ALMA MATER STUDIORUM
UNIVERSITÀ DI BOLOGNA

DOTTORATO DI RICERCA IN

IL FUTURO DELLA TERRA, CAMBIAMENTI CLIMATICI E SFIDE SOCIALI

Ciclo 38

**Settore Concorsuale:** 02/C1 - ASTRONOMIA, ASTROFISICA, FISICA DELLA TERRA E DEI PIANETI

**Settore Scientifico Disciplinare:** FIS/06 - FISICA PER IL SISTEMA TERRA E IL MEZZO CIRCUMTERRESTRE

# A NEW WINDOW ON THE IONOSPHERE: A LOFAR PERSPECTIVE, FROM GEOMAGNETIC STORMS TO STATISTICAL TRENDS

**Presentata da:** Rebecca Ghidoni

**Coordinatrice Dottorato**
Silvana Di Sabatino

**Supervisore**
Tiziano Maestri

**Co-Supervisori**
Luca Spogli
Claudio Cesaroni

Esame finale anno 2026

This thesis has been done as part of the research activity carried out at Istituto Nazionale di Geofisica e Vulcanologia (INGV) in Rome.

"We can only see a short distance ahead,
but we can see plenty there that needs to be done."

**— Alan Turing**

# Abstract

The LOw Frequency ARray (LOFAR) radio telescope, while primarily conceived for astronomical observation, offers a uniquely powerful modality for high-resolution ionospheric research. The fundamental principle lies in analysing the amplitude scintillations imposed upon trans-ionospheric radio signals originating from distant cosmic sources. As these coherent wavefronts traverse the ionosphere, they are perturbed by localized variations in plasma density, creating a complex diffraction pattern on the ground. LOFAR's dense configuration of antennas and its operational frequency range, which is highly sensitive to such plasma effects, make it exceptionally well-suited for the characterisation of these scintillations. This research leverages this advanced capability to produce several key scientific contributions to the field of space physics.

A primary and foundational objective of this work was to rigorously validate LOFAR as a robust instrument for ionospheric monitoring. To establish its credibility, a comprehensive comparative analysis and cross-validation were performed using data from established geospace instrumentation, including Global Navigation Satellite System (GNSS) receivers, ionosondes, and magnetometers. LOFAR-derived metrics, such as the scintillation index, were directly compared against measurements from these systems. The strong correlations achieved in this analysis successfully demonstrate not only the feasibility but also the reliability and precision of LOFAR for routine ionospheric diagnostics.

Building upon this validation, the research extended the scientific utility of LOFAR to the challenging domain of extreme space weather. A novel algorithm was developed specifically to determine the effective altitude of the ionospheric irregularity layer, a critical parameter for accurately modelling scintillation phenomena and understanding energy deposition processes in the upper atmosphere. The algorithm's robustness was proven by successfully processing data gathered during the most intense geomagnetic storm of the past two decades. This achievement showcases a unique capability to probe and quantify ionospheric dynamics under highly disturbed and rapidly changing conditions, which are often opaque to other measurement techniques.

Finally, to construct a climatological perspective, a comprehensive, long-term statistical analysis was performed on an extensive dataset encompassing over two years of continuous LOFAR ionospheric observations. This study covered a wide spectrum of geomagnetic conditions, from periods of profound quiet to times of severe storm activity. The investigation yielded significant new insights into the statistical distribution, morphological characteristics (such as field-alignment and scale size), and temporal evolution of the ionospheric irregularities that impact low-frequency radio systems. This has resulted in a more complete physical and statistical understanding of the processes governing plasma instability and structure in the middle/high-latitude ionosphere. By leveraging an extensive dataset spanning over two years this study rigorously quantified the morphological characteristics of these irregularities, specifically establishing their dominant magnetic field alignment, determining their anisotropic scale sizes, and defining the temporal evolution of the diffractive plasma structures that critically affect low-frequency radio systems

Collectively, these contributions establish LOFAR not only as a premier astronomical facility but also as an indispensable tool for space weather research, providing unprecedented observational capabilities that advance our understanding of ionosphere-magnetosphere coupling and its impacts on technological systems.

# Index

1. **The Ionosphere** ..... 19

*1.1. The discovery and exploitation of the ionosphere* ..... 20

*1.2. The main processes in the ionosphere* ..... 21
1.2.1. Photoionisation ..... 21
1.2.2. Recombination ..... 24

*1.3. The role of the Earth's magnetic field* ..... 25
1.3.1. The Appleton anomaly ..... 25
1.3.2. Particle precipitation ..... 26

*1.4. How the ionosphere interacts with other layers* ..... 27

*1.5. Ionospheric irregularities* ..... 28
1.5.1. Ionospheric scintillation ..... 29
1.5.2. Travelling Ionospheric Disturbances (TIDs) ..... 30
1.5.3. High Latitude irregularities ..... 31

2. **Instruments** ..... 35

*2.1. LOFAR* ..... 35
2.1.1. LOFAR configuration ..... 36
2.1.3. Normalised Intensity and S4 ..... 42
2.1.4. Mutual benefits between LOFAR and Ionosphere ..... 43

*2.2. Companion Dataset* ..... 45
2.2.1. GNSS ..... 45
2.2.2. Ionosondes ..... 48
2.2.3. Magnetometers ..... 50
2.2.4. Swarm ..... 53
2.2.5. Defense Meteorological Satellite Program (DMSP) ..... 54
2.2.6. International Geomagnetic Reference Field (IGRF) ..... 56
2.2.7. Kp Index ..... 57
2.2.8. Summary ..... 58

3. **Mathematical Methods** ..... 61

*3.1. Ionospheric Pierce Point* ..... 61

*3.2. GNSS measurements* ..... 62

*3.3. Dynamic Spectra* ..... 67

*3.4. Velocity from Cross-correlation* ..... 68
3.4.1. Spline interpolation ..... 71
3.4.2. Frozen-in approximation ..... 71

*3.5. Velocity from Fresnel's Method* ..... 72

*3.6. Effective Altitude retrieval* ..... 75

4. **Results** ..... 77

*4.1. January 2022 storm* ..... 77
4.1.1. The storm conditions ..... 77
4.1.2. Results and Discussion ..... 78
4.1.3. Final remarks ..... 90

*4.2. May 2024 Mother's Day Superstorm* ..... 91

4.2.1. Note on the naming convention ..... 91
4.2.3. The storm conditions ..... 92
4.2.4. LOFAR data ..... 93
4.2.5. May 10th 21:35-23:35 UTC (LOFAR dataset C - source: 3C380) ..... 95
4.2.6. May 11th 03:40-11:40 UT (LOFAR dataset D - source CASSIOPEIA A) ..... 98
4.2.7. Final remarks ..... 105

*4.3. Climatological analysis* ..... 106
4.3.1. Data screening and selection ..... 106
4.3.2. Results and discussion ..... 108

5. **Conclusions** ..... 117

*5.1. Summary of relevant outcomes* ..... 117

*5.2. Future Developments* ..... 118

**Bibliography** ..... 133

# Thesis Structure

The structure of this thesis is organized as follows:

**Chapter 1** provides a comprehensive introduction to the fundamental principles of ionospheric physics, discussing the main physical processes, morphology, and dynamics that govern the Earth's upper atmosphere.

**Chapter 2** details the instrumentation and diverse data sources utilised in this research. This chapter describes the operational principles of each instrument employed to observe and characterize ionospheric phenomena under a variety of geomagnetic conditions.

**Chapter 3** outlines the key mathematical and analytical formalisms applied throughout the data analysis. It describes the signal processing techniques and methods employed to ensure the robustness, accuracy, and validity of the scientific results derived from the observational data.

**Chapter 4** presents the principal scientific results of this research. The chapter commences with an analysis of a minor geomagnetic storm event from January 2022, establishing a baseline for instrument performance and response. Subsequently, the focus shifts to an in-depth investigation of the major geomagnetic superstorm of May 2024. This section highlights LOFAR's unique operational resilience during extreme space weather, demonstrating its capability to provide continuous, high-quality data even when conventional instruments, such as ionosondes, were rendered inoperable. The chapter culminates with a comprehensive statistical analysis of over two years of LOFAR ionospheric data, performed to identify the morphological characteristics of plasma irregularities affecting low-frequency radio observations.

**Chapter 5** synthesizes the key findings of the thesis, emphasizing the successful validation of LOFAR as a powerful and reliable ionospheric monitoring tool and highlighting its unique contributions to space weather science. To conclude, the chapter discusses promising avenues for future research and considers the potential applications and extensions of the methodologies and findings presented.

**Annexes** provide supplementary material essential for the detailed validation of the results. These include data availability charts for the ionosonde network and extended sets of dynamic spectra and scintillation index plots for the Mother's Day Superstorm. It also includes specific supporting data regarding solar flare effects and low-frequency ionospheric quietness.

The results described in this thesis are mainly reported also in:

- **Ghidoni**, R; Spogli, L; Mevius, M; Cesaroni, C; Alfonsi, L; Beser, K; Guerra, M; Maestri, T; (2025) Ionospheric Response to the January 2022 Geomagnetic Storm Using LOFAR and GNSS, *J. Space Weather Space Clim.*, *https://doi.org/10.1051/swsc/2025052*

- **Ghidoni**, R; Spogli, L.; Dorrian, G.; Mevius, M; Flisek, P; et al. (2025) LOFAR uniqueness under extreme ionospheric conditions: The May 2024 Mother's Day Superstorm, *J. Space Weather Space Clim.*,*https://doi.org/10.1051/swsc/2025059*

- **Ghidoni et al.** Statistical Analysis, [In Preparation]

# Acronyms

- **AGN:** Active Galactic Nuclei
- **AR:** Active Region
- **BDS**: BeiDou Navigation Satellite System
- **CC:** Cross-correlation
- **CME:** Coronal Mass Ejection
- **CS:** Core Station
- **DIAS:** Digital Upper Atmosphere Server
- **DMSP:** Defense Meteorological Satellite Program
- **DSCOVR:** Deep Space Climate Observatory
- **DST:** Disturbance Storm Time
- **ECEF:** Earth-centered, Earth-fixed
- **EEJ:** Equatorial Electrojet
- **EFI:** Electric Field Instrument
- **EGNOS:** European Geostationary Navigation Overlay Service
- **EIA**: Equatorial Ionisation Anomaly
- **EPB**: Eqautorial Plasma Bubble
- **ESA**: European Space Agency
- **FAC**: Field Aligned Currents
- **FFT**: Fast-Fourier Transform
- **GFLC**: Geometry Free Linear Combination
- **GIRO**: Global Ionospheric Radio Observatory
- **GLONASS**: Globalnaya Navigatsionnaya Sputnikovaya Sistema
- **GNSS**: Global Navigation Satellite System
- **GOES**: Geostationary Operational Environmental Satellites
- **GPS:** Global Positioning system
- **HBA**: High Band Antenna

- **HDFI**: High-Frequency Doppler-Frequency-Information
- **HF**: High-Frequency
- **IAGA**: Association of Geomagnetism and Aeronomy
- **ICME**: Interplanetary CME
- **IDOLS**: Incremental Development Of LOFAR Space Weather
- **IGRF**: International Geomagnetic Reference Field
- **INGV**: Istituto Nazionale di Geofisica e Vulcanologia
- **IMAGE**: International Monitor for Auroral Geomagnetic Effects
- **IMF**: Interplanetary Magnetic Field
- **IPP**: Ionospheric Pierce Point
- **IRNSS:** Indian Regional Navigation Satellite System
- **IS:** International Station
- **ISIS:** International Satellite Ionospheric System
- **ISMR:** Ionospheric Scintillation Monitoring Receivers
- **JSWSC:** Journal of Space Weather and Space Climate
- **LBA**: Low Band Antenna
- **LIRG**: LOFAR Ionospheric Research Group
- **LOFAR**: Low frequency Array
- **LoS:** Line of Sight
- **LSTID:** Large scale TID
- **MEO:** Medium Earth Orbit
- **MSTID:** Medium scale TID
- **NavIC:** Navigation with Indian Constellation
- **NOAA:** National Oceanic and Atmospheric Administration
- **OLS:** Operational Linescan System
- **PITHIA-NRF:** Plasmasphere Ionosphere Thermosphere Integrated Research Environment and Access services: a Network of Research Facilities
- **PLL:** Phase-Locked Loop

- **PSF:** Point Spread Function
- **QZSS:** Quasi-Zenith Satellite System
- **RFI:** Radio Frequency Interference
- **RNSS:** Regional navigation Satellite System
- **ROT:** Rate of TEC
- **ROTI:** Rate of TEC index
- **RS:** Remote Station
- **SAID:** Sub-Auroral Ion Drifts
- **SAPS:** Sub-Auroral Polarisation Streams
- **SED:** Storm Enhanced Density
- **SNR:** Signal-to-noise Ratio
- **SSIES:** Special Sensor for Ion and Electron Scintillation
- **SSJ:** Special Sensor J
- **SSM:** Special Sensor Magnetometer
- **SSTID:** Small scale TID
- **SSUSI:** Special Sensor Ultraviolet Spectrograph Imagers
- **STEC:** Slant TEC
- **SW:** Solar Wind
- **TEC:** Total electron content
- **TID:** Travelling Ionospheric disturbance
- **UT:** Universal Time
- **VTEC:** Vertical TEC
- **WAAS:** Wide Area Augmentation System

# Mathematical notation

In this thesis the mathematical variables and operations follow the same logic:

- x (non-bold lower-case): Scalar
- **x** (bold lower-case): Vector
- **M** (bold upper-case): Matrix
- $(\bullet)^{t}$: Transpose operator
- $\overline{(\bullet)}$: Conjugation
- $(\bullet)^{-1}$: Inverse
- $(\bullet)^{\dagger}$: Pseudo-inverse
- $\odot$: Hadamard element-wise multiplication operator
- $\otimes$: Kroneker matrix product
- $\frac{(\bullet)}{(\bullet)}$: Element-wise division
- $\mathcal{E}\{\bullet\}$ or $\langle\bullet\rangle$: Expected value
- diag(•): transport a vector on the main diagonal of a diagonal matrix
- vec(•): transform a matrix in a vector by stacking the columns vertically
- vecdiag(•): return the main diagonal of a matrix stacked into a vector.
- $\mathbf{a} \cdot \mathbf{b}$: Vectors inner product
- $e^{(\cdot)}$ or exp(.): Natural exponent
- $\mathbf{0}$: Vectors containing zeros
- $\mathbf{1}$: Vectors containing ones
- $\delta_{ij}$: the Kronecker delta function

# 1. The Ionosphere

The ionosphere is identified as the region of the atmosphere where the particle's ionisation is high enough to influence the propagation of radio signals (Kelley, 2009). This broad description makes it difficult to properly define the exact boundaries of the ionosphere. However, for practical applications, it is common to locate the Earth's ionosphere as the region, in the upper atmosphere, between 50 km and 1000 km above sea level (Brekke, 2013). It is important to understand that the ionosphere is not a distinct layer from the neutral atmosphere but overlaps with the thermosphere and parts of the mesosphere and exosphere. Indeed, those layers are defined by their thermal properties while the ionospheric layers are defined by their electrical properties, since the free electron density strongly depends on the altitude. The local characteristics of the ionosphere are influenced by many factors. However, the main processes that influence the presence of free electrons and ions in the atmosphere are photoionisation and recombination. Photoionisation is the physical process in which electromagnetic energy removes an electron from an atom or an ion. The opposite process, called recombination, refers to the capture of a free electron by a positive ion, leading to the emission of a photon (Hunsucker & Hargreaves, 2002).

Figure 1.1 shows the typical daytime (solid lines) and nighttime (dashed lines) electron density profiles at mid-latitude and for different solar activity conditions (red for solar maximum and green for solar minimum). Being related to photoionisation, high solar activity (flux) conditions result into generally higher level of ionisation. In addition, various regions can be identified, according to the local maxima of the electron density.

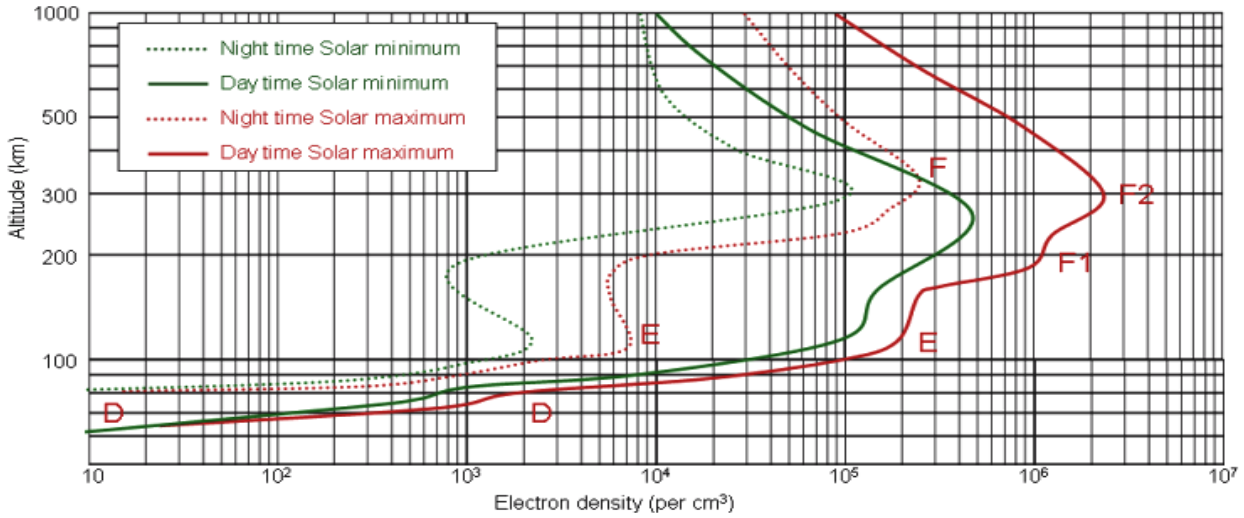



*Figure 1.1. Typical ionospheric electron density profile for daytime (continuous lines) and nighttime (dashed lines) hours. The green lines represent the density values during solar minimum, and the red lines represent the density values during solar maximum. The plot also shows the name of the layers in which the ionosphere is divided and their approximate altitude. From* https://sidstation.loudet.org/ionosphere-en.xhtml

The D region is the lowest ionospheric region and extends from 50 to 90 km and has an electron density peak of $\sim 10^3 \frac{e}{cm^3}$, at an altitude around 80 km. This layer usually does not heavily interfere with terrestrial radio communications, causing only the absorption of in the low frequency band (< 3

Mhz) and disappears after sunset, because of the high-rate of recombination with complex ions at low altitudes.

The E region extends usually from 90 to 150 km. The peak density is positioned at an altitude of around 120 km and present a density, during daytime, of $\sim 10^5 \frac{e}{cm^3}$. However, the density can reach, under specific conditions, values above $\sim 10^6 \frac{e}{cm^3}$ in a narrow layer, called sporadic E layer. It is mostly controlled by solar flux and solar zenith angle.

The region between 150 and above is called F region, and the peak density is reached at an altitude of around 250 to 350 km. During daytime hours, the F region splits into two different layers: the F1 and the F2 layers. The first is characterized by an electron density maximum at around ~ 180 km. The F2 layer presents the highest electron density and, therefore, is the most important layer for radio communication purposes. While F1 layer is mostly dominated by geochemistry processes, the F2 layer is featured by a high importance on transport and diffusion processes (Kelley, 1989).

## 1.1. The discovery and exploitation of the ionosphere

At the end of the XIX century the problem of explaining the observed daily variations in the Earth's magnetic field was solved by the Scottish physicist Balfour Stewart, that hypothesised the presence, in the atmosphere, of electric currents (Siegel, 1976). However, it was necessary to wait until 1901 to obtain a proof of this theory, when the Italian physicist Guglielmo Marconi successfully transmitted a radio signal across the Atlantic Ocean, between Poldhu in Cornwall (UK) and Signal Hill (Canada) (Marconi, 2002). This experiment proved the presence of a reflective layer in the upper part of the atmosphere. The following year, A. E. Kennelly and O. Heaviside independently demonstrated that this layer was an ionised layer.

However, the experiment that definitely confirmed the presence of the ionosphere around the Earth was conducted only in 1924, by the English physicist Edward V. Appleton. He demonstrated, using phase interference analysis, the existence of E, F1 and F2 layers. The era of Ionospheric Science could finally begin.

In the next years, many instruments were developed to investigate and exploit this part of the upper atmosphere, that only in 1932 started to be called "Ionosphere". The first ground-based instrument to specifically study this newly discovered electrical properties in the atmosphere was the ionosonde, an HF radar developed by the American physicists Gregory Breit and Merle A. Tuve.

With the development of the scientific research, it started to grow also the interest for the military application. During the World Wars, many countries understood the importance of fast and reliable communications around the entire globe. The second half of the twentieth century was, for this reason, characterised by the rapid growth of many satellite missions.

Some examples are the missions Alouette 1 and 2 launched in 1962 and 1965 respectively and International Satellites for Ionospheric Studies (ISIS) satellites launched in 1969 and 1971 respectively. All these missions were devoted mainly on the study of the ionospheric electron density distribution during quiet and disturbed helio-geophysics conditions (Benson & Bilitza, 2009).

In the meanwhile, US Navy starts to develop a satellite mission named Transit with the aim to furnish a positioning service to the ship during navigation in all weather conditions. First of the six Transit

satellites reached its orbit in 1960 and in 1967 the first satellite positioning service was made available for civil use. Taking advantage from the experience of Transit US Department of Defence started to develop a new satellite fleet and in 1994 the Global Positioning System (GPS) services was made available.

The late 20th and early 21st centuries saw a growing recognition of the strategic importance of independent positioning and navigational capabilities, leading to the development of two additional major systems: Galileo by the European Union and the BeiDou Navigation Satellite System (BDS) by China. Nowadays is common practice to consider all this satellites with the name Global Navigation Satellite System or GNSS.

In addition to its primary role of positioning, navigation and timing, GNSS has gradually extended its utility into various scientific disciplines. Among these, ionospheric research has particularly benefited of the continuous, global, and multi-frequency GNSS' radio signals. One pioneering example is the GPS Metereology (GPS/MET) experiment. From its lunch in April 1995 (Hajj & Romans, 1998), it used the GPS signals' occultation by the Earth's atmosphere to demonstrate the GPS capacity of provide new insights into ionospheric structures, by deriving the vertical electron density profiles.

Over time, as GNSS constellations expanded, satellite-based ionospheric experiments evolved from small, occasional experiments into robust and continuous monitoring systems.

## 1.2. The main processes in the ionosphere

### 1.2.1. Photoionisation

Despite the ionosphere being easily observable in the macro-world, its formation is guided by quantum processes. Specifically, photoionisation is the process occurring when a photon interacts with an atom, an ion or a molecule, causing the excitation of an electron. The process can be summarised by the reaction:

$$X + h\nu \rightarrow X^+ + e^- \tag{1.1}$$

where $X$ is the initial atom and $h\nu$ represents the incoming photon, whose energy is the product of Planck's constant, $h$, and its frequency, $\nu$ (Gold et al., 2025). The interaction yields a resulting ion, $X^+$, and an electron, $e^-$. This process governs the state of matter in numerous high-energy environments, from stellar nebulae to the upper layers of planetary atmospheres passing by plasma physics.

For the photoionisation process to occur, a strict energetic condition must be met: the energy of the incident photon must be greater than or equal to the ionisation energy, $E_I$, of the target species. The ionisation energy is therefore defined as the minimum energy required to remove the most loosely bound electron from an atom or molecule in its ground state. If the photon's energy precisely matches this ionisation energy, the electron is liberated with negligible kinetic energy. However, in the case the photon's energy exceed the ionisation threshold, the surplus energy is imparted to the ejected electron as kinetic energy, $K_n$ that contributes to the overall thermal energy budget of the newly formed excited state.

Due to its quantum nature, even when the energy condition is met, the occurrence of photoionisation is a probabilistic event. Indeed, the likelihood of the process is quantified by the photoionisation cross-section, denoted by $\sigma(\nu)$. This parameter represents the effective target area that an atom or molecule presents to an incoming photon of a specific frequency, $\nu$. A larger cross-section corresponds to a higher probability of ionisation. The value of the cross-section is strongly dependent on the photon's energy. For a given electron shell, the cross-section is effectively zero at the ionisation energy threshold ($h\nu < E_I$). It then rises sharply for energies just above this threshold, typically reaching a peak value before gradually diminishing as photon energy increases further. The study of this complex energy dependence is of prime importance in atmospheric science, as the solar spectrum is not uniform, as shown in figure 1.2.

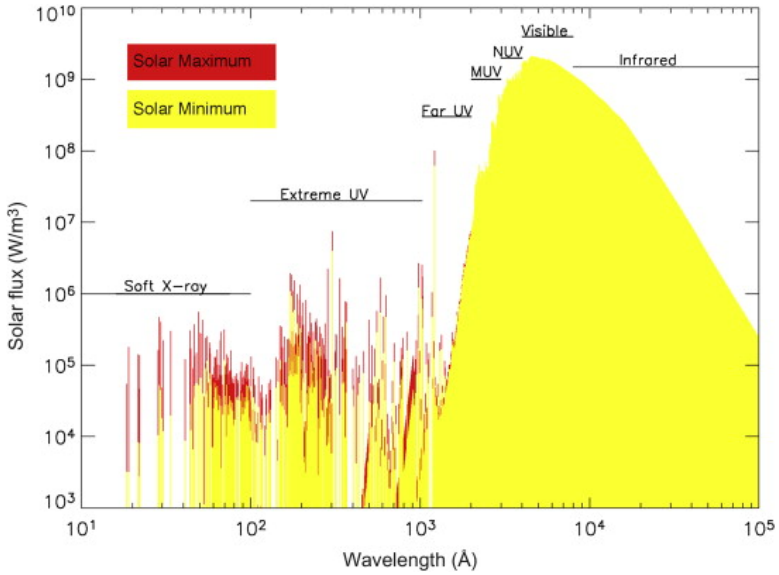



*Figure 1.2. Solar Spectrum Emission. From Encyclopedia of the Solar System(https://www.sciencedirect.com/book/9780124158450/encyclopedia-of-the-solar-system).*

As these energetic photons penetrate the thermosphere and mesosphere, they are absorbed, initiating the photoionisation reactions that sustain the presence of the ionosphere.

The overall rate of photoionisation at a given altitude is therefore a function of both the incident solar flux at each frequency and the corresponding photoionisation cross-sections of the local gases in the atmosphere.

It is important to remember that the atmosphere composition strongly depends on altitude, as shown in figure 1.3. This influences the capacity of different solar wavelengths to penetrate the atmosphere.

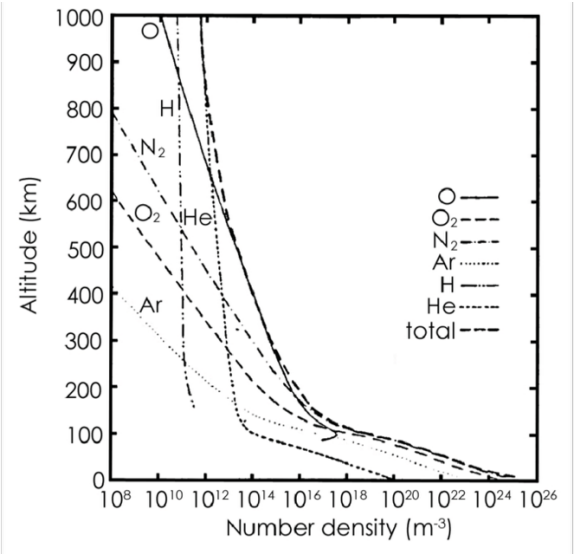



*Figure 1.3. Variation of atmospheric composition to an altitude of 1000 km for a typical temperature profile (Based on: U.S. standard atmosphere, 1976 (https://ntrs.nasa.gov/api/citations/19770009539/downloads/19770009539.pdf))*

The characteristic layered structure of the ionosphere, as summarised in figure 1.3, is conceptually explained by the Chapman theory (Chapman, 1931). This model describes the formation of an ionospheric layer as a balance between the production of ion-electron pairs by solar photoionisation and their loss through recombination. The shape of the layer arises from two competing factors that vary with altitude: the intensity of incoming solar radiation and the density of the neutral atmosphere. At very high altitudes, the neutral atmosphere is sparse, so despite abundant solar radiation, the rate of ionisation is low. Conversely, at lower altitudes, the atmosphere is dense, but most of the ionizing solar radiation has been absorbed by the layers above, again resulting in a low ionisation rate. The peak of an ionospheric layer, therefore, forms at the specific altitude where the product of the neutral gas density and the ionising radiation flux is maximized. This creates the distinct, vertically stratified profile of electron density that characterizes the different regions of the ionosphere. While a simple Chapman model assumes a single atmospheric species, the presence of multiple layers like the D, E, and F regions is a consequence of the complex composition of the upper atmosphere. Different atomic and molecular species have distinct density profiles that vary differently with altitude and absorb different wavelengths of solar radiation. This results in multiple peaks of ionisation at various altitudes, creating the distinct, vertically stratified profile of electron density that characterizes the different regions of the ionosphere.

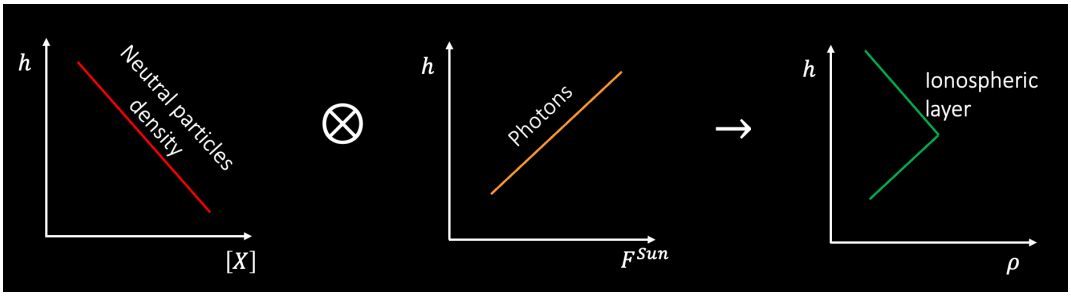



Figure 1.4. Schematic graph of the *ionospheric layer formation according to the Chapman theory*. The red line represents the increment of the density of an atmospheric neutral particle (e.g. $X$) as the altitude decreases. The yellow line shows the decreasing capacity of the photons to penetrate the lower layers of the atmosphere. The combination of these two processes creates the characteristical shape of the ionospheric layers' density (green line).

### 1.2.2. Recombination

The inverse process of photoionisation is called plasma recombination and describe the process by which positive ions of a plasma capture a free electron or a negative charged ion to form new neutral atoms, or less charged ions.

This process primarily occurs through three distinct mechanisms: dissociative recombination, radiative recombination, and ion-ion recombination. The prevalence of each mechanism is dictated by the atmospheric composition, density, and temperature characteristic of each ionospheric region.

In the lower D and E regions, where molecular ions such as $O_2^+$ and $NO^+$ are abundant, dissociative recombination is the dominant process. This is a rapid two-step mechanism where an electron is captured by a molecular ion, forming an unstable excited neutral molecule that subsequently dissociates into neutral atoms. Due to its high-rate coefficient, this process is the primary sink for electrons in these lower, denser regions.

Conversely, in the higher and less dense F region, where atomic oxygen ions ($O^+$) are the principal ionic species, dissociative recombination cannot occur directly. Here, a slower two-step process begins with ion-atom interchange reactions, such as the conversion of $O^+$ to $NO^+$ or $O_2^+$ through reactions with $N_2$ or $O_2$, followed by the rapid dissociative recombination of these newly formed molecular ions. Radiative recombination, where an electron is captured by an atomic ion with the simultaneous emission of a photon, is a much slower process and is generally a minor loss mechanism for electrons throughout the ionosphere.

Finally, ion-ion recombination, involving the mutual neutralisation of positive and negative ions, becomes significant only in the lowest D-region, particularly at night, where the higher atmospheric pressure allows for the formation and presence of a substantial population of negative ions. The interplay and altitude-dependence of these recombination processes are therefore critical in determining the overall structure and dynamics of the ionosphere.

While these recombination processes are continuous, their net effect is most pronounced at night. During the day, photoionisation by solar radiation constantly produces new ion-electron pairs, largely balancing the loss from recombination. In the absence of sunlight, however, recombination becomes the dominant process, leading to a significant decrease in total electron density, particularly in the D and E regions.

However, the ionosphere does not entirely disappear at night because the recombination time for the ions and electrons (the average time required for all the ions and electrons to unite to form neutral particles) is long enough for the layer to persist overnight.

## 1.3. The role of the Earth's magnetic field

Being composed of charged particles, the shape of the ionosphere is strongly influenced by the Earth's magnetic field lines. Besides the solar zenith angle, which triggers the ionospheric plasma distribution at the largest scale, at a global level, the Earth's magnetic field morphology redistributing the charged particles in the so-called "Appleton anomaly", in the Equatorial sector, and by favouring the direct particle precipitation from the solar wind around the magnetic poles, which constitute an additional source of ionisation.

While the primary focus of my research is on mid-latitude and sub-auroral ionospheric phenomena, it is crucial to recognize that ionospheric regions are not isolated but are part of a highly coupled system. Phenomena originating in one region can significantly impact adjacent areas. Therefore, a general understanding of processes at other latitudes, such as the equatorial or polar regions, is also essential. A clear example of this interconnectedness was observed during the major geomagnetic storm of May 2024, when phenomena typically confined to high latitudes converged and produced significant effects at mid-latitudes (Spogli et al., 2024).

### 1.3.1. The Appleton anomaly

The Equatorial Ionisation Anomaly (EIA), called also Appleton Anomaly or Equatorial Fountain, is the largest ionospheric structure. It is created and maintained by the joint effect of the daytime eastward electric field flowing in a narrow (few degrees) latitudinal band around the magnetic equator in the E-layer (equatorial electrojet, EEJ) and of the Earth's magnetic field, whose lines are almost horizontal at equatorial latitudes. This causes the F-layer plasma to drift upward to higher altitudes. Concurrently to the upward displacement, plasma flows down the geomagnetic field lines under the influence of pressure gradients and gravity. Despite maximising at the magnetic equator, the field-perpendicular plasma drift and field-aligned plasma diffusion act together all along the field lines at all altitudes, causing plasma to flow in the direction of the resultant. This means that diffusion along the magnetic field lines occurs simultaneously with the uplift and not only after when the plasma falls back to lower altitudes (Balan et al., 2018; Spogli et al., 2023). This movement is the responsible for the anomalously density accumulation at the EIA crests. As a result, plasma density at the crests can be an order of magnitude higher than at the dip equatorial F peak, even at nighttime. A scheme of the distribution of charged particles near the magnetic equator is shown in figure 1.4. The characteristic distribution of the ionospheric plasma is symmetrically divided north and south off magnetic equator with a typical enhancement around 20° in magnetic latitude. This redistribution of plasma depletes the ion concentration directly above the equator and forms two bands of enhanced density, labelled as the "Ionosphere Crest," on either side.

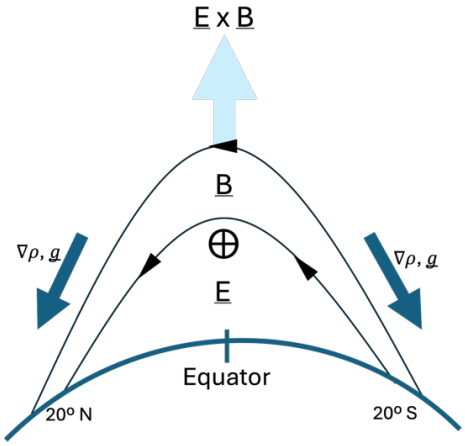



*Figure 1.5. Scheme of distribution of charged particles near the magnetic equator. From Cesaroni (Private Communication)*

### 1.3.2. Particle precipitation

While solar radiation is the primary driver of the global, dayside ionosphere, the influx of charged particles from the Sun provides a second, distinct, and highly dynamic mechanism of ionisation. This process, known as "direct particle precipitation", involves energetic particles, originating from the Solar Corona, that are guided by the Earth's magnetosphere down to the upper atmospheric layers. The continuous streams of these charged particles, mainly electrons, protons and alpha particles, released from the outermost layer of the Sun's atmosphere is called solar wind. This plasma travels outward through the solar system at supersonic speeds of order of hundreds of km/s. The solar wind carries the frozen-in Interplanetary Magnetic Field (IMF), which interacts with the Earth's magnetosphere. Under northward conditions of the IMF (positive z-components, IMF-Bz>0), the Earth's magnetosphere is closed and acts as a protective shield, deflecting the bulk of this constant flow of particles around the planet. However, the magnetosphere is not an impermeable barrier. Southward conditions of the IMF (IMF-Bz<0) favour the transfer of energy and momentum from the solar wind to the magnetosphere-ionosphere system.

This energy transfer drives a vast system of electrical currents that couple the distant magnetosphere to the high-latitude ionosphere. These are known as Field-Aligned Currents (FACs) because they flow along the Earth's magnetic field lines. This system, first described by Iijima & Potemra (1976), is dominated by two concentric rings of current. The region 1 (R1) currents, located at the poleward edge of the auroral oval, are directly driven by the solar wind interaction and flow into the ionosphere on the dawn side and out of the ionosphere on the dusk side. Conversely, the region 2 (R2) currents are located at the equatorward edge of the auroral oval and are associated with pressure gradients in the inner magnetosphere. They flow in the opposite direction: out of the ionosphere on the dawn side and into it on the dusk side.

The particle precipitation that ionizes the high-latitude atmosphere is fundamentally linked to these current systems. The upward-flowing FACs are carried by energetic electrons accelerated downward from the magnetosphere. These precipitating electrons collide with atmospheric gases, causing the

visible aurora and creating significant, localized ionization. This precipitation is geographically concentrated. On the magnetic dayside, the polar cusps provide a direct entry point for solar wind particles. On the nightside, the magnetotail acts as a vast plasma reservoir. Dynamic processes within the magnetotail can accelerate these stored particles and inject them toward Earth through magnetic reconnection, specifically into the ring-shaped area defined by the R1 and R2 currents: the auroral oval.

Thus, the auroral oval is the ionospheric projection of the magnetospheric plasma sheet and boundary layers. It is along these specific magnetic field lines, carrying the FACs, that particle precipitation is most consistently observed, acting as a key source of the high-latitude irregularities studied in this work.

## 1.4. How the ionosphere interacts with other layers

Earth's upper atmosphere is not a static structure but a complex and dynamic system, that is influenced by many physical phenomena.

Figure 1.5, credited to J. Grebowsky, provides a comprehensive visualisation of the major physical processes that connect the Sun, Earth's magnetosphere, ionosphere, and thermosphere. On the left, the Sun is depicted as the primary source of energy, providing two distinct inputs that drive the geospace system.

The first of these is radiation, which represents the flux of photons that propagates to Earth's dayside, where it ionises the neutral upper atmosphere through photoionisation. The second primary input is the solar wind, that transports plasma particles towards the Earth and that can modify the complex current system running in the magnetosphere-ionosphere system.

In the equatorial and mid-latitude regions, the upper atmosphere dynamics is largely governed by the interplay between the neutral atmosphere and the ionosphere, constrained by the geometry of the magnetic field. Neutral winds in the thermosphere, depicted by yellow arrows, exert a dragging force on the ions. Near the magnetic equator, this force pushes plasma upwards to higher altitudes along the arched magnetic field lines. Once elevated, this plasma diffuses downward under the influence of gravity, following the magnetic field lines away from the equator in a process known as the Fountain Effect. On a larger scale, the grey loops representing magnetic flux tubes show the continual exchange of plasma between the ionosphere and the overlying plasmasphere, a region of cold, dense plasma in the inner magnetosphere.

The high-latitude polar regions are dominated by highly energetic processes. The "Auroral Heating Region" acts as the central engine, where the deposition of energy from precipitating particles intensely heats both the ionized and neutral gases, through Joule and particle heating processes. This energy, combined with electric fields generated by the solar wind's interaction with the magnetosphere, drives a large-scale pattern of "Magnetosphere-Driven Ion Convection," where plasma is transported at high speeds across the polar cap. This convective motion generates distinct features such as the "Ionosphere Trough," a channel of depleted plasma density in correspondence with the equatorward boundary of the auroral oval. The diagram illustrates the critical concept of ion-neutral coupling in this region. The intense heating causes "Neutral Upwelling," a vertical expansion of the neutral atmosphere. Concurrently, the rapidly moving ions drag the neutral gas with them,

creating a powerful "Ion-Driven Wind". In the most extreme cases, this combination of heating and upward motion can accelerate atmospheric constituents to escape velocity, resulting in "Ion/Neutral Escape" and a gradual loss of atmosphere to space.

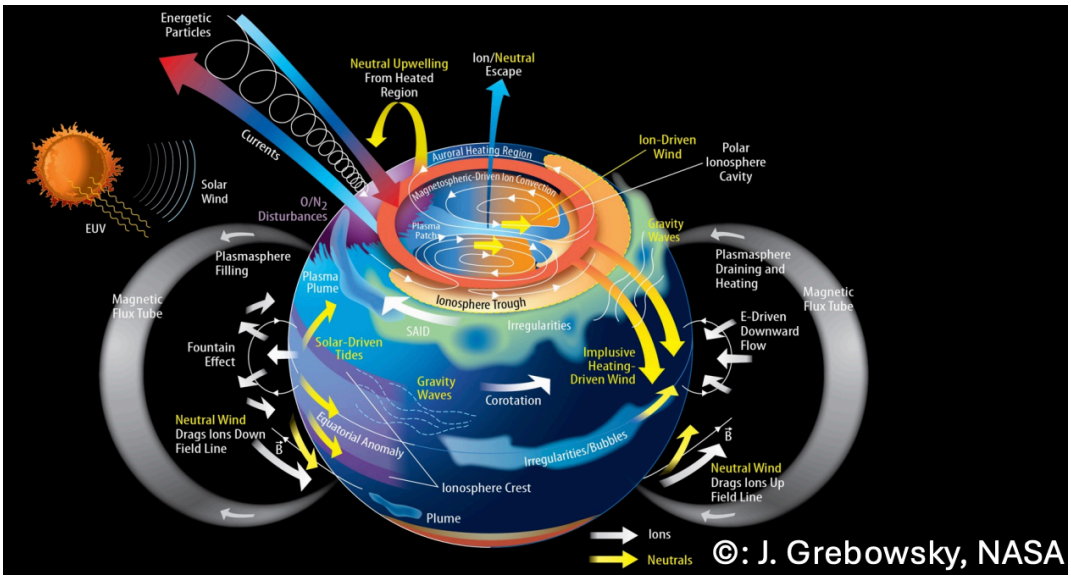



*Figure 1.6. Scheme of the interaction of the Earth's ionosphere-thermosphere system. From J.Grebowsky (NASA)*

## 1.5. Ionospheric irregularities

While simplified global models can depict the ionosphere as a smooth, stratified medium, its true nature is profoundly dynamic and complex. It is continuously perturbed by the interaction of forces originating from solar, magnetospheric, and lower atmospheric sources. These perturbations create deviations from the background electron density, collectively known as ionospheric irregularities. These irregularities exist across a vast spectrum of spatial scales, from thousands of kilometres down to a few centimetres and may create disturbed ionospheric conditions with timescales from seconds to several hours.

However, their effect on a trans-ionospheric radio signal is not absolute but it is determined by the size of the irregularity relative to the signal's Fresnel's scale. The Fresnel's scale defines the region of the wavefront that significantly contributes to the signal received at the ground, and it is a function of the signal wavelength and the distance to the irregularity layer.

This scale dependency creates two distinct regimes of interaction. Large-scale irregularities, with scales much larger than the Fresnel's scale, do not scatter the signal. Instead, they act as large, weak lenses, causing systematic refraction. This bending of the signal path manifests as large-scale, coherent variations in the Total Electron Content (TEC) and is the primary mechanism behind Travelling Ionospheric Disturbances (TIDs). In contrast, the so-called small-scale irregularities, with sizes comparable to or smaller than the Fresnel's scale, act as a diffraction screen. As the radio wave passes through this turbulent medium, it is scattered, creating a complex interference pattern on the ground. This diffractive process is the source of rapid fluctuations in both signal amplitude and phase, a phenomenon known as ionospheric scintillation.

This thesis will investigate the few-kilometres scale structures responsible for ionospheric scintillation in the data collected by LOFAR and it will also characterise the large-scale TIDs, which are often the underlying "seed" mechanisms that generate the smaller, scintillation-producing irregularities.

### 1.5.1. Ionospheric scintillation

Ionospheric scintillation refers to the rapid fluctuations in a trans-ionospheric radio wave as it passes through the irregularities in electron density. The phenomenon is analogous to the twinkling of starlight (astronomical scintillation) caused by turbulence in the Earth's troposphere. It was first identified in the field of radio astronomy, where it was observed as irregular, short-period variations in the intensity of cosmic radio emission (Hey et al., 1946). While originally thought to be intrinsic to the celestial sources, these fluctuations were later confirmed to be caused by diffraction as the wavefront traverses a medium containing electron density irregularities (Smith, 1950)

The presence of ionospheric irregularities induces two primary propagation effects on radio signals: refraction and diffraction.

Refraction is caused by irregularities with scales covering full spectrum of scale sizes. They act as weak lenses, systematically bending the signal's ray path. This bending introduces a coherent phase shift but leaves the signal amplitude unchanged, as the energy is only redirected.

In contrast, diffraction is a more complex phenomenon arising from smaller-scale irregularities, particularly those with sizes below the first Fresnel's zone of the signal and related observational geometry. These irregularities act as scattering centres, causing the incident plane wave to be re-radiated as a multitude of secondary wavelets. At the receiver, these wavelets interfere, leading to a complex, spatially and temporally varying pattern of constructive and destructive interference. This process is the source of the fluctuations in both signal amplitude (fading and enhancement) and phase (advance and delay). The stochastic nature of this effect is a direct consequence of the turbulent and random distribution of the plasma density irregularities. The theoretical framework for describing this concerns the Fresnel's diffraction, which models the near-field interference pattern generated by a "diffracting screen" located at the height of the ionosphere. It is this diffractive scattering that constitutes the most significant challenge for satellite communication and navigation systems. For example, in GNSS, the rapid and deep amplitude fades can cause the signal-to-noise ratio to fall below the receiver's tracking threshold, leading to a complete loss of lock. Simultaneously, the rapid phase variations can overwhelm the receiver's Phase-Locked Loop (PLL), causing instantaneous loss of the integer-cycle ambiguity in the carrier phase measurement. These losses are called cycle-slips and can severely degrade the accuracy and reliability of applications reliant on precise positioning and timing, such as the GNSS (Poniatowski & Nykiel, 2020).

Scintillation is a highly geographically and temporally dependent phenomenon (Yeh & Liu, 1982). It is possible to consider three main ionospheric regions where scintillations phenomena are present with different characteristics:

- Equatorial Region: The post-local sunset equatorial ionosphere is the site of the most intense scintillation events. After sunset, the rapid decrease in conductivity at the base of the F-layer, combined with the gravitational force acting on the dense plasma above, creates the conditions for the Rayleigh-Taylor instability. This instability leads to the formation of large-scale (~ 100 km) depletions in plasma density known as Equatorial Plasma Bubbles (EPBs). The steep

gradients and turbulence on the edges of these bubbles contain the small-scale irregularities that can cause severe amplitude and phase scintillation (Balan et al., 2018; Bhattacharyya, 2022; Li et al., 2021).

- High-Latitude Regions: The auroral and polar cap regions are also hotspots for scintillation. Here, the generation mechanisms are linked to magnetospheric processes, including the precipitation of energetic particles and the presence of strong electric fields and plasma convection. These processes create a variety of plasma instabilities that generate field-aligned irregularities, leading to persistent, though typically less intense than equatorial, scintillation (Enengl et al., 2024; Nishimura et al., 2023; Spogli et al., 2009).
- Mid-Latitudes: The mid-latitude ionosphere is generally considered quieter. However, significant scintillation can occur, particularly during severe geomagnetic storms (Spogli et al., 2024). During these events, the auroral oval expands equatorward, and large-scale phenomena like large scale TIDs can create steep density gradients that may decay into smaller, scintillation-producing irregularities through mechanisms like the Perkins instability (Cesaroni et al., 2017; Zakharenkova et al., 2016) .

The study of ionospheric irregularities is driven by both fundamental scientific inquiry and significant practical applications. In fact, strong amplitude scintillation can cause, for example, the received signal power to drop below the receiver's tracking threshold, leading to a "loss of lock" on the satellite signal. Phase scintillation rapidly alters the signal's phase, corrupting the carrier phase measurement. The discontinuities in the measured signals, which are called "cycle slips", can be disastrous for high-precision positioning and timing applications (Luo et al., 2018; Vadakke Veettil & Aquino, 2021).

.

Ionospheric scintillation is central to my research, as it is the very presence of this phenomenon that induced intensity variations that enables the probing of ionospheric dynamics. Specifically, the analysis of these diffraction patterns as they traverse the LOFAR array provides the fundamental data required to reconstruct the drift velocity of the irregularities and, subsequently, to retrieve their effective altitude, as detailed in Chapter 4.

### 1.5.2. Travelling Ionospheric Disturbances (TIDs)

As my research primarily focuses on the mid-latitude ionosphere, understanding the dominant source of plasma instabilities in this region is critical. At these latitudes, while various plasma processes contribute to ionospheric instability, Travelling Ionospheric Disturbances (TIDs) are now understood to be the primary driver for the generation of scintillation-producing irregularities.

TIDs are the ionospheric manifestation of Atmospheric Gravity Waves (AGWs), propagating upwards from the lower atmosphere. As an AGW propagates through the thermosphere, the wave-like motion of neutral particles is imparted to the ionospheric plasma via collisional coupling. This forces the ions and electrons into a similar oscillatory pattern, creating the quasi-periodic enhancements and depletions in electron density that presents as a TID.

TIDs are typically classified based on their observational characteristics, such as wavelength, period and velocity, which are directly related to their source mechanisms. The three primary categories are Large-Scale TIDs (LSTIDs), Medium-Scale TIDs (MSTIDs) and Small-Scale TIDs (SSTIDs).

LSTIDs represent the largest and fastest of these disturbances(Borries et al., 2009; Hocke & Schlegel, 1996; Katamzi et al., 2012; Thaganyana et al., 2022).

The immense energy deposited into the auroral oval during extreme events, through Joule heating and energetic particle precipitation, can generate large-amplitude AGWs that subsequently propagate equatorward. LSTIDs are defined by horizontal wavelengths greater than 1,000 km and periods ranging from approximately 45 minutes to 3 hours. They propagate at high horizontal velocities, typically between 300 and 1,000 m/s, and travel predominantly equatorward from the auroral zones of both hemispheres. The passage of an LSTID causes significant, large-scale undulations in the F-region electron density and, consequently, pronounced variations in the Total Electron Content (TEC). These perturbations can introduce range errors of several meters for GNSS users and cause significant Doppler shifts in High Frequency (HF) radio signals.

On the other hand, MSTIDs are a more common and ubiquitous phenomenon than LSTIDs. Their sources are believed to be largely meteorological, originating from the lower atmosphere. A variety of tropospheric and stratospheric events (Barta, Veronika et al., 2025; Honda et al., 2025), e.g. severe weather systems, seismic events (Sanchez et al., 2025), tsunamis, volcanic eruptions (Cahyadi et al., 2021; Verhulst et al., 2022), airflows over mountainous terrain, and even artificial phenomena like explosions (Jonah et al., 2021) or the passage of a rocket (Chou et al., 2018) can generate AGWs that propagate vertically into the thermosphere. MSTIDs are characterized by horizontal wavelengths of several hundred kilometres (typically 100-500 km) and periods shorter than LSTIDs, generally between 10 and 60 minutes. Their horizontal velocities are slower, in the range of 50 to 350 m/s (Hernández-Pajares et al., 2012), and their direction of propagation is highly variable, often related to the location of their tropospheric source. While smaller in amplitude than LSTIDs, the frequent occurrence of MSTIDs makes them a persistent source of ionospheric variability.

At the smallest end of the spectrum are Small-Scale TIDs (SSTIDs), with wavelengths of tens of kilometres and periods of a few minutes (Boyde et al., 2022; Tsybulya & Jakowski, 2005; Yin et al., 2019). These are often generated by the nonlinear breakdown of larger MSTIDs or localized atmospheric events. The sharp, steep electron density gradients associated with SSTIDs are of particular importance, as they can directly trigger plasma instabilities (e.g., the Perkins instability), acting as seed mechanisms for the generation of the meter-scale irregularities that ultimately produce ionospheric scintillation.

The primary impact of TIDs on trans-ionospheric radio signals is the imposition of significant, periodic variations in TEC (Basu et al., 2002; Borries et al., 2009; Kotulak et al., 2020). This modulation introduces range errors that can severely compromise the accuracy of high-precision applications. Furthermore, under certain conditions, the sharp density gradients associated with TIDs can act as seed mechanisms, triggering plasma instabilities that lead to the generation of the smaller-scale irregularities discussed previously, thereby creating conditions conducive to scintillation.

Characterizing TIDs is crucial, as they represent the large-scale structures that, in my research, are compared against the smaller-scale irregularities detected by LOFAR during the geomagnetic storms.

### 1.5.3. High Latitude irregularities

At auroral and sub-auroral latitudes, the ionosphere is dominated by complex interactions between magnetospheric forcing and ionospheric plasma dynamics. This coupling facilitates the transfer of energy and momentum from the solar wind down into the high-latitude atmosphere, creating a variety of instability mechanisms. As reviewed by Nishimura et al. (2022), three primary mechanisms are responsible for the formation of small-scale structures in this region: irregularities associated with the polar cusp, the Gradient Drift Instability (GDI), and the Kelvin-Helmholtz Instability (KHI).

Cusp irregularities are observed in the dayside high-latitude ionosphere, where the solar wind has direct access to the Earth's upper atmosphere. Here, intense low-energy particle precipitation significantly enhances electron temperature and density, creating turbulence. The Gradient Drift Instability (GDI) is a dominant mechanism for structuring polar cap patches; as these high-density islands convect across the polar cap, the GDI acts primarily on their trailing edges, causing the smooth plasma to fracture into smaller, unstable structures. Finally, the Kelvin-Helmholtz Instability (KHI) is driven by strong velocity shears common at the boundaries of fast-moving plasma flow channels, rolling the plasma into large-scale vortices that subsequently break down into smaller irregularities.

These instabilities often coexist with, or are driven by, large-scale magnetospheric features. A principal manifestation is the formation of the auroral electrojets—intense, horizontal currents flowing in the E-region (approx. 100-120 km altitude) driven by the magnetospheric convection electric field. Adjacent to the auroral zone lies the main ionospheric trough, a persistent nightside feature characterized by a significant depletion in plasma density formed at the boundary between sunward-convecting auroral plasma and co-rotating mid-latitude plasma. Within this trough region, particularly during geomagnetically active periods, narrow channels of supersonic westward plasma flow known as Sub-Auroral Ion Drifts (SAID) or polarisation streams can develop. These features create extremely sharp localized gradients in plasma density and temperature, which can severely affect trans-ionospheric radio signals.

### 1.5.4. Other irregularities

Beyond the wave-like structures of TIDs, the ionosphere is host to other distinct forms of irregularities that can affects the different regions.

A prominent example at mid and low latitudes is the Sporadic E (Es) layer. These are not traditional ionospheric layers but are transient, anomalously dense, and extremely thin (~1-2 km thick) patches of plasma that form within the E-region (~ 90-140 km altitude). Their formation is not driven by photoionisation but by a dynamic process described by the wind shear theory (Axford, 1963; Whitehead, 1961). This theory posits that vertical shears in the horizontal neutral wind interact with the Earth's magnetic field. This interaction exerts a Lorentz force that "sweeps" and compresses long-lived metallic ions (such as $Fe^+$ and $Mg^+$, deposited by meteor ablation) into a very dense, thin sheet. Because these metallic ions have a very low recombination rate compared to the ambient molecular ions ($O_2^+$, $NO^+$), they can accumulate to densities far exceeding the background. The resulting layer can unexpectedly support or block high-frequency (HF) radio propagation and, under certain conditions, decay into smaller-scale irregularities (Haldoupis, 2011).

Additionally, at auroral and sub-auroral latitudes, the ionospheric plasma is frequently and intensely disturbed by phenomena driven by magnetosphere-ionosphere coupling. This coupling facilitates the transfer of energy and momentum from the solar wind and magnetotail down into the high-latitude atmosphere along geomagnetic field lines, primarily through particle precipitation and the imposition of large-scale electric fields. A principal manifestation of this energy deposition is the formation of the auroral electrojets—intense, horizontal currents flowing in the E-region ionosphere (approximately 100-120 km altitude) within the auroral oval. Driven by the magnetospheric convection electric field, these currents are bifurcated into a westward electrojet in the nightside sector and an eastward electrojet in the dayside sector.

Adjacent to the main auroral zone lies the main ionospheric trough, a persistent feature of the nightside F-region ionosphere characterized by a significant depletion in plasma density. This structure forms at the boundary between the sunward-convecting auroral plasma and the co-rotating mid-latitude plasma. The trough's formation is attributed to the prolonged residence of plasma flux tubes in darkness, combined with enhanced ion-neutral frictional heating and increased plasma recombination rates driven by strong perpendicular electric fields. Its sharp density gradients on both the poleward and equatorward walls represent a significant source of ionospheric disturbance. Within this trough region, particularly during geomagnetically active periods, narrow, supersonic channels of westward plasma flow, known as sub-auroral ion drifts (SAID) or polarisation streams, can develop. These features, driven by intense poleward-directed electric fields, further exacerbate the plasma depletion and create extremely sharp localized gradients in plasma density and temperature, which can severely affect trans-ionospheric radio signals.

LOFAR's observational geometry, with its extensive network of European stations, provides lines-of-sight that frequently intersect these auroral and sub-auroral regions, enabling the detailed study of the irregularities they generate. The specific structure of the LOFAR array that facilitates these observations will be detailed in Chapter 2.1, and the scientific results from these studies will be presented in Chapter 4.

# 2. Instruments

As described in Chapter 1, the Earth's ionosphere is a complex and dynamic plasma environment. For this reason, its study necessitates a plethora of observational techniques and instrumentation. Over the decades, a suite of ground-based and space-borne instruments has been developed to probe its structure and behaviour, including tools such as ionosondes, incoherent scatter radars, and Global Navigation Satellite System (GNSS) receivers, each providing crucial but distinct insights into the ionospheric state.

While this research leverages data from several of these established instruments, its primary focus is on exploiting the novel capabilities of the LOFAR radio telescope. The unprecedented sensitivity and flexibility of LOFAR offer a unique window into ionospheric phenomena. The subsequent sections will provide a detailed description of the operational principles of LOFAR, as well as the complementary traditional instruments utilized in this work, to establish the observational foundation for the research presented herein.

## 2.1. LOFAR

LOFAR is a radio interferometer extending across nine European countries, with most of its antennas concentrated in the Netherlands (van Haarlem et al., 2013) in a three km$^2$ area centered at 52°54' N and 6°52' E. LOFAR covers the frequency range 10-240 MHz, that corresponds to a wavelengths range of ~30–1.2 m. This allows it to reach the lowest end of the radio band observable from the Earth's ground-level, as shown in figure 2.1, with an unprecedented sensitivity and angular resolution in this poorly explored regime.

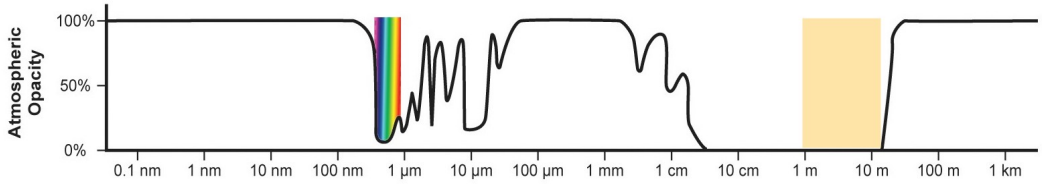



*Figure 2.1. Graphical representation of which electromagnetic wavelength regions are blocked by Earth's atmosphere. The yellow band represents the range of LOFAR observations. (Source: NASA, 2011)*

The main objectives of LOFAR, as described in (van Haarlem et al., 2013), can be summarised in six Key Science Projects (KSPs), which cover wide fields of radio astronomy:

1. **Cosmic magnetism of the nearby universe**: LOFAR investigates the magnetic fields of the Universe, by observing synchrotron radiation from Cosmic Rays in both the Milky Way and distant galaxies, as well as by exploiting the Faraday rotation of the emitted signals.
2. **Cosmic Rays**: The collisions between high energy cosmic rays (HECRs) and atoms in Earth's atmosphere generate a cascade of secondary particles that emit radio-flashes and can thus be studied by LOFAR.

3. **Epoch of Reionisation**: The 21 cm line from neutral hydrogen at the Epoch of Reionisation is red shifted to the frequency regime of LOFAR. The detection of this signal can provide valuable information on the first stars and galaxies in the early Universe.
4. **Solar physics and space weather**: The radio emission of the Sun associated with periodical flares and coronal mass ejections have a huge impact on Earth and the space environment. Most of the activity has strong signatures in the frequency range explored by LOFAR, which can be used for Space Weather monitoring and studies.
5. **Transient events**: Long-period monitoring of wide areas of the sky can reveal transient phenomena, such as variable active galactic nuclei (AGNs), novae, supernovae, pulsars, X-ray binaries, fast radio bursts, and gamma-ray burst afterglows.
6. **Deep extragalactic surveys**: LOFAR is scanning the whole Northern Sky through different ongoing surveys. These are providing unprecedentedly large catalogues of radio sources thanks to the excellent sensitivity of LOFAR.

### 2.1.1. LOFAR configuration

At present, LOFAR consists of a network of 52 stations spread all over Europe that measure at frequencies between 10 and 240 MHz. The Netherlands host 38 stations, whereas 14 stations are distributed in France (1), Germany (6), Ireland (1), Latvia (1), Poland (3), Sweden (1), and United Kingdom (1); two additional stations are going to be built in Italy, near the Medicina Radio Observatory site (Bologna), and in Bulgaria as part of the LOFAR 2.0 upgrade. The Dutch stations are organised in 'Core' (CS) and 'Remote' (RS) stations, while the other European stations are referred to as 'International' (IS) stations. Near the Dutch village of Exloo, the 24 core stations (Figure 2.2a) are distributed across an area of radius ~ 2 km; among them, 6 stations are located in an even smaller central island of 320 m of diameter, and constitute the so-called Superterp (Figure 2.2b). The 14 remote stations are spread within a radius of 90 km (Figure 2.3). The 14 international stations (Figure 2.4) provide the longest baselines that allow to reach sub-arcsec resolution.

To match the necessity of covering a broad frequency range sensitive to Radio Frequency Interference (RFI) of various origins, as well as minimising the construction costs, two different designs have been developed for the LOFAR antennas, namely the High Band Antenna (HBA) and the Low Band Antenna (LBA). Within the dense core of LOFAR, the High Band Antennas are further divided into two subsets: HBA0 and HBA1.

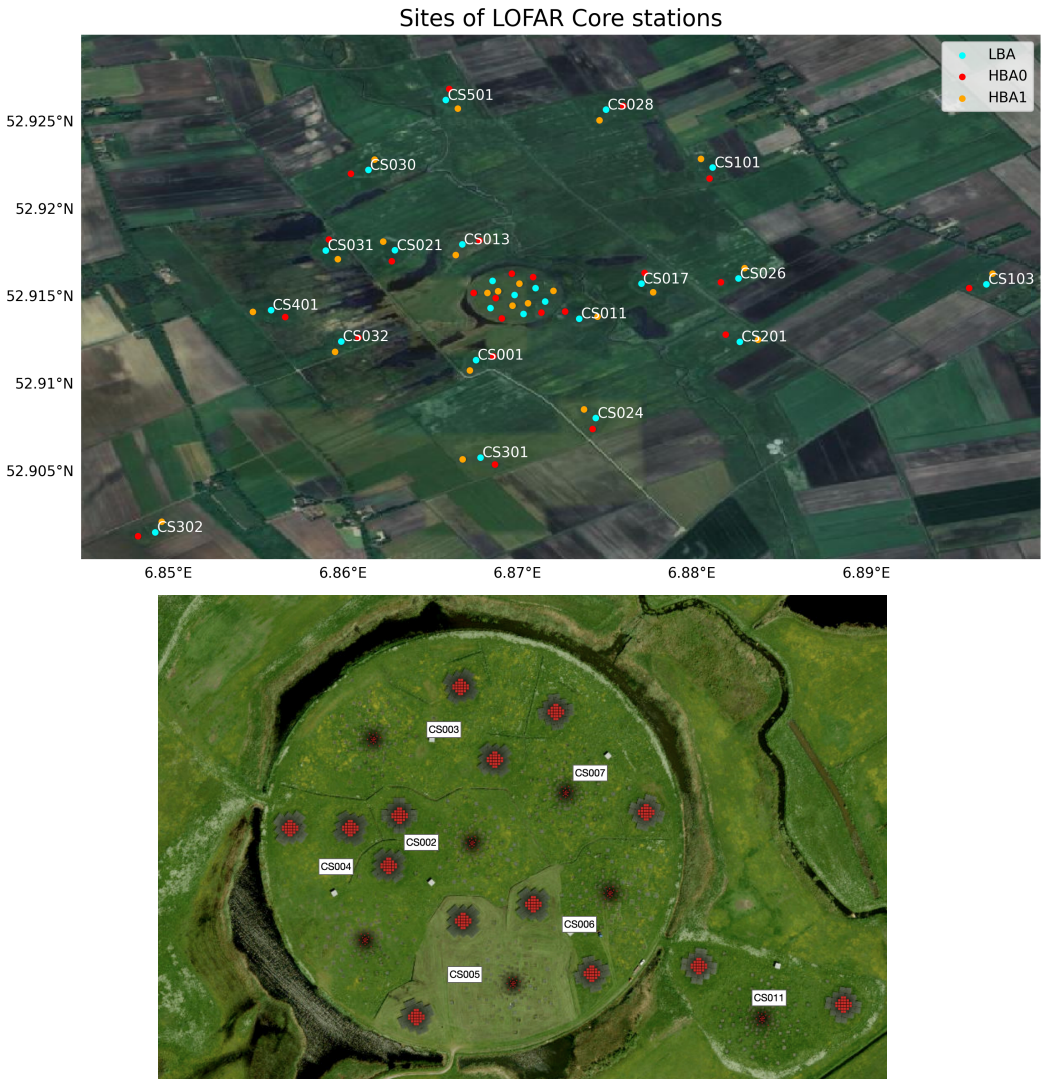



*Figure 2.2. Map of LOFAR Core Stations. In the upper plot, the cyan dots represent the position of the LBA antennas, while the red and orange dots represent the position of the HBA0 and HBA1 antennas, respectively. The lower plot zooms on the "superterp", containing six core stations.*

The spatial configuration of the LOFAR core and remote stations is a critical design element, engineered to optimize the sampling of the uv-plane, the 2-dimensional plane of spatial frequencies that are sampled by the telescope. In radio interferometry, the distribution of samples in this plane is fundamental to the instrument's performance (Thompson et al., 2017).

According to the van Cittert-Zernike theorem, each baseline formed by a pair of antennas measures a single complex visibility. This visibility corresponds to a specific Fourier component of the sky's brightness distribution at a coordinate in the uv-plane. The completeness and density of the resulting uv-coverage directly determine the characteristics of the synthesized beam, the instrument's point spread function (PSF), and thus the fidelity of the final image. A dense and uniform coverage is paramount for minimizing imaging artifacts and achieving high dynamic range.

The LOFAR array geometry was specifically designed to provide a high density of shortest baselines. This ensures sensitivity to astronomical sources exhibiting large angular scales, such as diffuse galactic emission or extended radio halos. Such structures are probed by the lowest spatial frequencies and would be resolved out, i.e., spatially filtered and lost, by an array dominated by longer baselines.

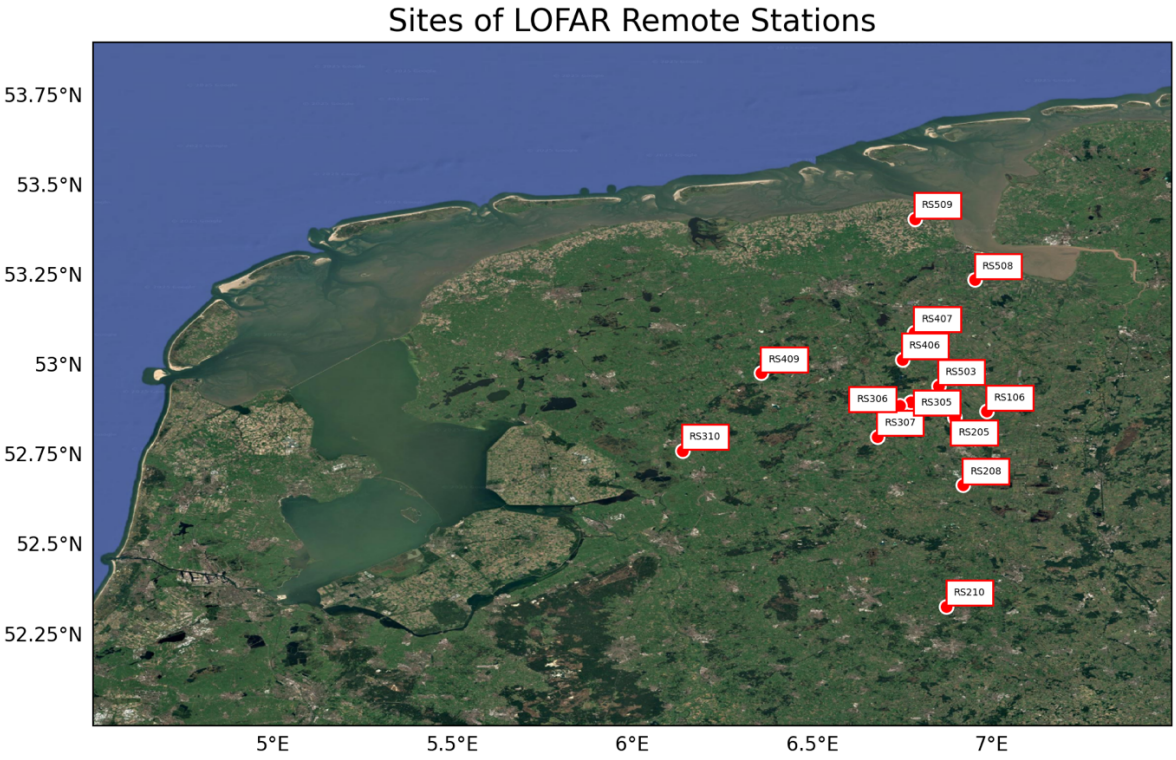



*Figure 2.3. Map of LOFAR Remote stations*

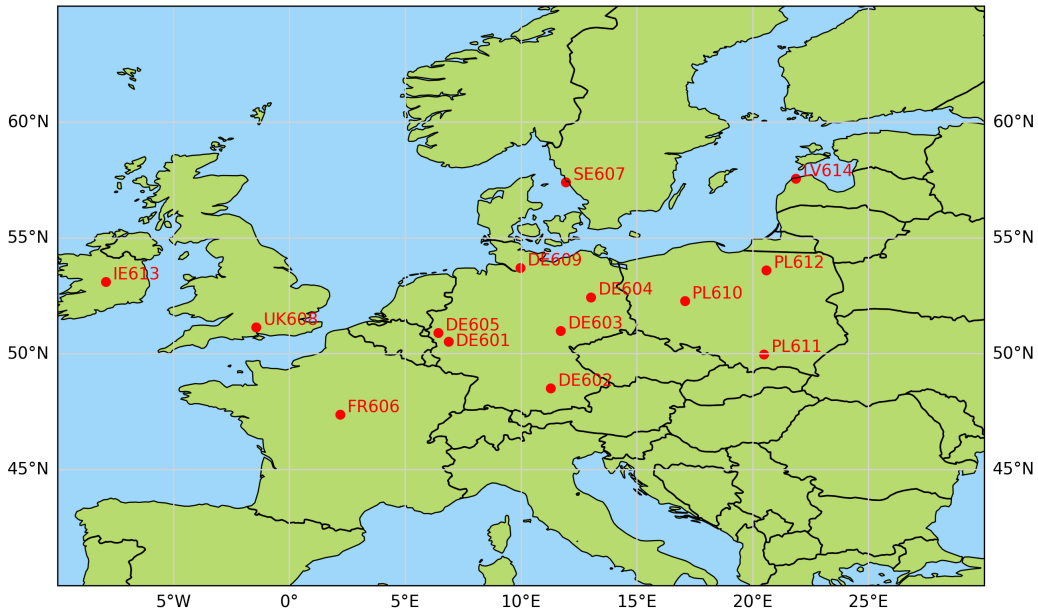



*Figure 2.4. Map of LOFAR International stations*

Each LOFAR station includes a large number of individual antennas sensitive to two orthogonal linear polarisations of the signal of the radio sources. For the analysis in my research, the power measured

in each direction is then combined in a single total intensity, to obtain data that do not depend on the direction of the single antenna with respect to the ground. This process makes it possible to easily compare the data extracted from different antennas, to obtain the global measure of the specific station. In total, more than 20000 antennas are spread over Europe. Contrary to traditional dish telescopes, these antennas do not have moving parts, therefore pointing and tracking are carried out by combining the signals acquired by each antenna to form a phased array.

LBAs are designed to operate from the atmospheric spectral cutoff of the "radio window" at 10 MHz up to the onset of the commercial FM radio band at 90 MHz. One LBA antenna consists of a simple dual-dipole, sensitive to two orthogonal linear polarisations (X and Y), and places above a conducting ground plane with the wires at an angle of 45 degrees with respect to the ground, as shown in figure 2.5a.

The median averaged measurable power spectrum of each antenna is shown in figure 2.5b. The peak is positioned around 58 MHz. It is noteworthy that some frequencies, particularly the lowest ones, present strong RFI. For this reason, and for the proximity of the FM band at the upper end, this range is usually operationally limited to 30–80 MHz.

HBAs, on the other hand, are designed to operate in the frequency range between 110 and 240 MHz. At these frequencies, sky noise no longer dominates the total system noise, as is the case for the LBAs. Consequently, a different design was required to minimise contributions to the system noise due to the electronics. Each HBA "tile" is an assembly of 16 bow-tie-shaped dual dipole antennas arranged in a 4x4 grid, as shown in figure 2.5c. For HBAs antennas the peak measurable power is positioned near 170 MHz, as shown in figure 2.5d.

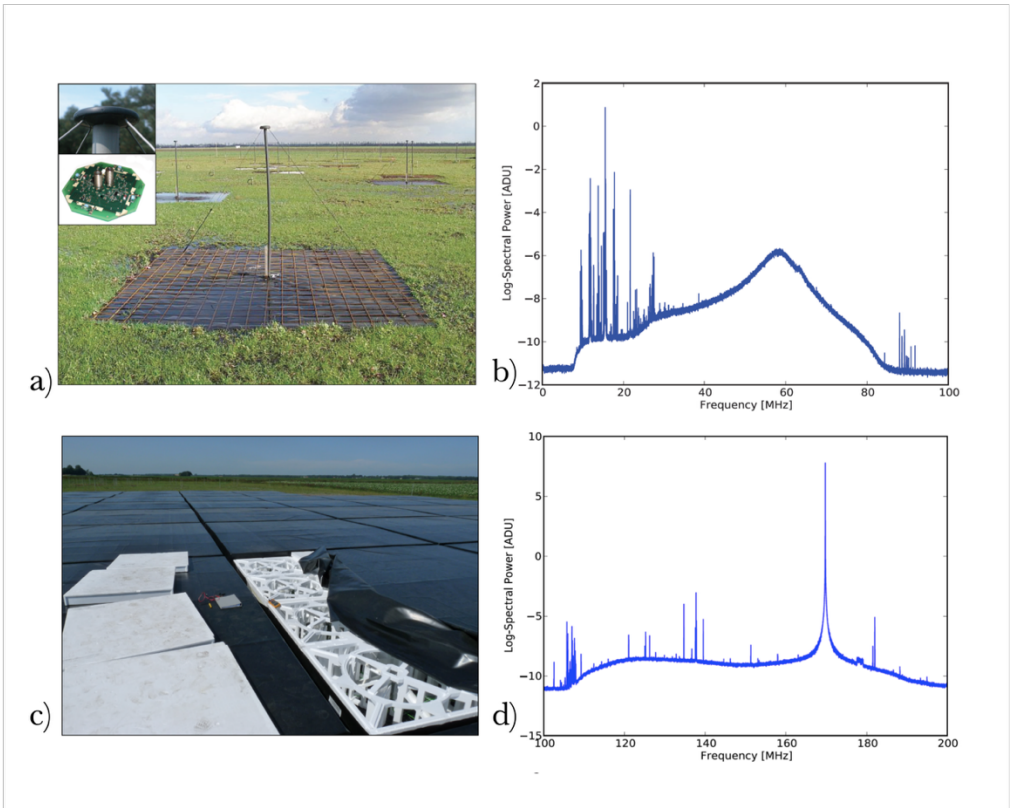



*Figure 2.5. Picture (left panels) and responses (right panels) of LOFAR LBA (upper panels) and HBA (lower panels), as reported by (van Haarlem et al., 2013). Specifically, the right panels represent the median averaged spectrum for all tiles of a single station.*

Each Dutch station includes 48 HBAs and 96 LBAs, whereas each international station includes 96 HBAs and 96 LBAs to grant extra sensitivity to the longest interferometric spacings.

Despite the configuration of each core, remote or international station follows the same characteristic distribution of the antennas, as shown in figure 2.6, each station presents a different global rotation. In fact, the beam recorded by each antenna could present a side-lobe structure. To reduce this problem, the orientation of each station, at the time of construction, was meticulously decided so that each couple of stations presents a different rotation and therefore reduce the effect of bright off-axis sources.

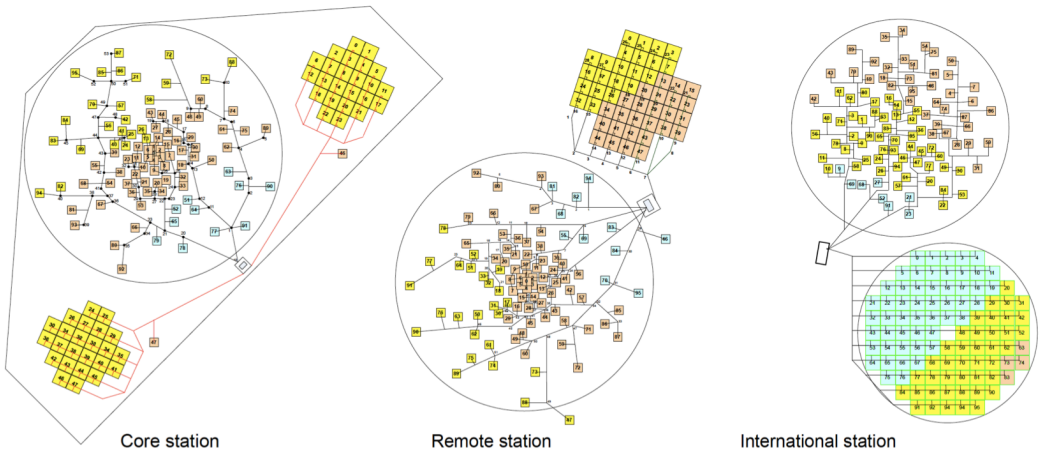



*Figure 2.6. Distribution of HBAs and LBAs within each core, remote, and international station (van Haarlem et al. (2013))*

### 2.1.2. Radio Frequency Interference

Operating within the VHF and lower UHF bands, LOFAR is inevitably exposed to a complex RFI environment. For the LBA, the primary sources of interference are man-made signals from the commercial FM broadcast band (88–108 MHz) at the upper end of the spectrum, and long-range RFI reflected by the ionosphere at the lower end (< 30 MHz). To mitigate these effects, the operational bandwidth for ionospheric studies using LBAs is typically restricted to the 30–80 MHz window, where the spectrum is comparatively cleaner. Similarly, HBA observations are subject to interference from digital audio broadcasting and aeronautical communications, though the design of the HBA tiles provides some natural filtering.

RFI mitigation is managed through a multi-tiered approach. At the observatory level, data undergo a standard Data Quality Assessment (DQA) prior to delivery. This automated workflow employs the AOFlagger tool (Offringa et al., 2010), which utilizes the SumThreshold method to detect and flag RFI at high time-frequency resolution. The DQA process generates detailed inspection plots, including time-frequency diagrams and power spectra, allowing for a preliminary validation of the observation's spectral integrity and the excision of gross interference.

Building upon this standard pipeline, the research presented here applies robust signal processing techniques to mitigate residual or faint RFI that may persist after flagging. Specifically, the cross-correlation algorithm employed for velocity reconstruction utilizes a Fast Fourier Transform (FFT) convolution approach. This method is highly resistant to fast, unphysical data spikes typical of local RFI, which manifest as broadband intensity jumps distinct from the coherent, wave-like patterns of ionospheric scintillation. Furthermore, the normalization of dynamic spectra using a sliding median filter effectively removes slow variations and persistent narrowband RFI, ensuring that the calculated scintillation indices reflect genuine plasma turbulence.

### 2.1.3. Normalised Intensity and S4

One of the primary datasets obtained from the LOFAR stations and utilised in this study are the dynamic spectra. A dynamic spectrum is a two-dimensional visualisation that displays the intensity of a radio signal as a function of time (x-axis) and frequency (y-axis). This representation is crucial for analysing evolving radio phenomena, as it captures the spectral and temporal evolution of the emission from the radio source and the interferences that affects the measured signal. An example of a LOFAR dynamic spectrum is shown in figure 2.7a.

The LOFAR dynamic spectra are mainly needed to detect transient signals like the sun or pulsars but can also allow to obtain a detailed look into trans-ionospheric radio propagation, particularly focusing on scintillation effects. In this thesis, the dynamic spectra present, for computational capabilities reasons, a resolution of 0.195 kHz in frequency and 1 s in time, even if the original data were recorded at a higher temporal resolution (van Haarlem et al., 2013).

A key parameter derived from these dynamic spectra is the $S_4$ scintillation index (Yeh & Liu, 1982). In a general context, the $S_4$ index is a measure of the intensity of the amplitude scintillation. It is a statistical descriptor of the rapid fluctuations in a signal's intensity caused by propagation through a turbulent medium, such as the Earth's ionosphere.

Namely, the $S_4$ index is the standard deviation of the received signal power I normalized by its mean value and is used to measure amplitude scintillation over a specific time interval. $S_4$ equation is given by

$$S_4 = \frac{\sigma_I}{< I >} = \frac{\sqrt{< I^2 > - < I >^2}}{< I >} \tag{2.1}$$

For LOFAR, the extraction of intensity measures from the raw data collected by the stations is not straightforward and the mathematical aspects of this will be discussed in chapter 3.

An example of an $S_4$spectra is shown in the lower panel of figure 2.7, as extracted from the LOFAR dynamic spectrum of the corresponding upper panel. A higher $S_4$ value indicates stronger scintillation. This index is a fundamental tool in space weather and geophysics for quantifying ionospheric irregularities and plasma turbulence. While the GNSS ionospheric community commonly calculates $S_4$ over 60-second interval (Bougard et al., 2011), the LOFAR data sometimes also employs a 180-second window. This ensures that the calculation interval exceeds the typical cycle period of the observed scintillation variations (Wood et al., 2024).

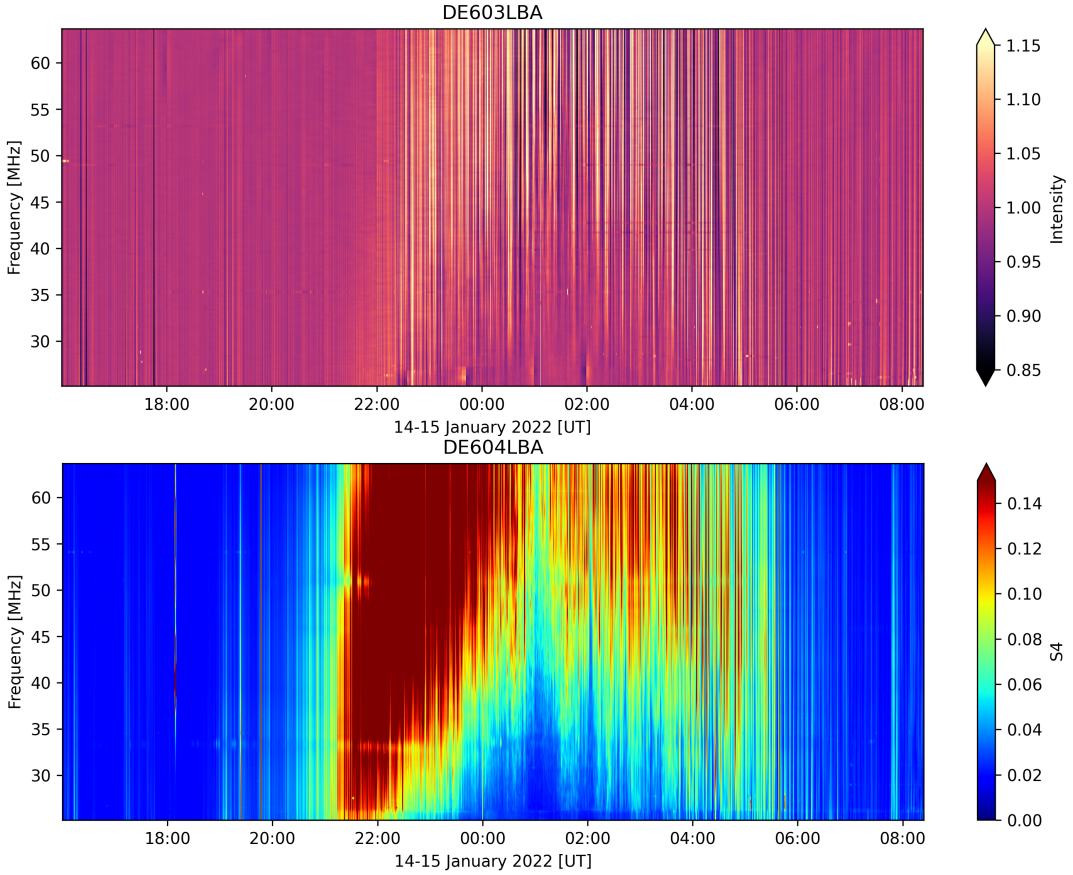



*Figure 2.7. Example of dynamic spectra from LOFAR German Station 603 (upper panel) and the associated S4 measured at 60 s (lower panel). The data were recorded between 16:00 UT of January 14$^{th}$, 2022 and 08:00 UT of January 15$^{th}$, 2022*

### 2.1.4. Mutual benefits between LOFAR and Ionosphere

The relationship between LOFAR radio astronomy and ionospheric science has, in the last years, become interdependent. It turned a significant observational challenge for one field into a unique scientific opportunity for the other.

For astronomers using LOFAR, the Earth's ionosphere is one of the most significant source of signal corruption, a problem that is particularly acute at the low frequencies in which LOFAR operates. The primary task of a radio interferometer like LOFAR is to coherently combine signals from dozens of stations spread across Europe. However, the ionosphere introduces direction-dependent phase errors that corrupt the wavefront of incoming astronomical signals. These phase distortions prevent the signals from being combined perfectly, which degrades the instrument's synthesized beam and corrupts the sampling of the uv-plane, a crucial step in image formation. The direct consequence of these phase errors are severe imaging artifacts, a loss of angular resolution, and significant positional errors for celestial sources (Gasperin et al., 2019a).

Beyond phase corruption, the ionosphere also impacts the amplitude and polarization of radio signals. As the signals traverse Fresnel's scale plasma irregularities, they undergo diffractive scattering, which leads to rapid fluctuations in signal strength, a phenomenon known as ionospheric scintillation. This is analogous to the twinkling of starlight, and for radio astronomy, it can cause a significant loss of

sensitivity, making it difficult to detect faint or diffuse astronomical structures. Furthermore, the interaction between the radio waves and the Earth's magnetic field within the ionospheric plasma causes Faraday rotation, which alters the signal's polarization (Sotomayor-Beltran et al., 2013)

To overcome these formidable challenges, the radio astronomy community has invested heavily in developing sophisticated calibration techniques designed to precisely model and remove these ionospheric effects (Edler et al., 2021). Given that the ionosphere is not a monolithic screen but a dynamic structure, these corrections must be direction-dependent and applied in near-real-time. This requires complex algorithms to describe the ionospheric state across the telescope's wide field of view. The success of any LOFAR observation is therefore critically dependent on the effectiveness of this ionospheric calibration, which is a major data processing effort (Gasperin et al., 2019b).

However, this symbiotic usage is not without its limitations. Unlike dedicated space weather monitors that provide continuous, global coverage, LOFAR's ionospheric data is fundamentally opportunistic, restricted to the specific times and directions of astronomical observation schedules. Furthermore, the quality of the derived ionospheric parameters is heavily dependent on the signal-to-noise ratio of the target source; as detailed in the climatological analysis (Chapter 4.3), robust velocity reconstruction is primarily feasible only when observing the brightest celestial sources, such as Cassiopeia A. Finally, standard calibration algorithms are designed to minimise phase errors rather than preserve physical truth. They often employ simplified models—such as a static thin screen at a fixed altitude—which, while sufficient for image sharpening, can mask complex vertical structures like the extreme uplift events identified in this research.

This necessity, however, has an extraordinary scientific benefit for upper-atmosphere geophysics. The very solutions and calibration data produced to "clean" the astronomical images are a rich and unprecedented source of information about the ionosphere itself. The calibration process generates specific data products that are invaluable for ionospheric research. These include detailed, time-resolved maps of TEC (Mevius et al., 2016) and the raw dynamic spectra that show the intensity of the radio signal as a function of time and frequency. From these spectra, quantitative measures of scintillation, such as the $S_4$ index, can be calculated and directly compared with data from traditional instruments like GNSS receivers. This effectively transformed LOFAR into a powerful, distributed sensor for the upper atmosphere.

The result is a powerful synergy where the astronomers' "noise" becomes the geophysicists' "signal." This process allows for the detailed characterization of ionospheric structures and their dynamics with a sensitivity and resolution that traditional instruments often cannot match. For instance, the dense configuration of LOFAR's core stations enables the tracking of ionospheric irregularities and the reconstruction of their velocity, a central method employed in this thesis. This capability opens new avenues for studying phenomena like TIDs (Boyde et al., 2022; Fallows et al., 2020), the evolution of plasma turbulence, and the ionospheric response to geomagnetic storms (Ghidoni et al., 2025a; Ghidoni et al., 2025b).

Conversely, the expertise of ionospheric physicists offers tangible benefits to the radio astronomy community. By providing a detailed physical characterisation of the 'noise' (e.g. the morphology, altitude, and dynamics of plasma irregularities) physicists can assist in the development of more sophisticated calibration models. For instance, understanding the specific anisotropy of field-aligned irregularities or the spectral characteristics of TIDs allows for calibration constraints that are physically motivated rather than purely mathematical. Furthermore, ionospheric monitoring and

forecasting capabilities can directly support telescope operations. As demonstrated in this thesis, metrics derived from geomagnetic and ionospheric indices can serve as precursors for predicting periods of extreme ionospheric clarity or disturbance. This enables 'smart scheduling' of observations, ensuring that the most sensitive, low-frequency astronomical campaigns are targeted during windows of optimal stability, thus maximising the scientific throughput of the instrument.

This symbiotic relationship transforms LOFAR from a dedicated astronomical observatory into a dual-use facility, providing invaluable data for both astrophysics and space weather research. It stands as a prime example of how solving complex engineering and data processing challenges in one scientific domain can directly fuel new methods and discoveries in another. The ongoing collaboration between the astronomical and geophysical communities is therefore essential for maximising the scientific return of the instrument, ensuring that every observation not only peers deeper into the cosmos but also enhances our understanding of the Earth's immediate space environment.This relationship has been formalised and actively fostered by the recently constituted LOFAR Ionospheric Research Group (LIRG). The LIRG, which I am a part of, is a dedicated working group within the collaboration that brings together astronomers and geophysicists. Its primary goal is to develop and refine the methods needed to exploit LOFAR's calibration data, effectively creating a pipeline that transforms an astronomical calibration problem into a robust source of data for ionospheric and space weather research. For instance, the dense configuration of LOFAR's core stations enables the tracking of ionospheric irregularities and the reconstruction of their velocity, a central method developed by the author as part of the LIRG's efforts and employed in this thesis.

## 2.2. Companion Dataset

Because of the ionosphere’s variability across spatial and temporal scales, as well as its coupling with both the lower atmosphere and the magnetosphere, its study necessarily requires a multi-instrumental approach. No single instrument can capture all the relevant physical parameters or resolve the full range of ionospheric phenomena. Therefore, I based my research not only on the data obtained from LOFAR, but on a diverse set of more traditional tools, both ground-based and space-borne, that provide complementary observations. Ground-based instruments (e.g., ionosondes, magnetometers, GNSS receivers) can provide long-term, high-temporal resolution data from fixed locations, which is essential for monitoring local and regional variations. Space-borne instruments (e.g., instruments onboard ESA’s Swarm and DMSP satellites), on the other hand, offer global coverage and in-situ measurements at ionospheric altitudes, critical for capturing large-scale structures and dynamics. In the following sections, I will describe in detail some of the most widely used traditional instruments in ionospheric science that have been used in this thesis. Each of these plays a unique role in characterizing different aspects of the ionosphere, contributing to a more comprehensive understanding of this vital atmospheric region and its effects on radio propagation.

### 2.2.1. GNSS

Global Navigation Satellite System (GNSS) refers to the collective set of satellite-based positioning and navigational systems operated by different countries around the world. It includes the Global Positioning System (GPS) developed by the United States, Globalnaya Navigatsionnaya Sputnikovaya Sistema (GLONASS) by Russia, Galileo by the European Union and BeiDou by China.

Together, these constellations provide continuous, global coverage, enabling high-precision positioning and timing services.

Many more constellations for navigation are operating besides GNSSs, broadcasting navigation signals at a regional scale (Regional Navigation Satellite Systems (RNSS) such as Japan's Quasi-Zenith Satellite System (QZSS), Indian Regional Navigation Satellite System (IRNSS) (also known as NAVigation with Indian Constellation (NavIC)), European Geostationary Navigation Overlay Service (EGNOS), America's Wide Area Augmentation System (WAAS) and China's Beidou regional.

Over the last 20 years alone, the number of operational GNSS satellites have increased from only 44 satellites in 2002, to 123 satellites as of 2022 (Purfürst, 2022). This huge increment in the number of satellites has direct benefits not only to the navigation and timing users, but to other applications that utilize the GNSS signals.

Despite the different operational characteristics, the different systems have similar basic structures. The co-existence of multiple system with similar capabilities has, therefore, pushed for the creation of multi-GNSS or multi-constellation receivers, which can measure signals coming from multiple systems simultaneously.

The map showing the location of the receivers used in this thesis are reported in the upper panel of figure 2.8. It is possible to notice how much denser the ground-based stations are with respect to the LOFAR antennas, which position is reported in figure 2.4. The GNSS receivers data are provided by the National Land Survey Finland (https://www.maanmittauslaitos.fi/en/finpos/rinex), SWEPOS Sweden (https://www.lantmateriet.se/en/geodata/gps-geodesy-and-swepos/lantmateriets-doi-objects/swepos-rinex-data/), Norwegian Mapping Authority (Kartverket, https://www.kartverket.no/en/on-land/posisjon/guide-to-etpos), and by the "Archivio Dati GNSS Centralizzato" of INGV (ftp://gnssgiving.int.ingv.it), which collects GNSS data from eighty networks in the Euro-Mediterranean region and Africa.

The GNSS satellites, that fly at an altitude of ~20000 km above the sea level (Medium Earth Orbit, MEO), can transmit multiple signals in the frequencies dedicated to Radio Navigation Satellite Services, i.e. at around 1-2 GHz (L-band), carrying memory of the ionospheric portion they crossed. The specific frequencies are illustrated in the lower panel of figure 2.8.

The multi-frequency, multi-constellation and multi-infrastructure synergy has significantly improved the robustness, accuracy, and reliability of positioning, especially in challenging urban or natural environments where satellite visibility can be limited.

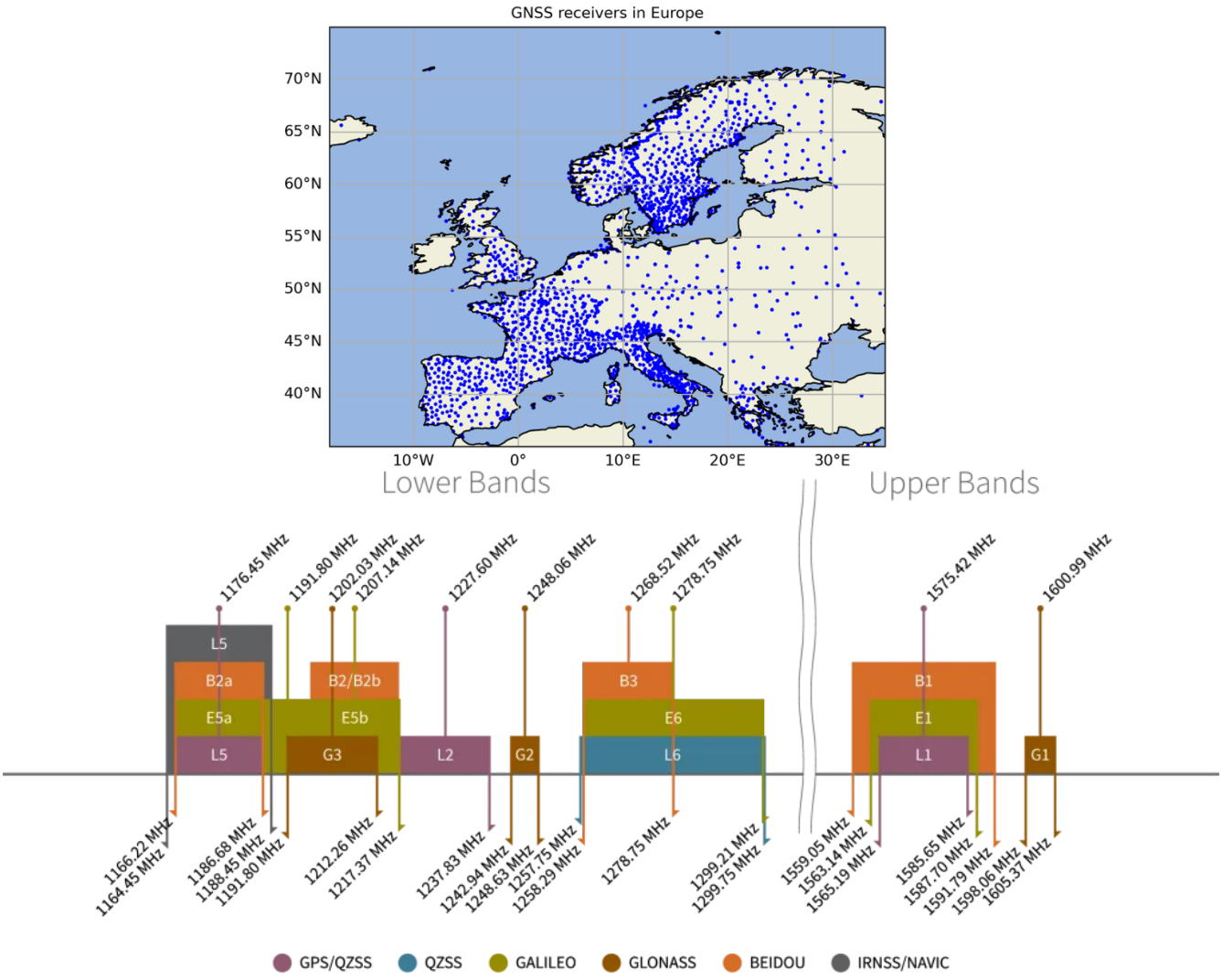



*Figure 2.8. Upper panel shows the location of all the multi-satellite GNSS receivers utilised in this thesis. Lower panel presents the navigational frequency bands for available GNSS/RNSS. Image from GNSS Constellations, Radio Frequencies and Signals. https://www.tallysman.com/gnss-constellations-radio-frequencies-and-signals/, April 2022.*

Due to their capability of transmitting multiple signals at different frequencies, the GNSS satellites in the last two decades become the most used instrument to study the ionosphere and for space weather monitoring purposes. For the purposes of this thesis, the trans-ionospheric GNSS signals provide the data to compute two fundamental metrics that characterize the ionospheric state.

The first metric is the Total Electron Content (TEC), which is a key parameter that quantifies the total number of free electrons in a one-meter-squared column along the path from the satellite to the receiver. TEC serves as a measure of the large-scale, background ionospheric plasma density and is crucial for monitoring the overall state of the ionosphere.

The second metric, and a primary data product for this work, is the Rate of TEC Index (ROTI). Unlike TEC, ROTI is not a measure of the total plasma, but rather a measure of its turbulence and serves as a direct proxy for phase scintillation. It is the standard deviation calculated from the time derivative of TEC (known as the Rate of TEC, or ROT), which is derived from the rapid fluctuations in the raw GNSS signals. ROTI specifically quantifies the intensity of small- to medium-scale ionospheric irregularities, and high ROTI values are indicative of a highly turbulent plasma environment.

In this study, ROTI is the main GNSS-derived product used for direct comparison with LOFAR's S4 scintillation index, allowing for an assessment of how these two different systems respond to the same ionospheric scale of the irregularities, of few kilometres. A comprehensive description of the mathematical methodology used to derive both calibrated TEC and the ROTI index from raw GNSS observables is provided in Chapter 3.

It is important to note that GNSS signals can also be used to measure the amplitude scintillation index (S4) directly, just as LOFAR does. However, computing a reliable S4 index from GNSS requires specialised, high-rate (e.g., 50 Hz or 100 Hz) instrumentation known as Ionospheric Scintillation Monitoring Receivers (ISMRs). These high-rate receivers are distinct from the more common geodetic receivers (which typically sample at 1 Hz or 30-second intervals) that constitute the vast majority of permanent global networks.

This relative sparsity of ISMRs, particularly over the European sector, makes a large-scale, direct comparison between GNSS-derived S4 and the S4 measured across the dense LOFAR array challenging. Therefore, to quantify ionospheric turbulence using the widely available geodetic receiver data, this thesis uses a different, but related, metric: the Rate of TEC Index (ROTI)

### 2.2.2. Ionosondes

An ionosonde is a specialised High-Frequency (HF) radar used to remotely sense the Earth’s ionosphere. The fundamental principle, pioneered by Breit and Tuve in the 1920s, involves transmitting a short radio pulse vertically upwards and measuring the time delay of the reflected echo from the ionospheric layers. The instrument sweeps through a range of frequencies, typically from 1 to 20 MHz. The development of ionosondes has progressed from early analog systems to highly sophisticated digital instruments, such as the AIS-Ionosonde (Zuccheretti et al., 2003), Digisonde (Reinisch et al., 2009) and Dynasonde (Rietveld et al., 2008) and reference therein, which began to emerge in the 1970s. These modern systems use advanced signal processing techniques, including pulse compression, to achieve higher resolution and greater accuracy in their measurements.

The primary output of an ionosonde is the ionogram. This is a two-dimensional plot that displays the apparent or "virtual" height of the ionospheric layers as a function of the radio wave frequency.

An ionosonde can only measure the virtual height of the ionosphere, rather than the true geometric height, due to the nature of radio wave propagation through a dispersive, ionised medium. When a HF radio wave is transmitted vertically into the ionosphere, it slows down progressively as it encounters increasing electron density with altitude. As a result, the wave is refracted and eventually reflected to the ground. The ionosonde calculates the height of this reflection point by assuming that the wave travelled at the speed of light in a vacuum both to the ionosphere and back. However, since the actual speed of propagation is reduced in the ionised medium, the time delay results in an overestimation of the wave's travel distance. This overestimated distance is referred to as the virtual height, which

represents the apparent altitude from which the radio wave seems to have reflected, under the assumption of straight-line travel at the vacuum speed of light.

An example of a typical ionogram is shown in figure 2.9. The vertical axis represents the virtual height (in km), and the horizontal axis represents the frequency (in MHz). Ionograms show distinct traces corresponding to reflections from the different ionospheric layers, such as the E, F1, and F2 layers. By analysing the shape and features of these traces, scientists can determine key ionospheric parameters, including:

- Critical frequencies (foE, foF1, foF2): The highest frequency at which a radio wave is reflected by a specific layer when transmitted vertically, being proportional to plasma density at the peak of the corresponding layer.
- Virtual heights (h'E, h'F1, h'F2): The apparent altitude of a layer, which is slightly higher than the true height because the radio wave slows down as it propagates through the plasma.

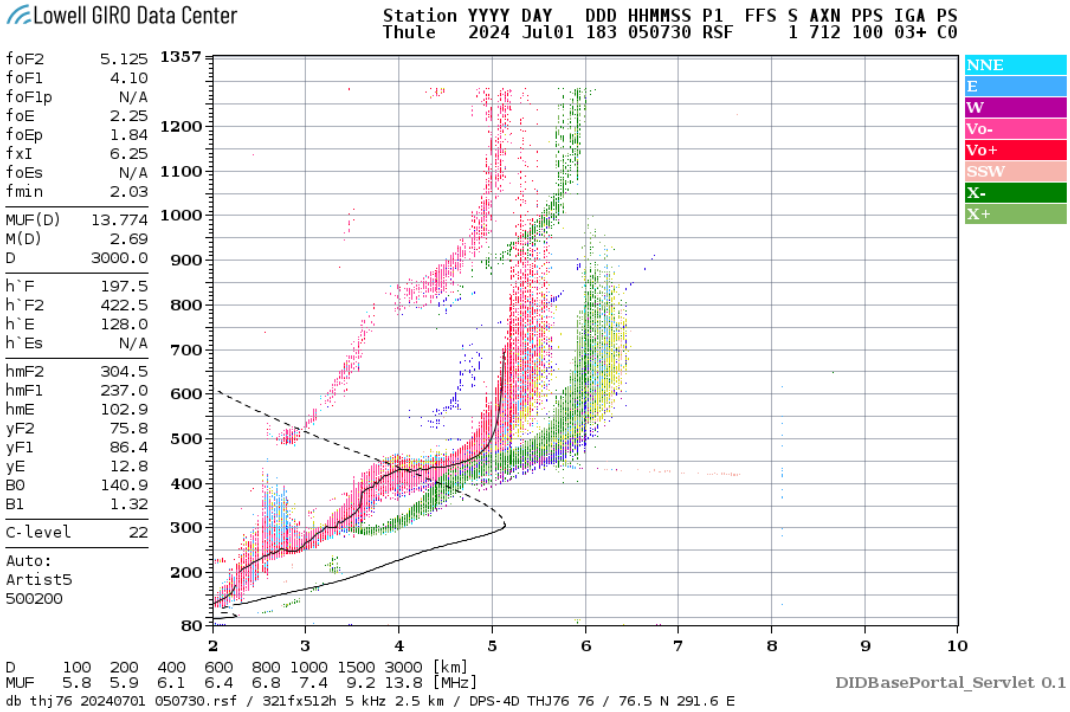



*Figure 2.9. Example of an ionogram from 01-07-2024. From* https://giro.uml.edu

Beyond the standard ionogram, modern digital ionosondes, particularly the Digisonde and other advanced systems, produce more sophisticated data products. These include High-Frequency Doppler-Frequency-Information (HDFI), which provides information on the movement and dynamics of the ionospheric plasma, as shown in figure 2.10. HDFI measures the Doppler shift and angle of arrival of the reflected signals, allowing for the study of plasma drifts, traveling ionospheric disturbances (TIDs), and drifting irregularities in the ionosphere. These advanced data products enable a more comprehensive understanding of the complex, dynamic nature of the upper atmosphere.

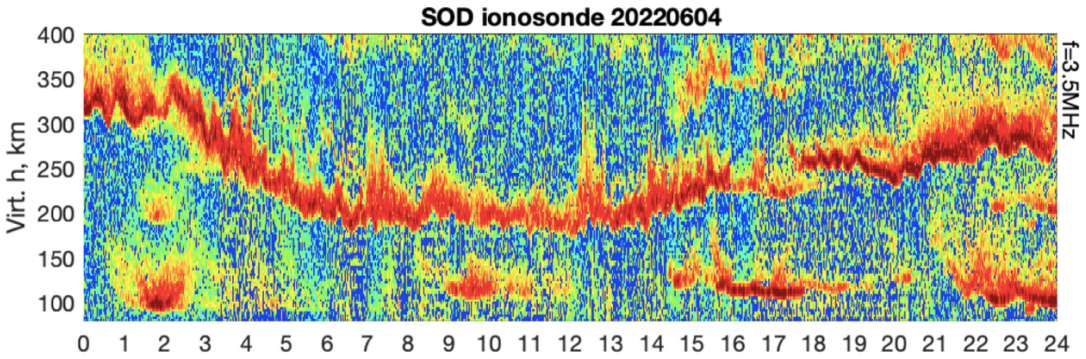



*Figure 2.10. Example of a HDFI from the Sodankyla ionosonde measured June 4th, 2022. From https://www.sgo.fi/pub_ion/IonoDaysView/IonoView_2022/IonoDay_2022_01_14.pdf*

The monitoring of the ionosphere relies on a global network of ionosondes. Several international collaborations and data centers, such as the Global Ionospheric Radio Observatory (GIRO, (Reinisch & Galkin, 2011) operated by the University of Massachusetts Lowell, collect and disseminate data from stations worldwide. This network is crucial for space weather monitoring and research, providing continuous, real-time data on the state of the ionosphere.

The European sector is home to a robust and well-integrated network of ionosonde stations. This network has been strengthened through collaborative projects like the European Digital Upper Atmosphere Server (DIAS) and the Plasmasphere Ionosphere Thermosphere Integrated Research Environment and Access services: a Network of Research Facilities (PITHIA-NRF) project (Belehaki et al., 2025)which aimed to integrate various observing facilities, including ionosondes, to provide a comprehensive view of the upper atmosphere.

In this research, ionosonde data provides essential context on the background state of the ionosphere, such the altitude of strong ionospheric irregularities, as presented in Chapter 4, their operational limitations during extreme storm conditions serve to underscore the unique observational capabilities of LOFAR.

### 2.2.3. Magnetometers

Magnetometers are instruments designed to measure the strength and the direction of a magnetic field. In the context of space physics and geophysics, they are crucial for monitoring the Earth's magnetic field, a dynamic entity influenced by both internal (geodynamo) and external (solar wind-magnetosphere interaction) processes. In the ionospheric physics domain, they are also helpful for the determination of the current systems flowing in the ionosphere, mostly at E-layer altitudes (~120 km). The fundamental principle behind most magnetometers is based on the interaction of a magnetic field with a sensitive material or an electronic circuit.

Various types of magnetometers exist, each with its own advantages and applications. Fluxgate magnetometers, for instance, are widely used in ground-based networks. They operate by sensing the magnetic field using a ferromagnetic core with a coil. By driving the core into saturation with a known current, any external magnetic field will alter the saturation time, and this change can be precisely measured. Proton precession magnetometers, on the other hand, measure the total magnetic field strength by exploiting the gyromagnetic properties of protons. When a strong magnetic field is briefly applied to a sample of water or another proton-rich fluid, the protons align. When the field is removed, the protons precess at a frequency directly proportional to the ambient magnetic field strength.

The data acquired by magnetometers is typically a time series of the magnetic field components, usually expressed in a coordinate system such as the XYZ, where X is north, Y is east, and Z is vertically downwards. These measurements are used to detect minute fluctuations in the Earth's magnetic field, which are often indicative of geomagnetic activity. These fluctuations can arise from a variety of sources, including magnetospheric substorms, solar flares, and coronal mass ejections (CMEs). To comprehensively study the dynamic processes in the auroral zone, a network of strategically placed magnetometers is essential. The International Monitor for Auroral Geomagnetic Effects (IMAGE) network (Tanskanen, 2009) is a prime example, providing high-quality, high-time-resolution data from the northern part of Europe. Established in 1991, the network consists of an array of ground-based fluxgate magnetometers spanning from northern Norway and Finland down to Poland. This geographic distribution is key, as it allows for the differentiation of spatial and temporal variations of geomagnetic activity.

The primary function of the IMAGE network is to monitor and study magnetospheric and ionospheric currents, particularly the auroral electrojets. The network's dense coverage in the Scandinavian auroral oval region is invaluable for this purpose (Figure 2.11).

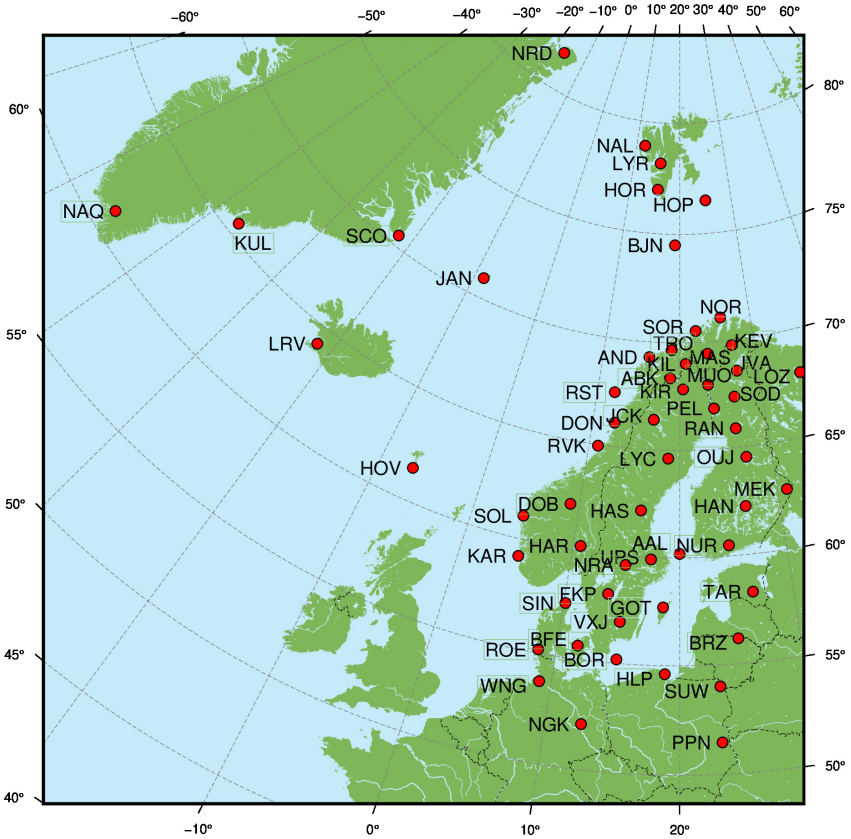



*Figure 2.11. Position of magnetometrs of the IMAGE network*

The magnetometers of the IMAGE network are located at high geographical latitudes to be directly underneath the auroral currents, providing a direct measurement of their magnetic signature. The data from the IMAGE network is made publicly available, enabling researchers worldwide to study phenomena such as geomagnetic substorms, auroral displays, and the response of the magnetosphere to solar wind conditions.

By analysing the perturbations in the X, Y, and Z components, it is possible to reconstruct the overhead current systems responsible for them. The high density and coverage of the IMAGE network allow for the triangulation of these current systems, providing a detailed picture of their spatial and temporal evolution.

In this thesis, magnetometer data and the derived auroral electrojet indices serve a crucial diagnostic role. They are used to characterize the overall geomagnetic conditions and to establish a direct link between the large-scale ionospheric current systems and the small-scale plasma structures observed by LOFAR.

#### *2.2.3.1. Electroject indexes*

The auroral electrojets are intense currents flowing in the ionosphere at altitudes of around 100-150 km. They are a direct manifestation of magnetospheric storms and substorms and play a crucial role in the transfer of energy from the magnetosphere to the ionosphere. The strength and direction of these currents are an important indicator of the level of geomagnetic activity. The Auroral Electrojet (AE) index is a family of indexes designed to quantify this activity (Kauristie et al., 2017).

The AE index is derived from the magnetic field data of a global network of high-latitude magnetometers, including those from the IMAGE network. The fundamental principle is to identify the maximum positive and negative excursions in the horizontal magnetic field component from a baseline value across all stations.

- AU (Auroral Upper) index: Represents the maximum positive deviation, which is primarily associated with the eastward auroral electrojet.
- AL (Auroral Lower) index: Represents the maximum negative deviation, which is associated with the westward auroral electrojet.
- AE (Auroral Electrojet) index: Defined as the difference between the AU and AL indexes (AE = AU - AL), it represents the total range of auroral electrojet activity.
- AO (Auroral Oval) index: Defined as the average of AU and AL (AO = (AU + AL) / 2), it is a measure of the average magnetic perturbation.

A high value of the AE index signifies strong auroral currents and, consequently, a high level of geomagnetic activity. The AE index is a critical tool for identifying substorm onset and for studying the timing and intensity of magnetospheric processes. The IMAGE network, with its dense coverage of the Scandinavian auroral zone, contributes significantly to the accuracy and resolution of these indices, particularly for the Northern Hemisphere, with a focus on the sector spanned by the field of view of LOFAR stations projected at ionospheric altitudes.

While the AE index provides a valuable global measure of geomagnetic activity, it is often useful to have a more regional index, especially when focusing on a specific geographic area like the northern European sector covered by the IMAGE network. To this end, a set of indices specifically derived from IMAGE data has been developed: the IMAGE Electrojet indexes (IU, IL, IE).

#### *2.2.3.2. Magnetic evolution in time*

The time series data from magnetometers allows for a detailed analysis of the evolution of the magnetic field over various timescales. From seconds to years, these measurements reveal the intricate interplay of solar and terrestrial processes.

**Short-term Variations (Seconds to Minutes)**: High-frequency fluctuations, known as pulsations, can be observed. These are often related to waves propagating through the magnetosphere and ionosphere, driven by interactions with the solar wind.

**Mid-term Variations (Minutes to Hours)**: Substorm activity is characterised by a rapid, large-scale decrease in the H-component of the magnetic field at high latitudes (the AL index), followed by a recovery phase. The IMAGE network is particularly well-suited for tracking the spatial and temporal evolution of the substorm current wedge.

**Long-term Variations (Days to Years)**: These variations are often associated with the 27-day solar rotation cycle and the 11-year solar cycle. The overall level of geomagnetic activity, as indicated by the average AE index, tends to follow the solar cycle, with higher activity during solar maximum. Additionally, long-term trends in the magnetic field can be used to study the secular variation of the Earth's main magnetic field, although this is a much slower process typically studied with a different class of magnetometers and observatories.

### 2.2.4. Swarm

The Swarm mission, a cornerstone of the European Space Agency's (ESA) Living Planet Programme, is a constellation of three identical satellites launched in November 2013 (Friis-Christensen et al., 2008). The primary objective of the mission is to provide an unprecedented high-resolution, multi-point survey of the Earth's magnetic field and its temporal evolution (Figure 2.12). This is achieved by separating the different sources of the magnetic field, from the Earth's core, mantle, and crust to the external sources in the ionosphere and magnetosphere.

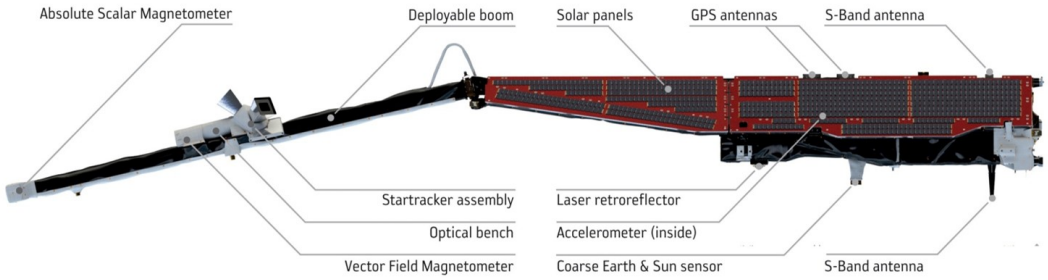



*Figure 2.12. Position of instrument on a Swarm satellite*

The Swarm mission's strength lies in its orbital configuration, which is designed to simultaneously sample the magnetic field and the surrounding plasma environment at different altitudes and local times. This setup allows for the crucial task of disentangling the various sources of the magnetic field.

- Swarm Alpha and Charlie: These two satellites fly in a lower, nearly identical orbit at an initial altitude of approximately 460 km. They fly side-by-side, separated by a longitudinal distance of about 1.4°. This proximity in orbit allows for the differentiation of magnetic field variations that have a short spatial wavelength, such as those originating from the Earth's crust.
- Swarm Bravo: This satellite orbits at a higher altitude of around 510 km. Its orbital plane gradually precesses relative to the Alpha and Charlie pair, allowing it to sample different local times. This multi-point measurement in space and time is essential for separating the magnetic field signals from external sources, particularly those from the dynamic currents in the ionosphere and magnetosphere.

The satellites are in near-polar orbits, with an inclination of about 87.3° for the lower pair and 87.75° for the higher one. This orbital path allows them to survey almost the entire globe, providing comprehensive coverage of the geomagnetic field and the ionospheric plasma environment. Despite being conceived mostly as a magnetic mission, Swarm has been demonstrated to be a precious tool to unveil ionospheric physics (A. Wood et al., 2022).

The in-situ measurement of electron density is one of the crucial data products from the Swarm mission, providing direct information about the state of the ionosphere. The measurements are made by the Electric Field Instrument (EFI) on each satellite. The EFI is a complex instrument, but its core components for plasma measurements are two Langmuir probes and two Thermal Ion Imagers.

The Langmuir Probes the primary sensors for measuring in-situ electron density and electron temperature. The operation of a Langmuir probe is based on the principle of collecting charged particles from the surrounding plasma. A spherical conducting probe is exposed to the plasma, and a voltage is applied to it. By sweeping this voltage and measuring the resulting current, a current-voltage (I-V) characteristic curve is obtained.

The electron density is derived from the "electron saturation" region of the I-V curve, where the probe potential is positive with respect to the plasma potential. In this region, the probe collects almost all electrons that come into its "sheath" region—a thin boundary layer that forms around the probe. The collected current is directly proportional to the electron density and the electron thermal velocity. By applying the Orbital Motion Limited theory to the collected current, the electron density can be precisely calculated.

The LPs on the Swarm satellites operate in a sophisticated "harmonic mode" which allows for very rapid and accurate measurements. This is critical for capturing the fine-scale structures and rapid variations in the ionospheric plasma, such as those associated with plasma irregularities and ionospheric disturbances. The in-situ measurements from the Langmuir probes are often used to validate and complement other ionospheric data products, such as the total electron content (TEC) derived from the on-board GPS receivers.

In summary, the Swarm constellation, with its unique orbital configuration and sophisticated instrumentation, provides a rich dataset for understanding the Earth’s magnetic field and its plasma environment. The in-situ electron density measurements are a cornerstone of the mission’s scientific output, offering a direct and highly accurate view of the dynamic and complex ionosphere.

The in-situ plasma density measurements from the Swarm mission are used in this thesis to provide direct validation of large-scale ionospheric features. Specifically, a satellite overpass is used to characterize the structure of the main ionospheric trough during the geomagnetic storm of January 2022, confirming the plasma environment in which the irregularities observed by LOFAR were generated.

### 2.2.5. Defense Meteorological Satellite Program (DMSP)

The DMSP is a long-running series of U.S. Department of Defense satellites, designed primarily for global weather monitoring to support military operations (Curtis & Adams, 1987). However, a key part of their mission has always been to monitor the space environment. The DMSP satellites are in a near-polar, sun-synchronous orbit at an altitude of approximately 830 km. This specific orbit, which crosses the equator at a constant local time, is ideal for repeatedly surveying the auroral regions and the polar caps, making them a crucial tool for space physics research.

Each DMSP satellite carries a suite of instruments, with two in particular being highly relevant for studying the auroral environment:

The Special Sensor Ultraviolet Spectrographic Imager (SSUSI) (Paxton et al., 2002): It operates in the far-ultraviolet spectrum—specifically between 115 and 180 nm. SSUSI allows scientists to monitor the aurora during both day and night, as these wavelengths are not obscured by reflected sunlight. By scanning cross-track to create a wide swath (approximately 3,000 km), the sensor maps the "auroral oval" and measures the intensity of emissions like the Lyman-Birge-Hopfield (LBH) bands and atomic oxygen lines. These data are critical for characterizing the energy flux and average energy of precipitating electrons, which helps forecasters predict space weather impacts on GPS signals, high-frequency radio communications, and satellite drag. An example of the data provided by DMSP/SSUSI is visible in figure 2.13.

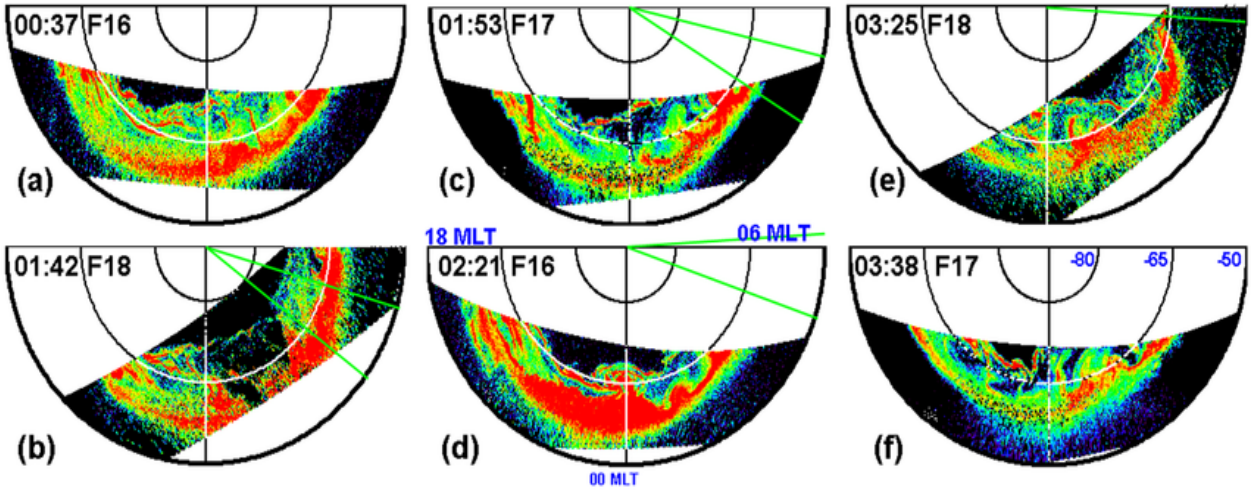



*Figure 2.13. The sequence of auroral images from DMSP SSUSI (Paxton et al., 2002). IMAGE network longitudinal sector is shown by green lines. The development of north-south narrow structures (streamers) and auroral omega bands are observed. From Apatenkov et al., (2020)*

The Special Sensor J (SSJ) instrument (Hardy et al., 1985): This is the core instrument for in-situ plasma measurements. The SSJ is a precipitating particle spectrometer that measures the energy and flux of electrons and ions as they precipitate into the upper atmosphere. It consists of a series of electrostatic analysers that record particles in the energy range from approximately 30 eV to 30 keV. This energy range is precisely where the particles responsible for most of the auroral displays and ionospheric heating reside. The SSJ instrument is crucial for characterizing the plasma environment at the satellite's altitude and for understanding the particle sources that cause the aurora.

Additionally, DMSP satellites carry other sensors, such as the Special Sensor for Ion and Electron Scintillation (SSIES), which measures ambient electron and ion densities, temperatures, and drift velocities, and the Special Sensor Magnetometer (SSM), a triaxial fluxgate magnetometer that measures geomagnetic fluctuations. Together, these instruments provide a comprehensive snapshot of the space environment along the satellite's orbital path.

One of the most significant contributions of the DMSP program to space physics is its ability to reconstruct the global morphology of the auroral oval. The auroral oval is the ring-like region around the magnetic poles where auroral displays are most frequent. Its shape and size are highly dynamic, expanding and contracting in response to changes in the solar wind and interplanetary magnetic field.

The reconstruction of the auroral oval is typically achieved using two main methods based on DMSP data:

Direct Imaging with the SSUSI: The low-light imaging capability of the OLS instrument provides a direct visual representation of the auroral oval's location and shape. As the satellite flies over the polar region, it captures a strip of auroral luminosity. By stitching together images from successive passes, or by using data from multiple DMSP satellites, a composite image of the entire auroral oval can be created. This method is particularly useful for visualizing the overall morphology and identifying key features like auroral arcs and substorm intensifications.

Using Precipitating Particle Data (SSJ): A more quantitative and robust method for defining the auroral oval's boundaries relies on the in-situ measurements from the SSJ instrument. The auroral oval is defined by the region where energetic particles (electrons and ions) from the magnetosphere precipitate down into the ionosphere. The SSJ sensor measures this precipitation directly.

The poleward boundary of the auroral oval is often defined as the point where the satellite crosses from a region of significant particle precipitation (the auroral oval) into the polar cap, where precipitation is typically much lower and softer (less energetic).

The equatorward boundary is defined by the transition from the auroral oval into the mid-latitude region, which is characterised by an abrupt decrease in the flux of precipitating particles.

By identifying these sharp boundaries in the SSJ data along the satellite's track, researchers can pinpoint the location and size of the auroral oval for a given magnetic local time and universal time. Since multiple DMSP satellites are typically in orbit at different local times, their combined measurements can provide a near-instantaneous, multipoint representation of the entire oval. This data is then used in various models and algorithms to mathematically fit the oval's shape, which is often approximated as an eccentric circle or an ellipse in corrected geomagnetic coordinates.

The ability of the DMSP network to provide both visual imagery and quantitative in-situ particle data for the auroral oval makes it an indispensable tool for space weather monitoring and research. It allows scientists to not only observe the beautiful displays of the aurora but also to understand the fundamental magnetospheric processes that drive them.

In my research, DMSP data were employed to improve the understanding of the ionospheric regions primarily responsible for the scintillations affecting LOFAR observations. The use of DMSP measurements made it possible to determine whether the LOFAR ionospheric pierce points (IPPs) were located within the auroral or sub-auroral regions, and consequently to identify the mechanisms responsible for the generation of ionospheric irregularities.

### 2.2.6. International Geomagnetic Reference Field (IGRF)

Another fundamental component of this research is the direction of the Earth's magnetic field. This background field vector is provided by the International Geomagnetic Reference Field (IGRF) model. The IGRF is a standard, collaborative, and widely used mathematical model that describes the large-scale, main magnetic field of the Earth. This "main field" is the component that primarily originates from the geodynamo in the planet's fluid outer core. The model is maintained by the International Association of Geomagnetism and Aeronomy (IAGA) and is updated every five years, providing a definitive set of parameters that represent the field and its slow, long-term changes, known as secular variation. Mathematically, the IGRF is represented as a spherical harmonic expansion. For any given

date and geocentric coordinates (latitude, longitude, and altitude), the model provides a set of standardised Gauss coefficients. These coefficients allow for the modelling of the magnetic field vector B and its components (e.g., North, East, and vertical). In this research, the IGRF 13th Generation model (Alken et al., 2021) is used to determine the vector B of the Earth's main magnetic field at any required point in space, most notably at the calculated Ionospheric Pierce Points (IPPs).

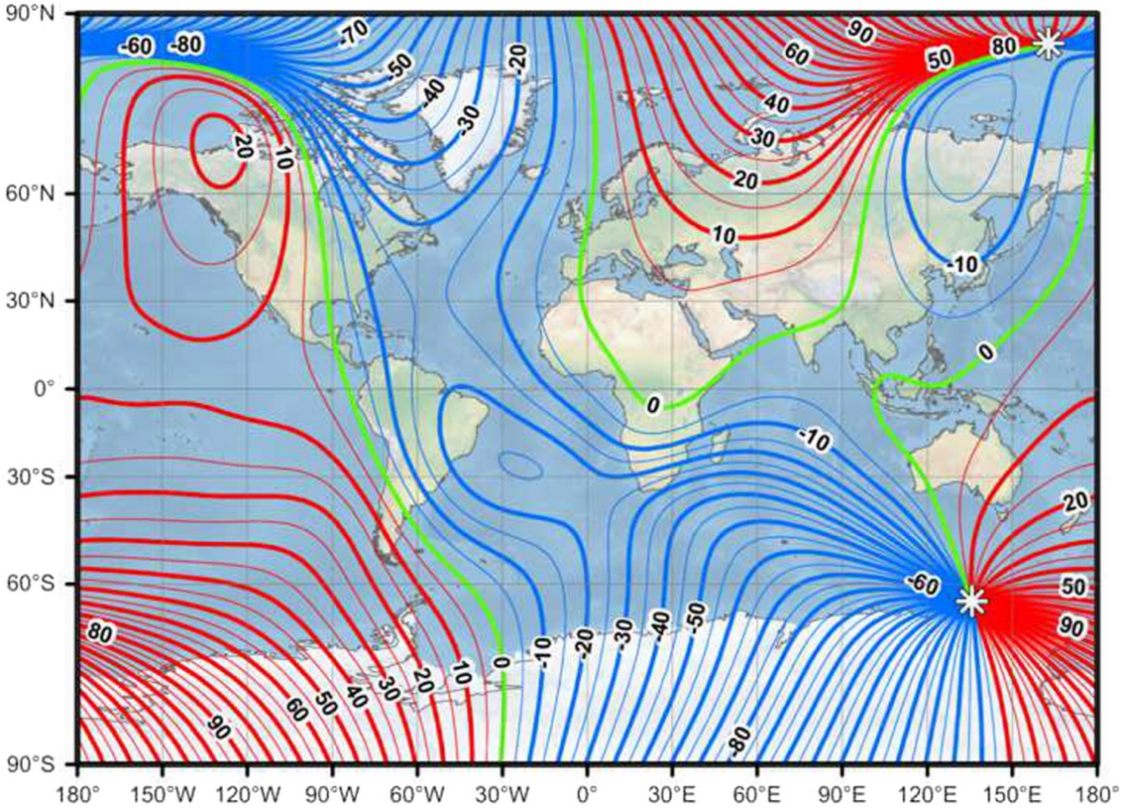



*Figure 2.14. Maps of declination of the modeled magnetic field at the WGS84 ellipsoid surface for epoch 2020. The zero contour is shown in green, positive contours in red, and negative contours in blue. White asterisks indicate locations of the magnetic dip poles. Projection is Miller cylindrical. From (Alken et al., 2021)*

### 2.2.7. Kp Index

The Kp index is a widely-used global geomagnetic activity index (Matzka et al., 2021). It is designed to characterize the magnitude of geomagnetic storms by quantifying the disturbances in the Earth's horizontal magnetic field. The index is "planetary" (the "p" in Kp) because it is derived from a network of 13 mid-latitude/sub-auoral magnetometer observatories distributed around the world, as shown in figure 2.15. This global distribution allows it to average out local-time effects and provide a comprehensive, 3-hour-based summary of the planet's overall geomagnetic activity. It is obtained as the weighted average value of the disturbance levels in the two horizontal field components (K-index), observed at the 13 selected stations. The Kp index is reported on a quasi-logarithmic scale from 0 to 9, where 0 represents profoundly quiet conditions and 9 signifies an extreme geomagnetic storm.

In this thesis, the Kp index is used as a standard, high-level index of the onset and severity of the geomagnetic storms being analysed.

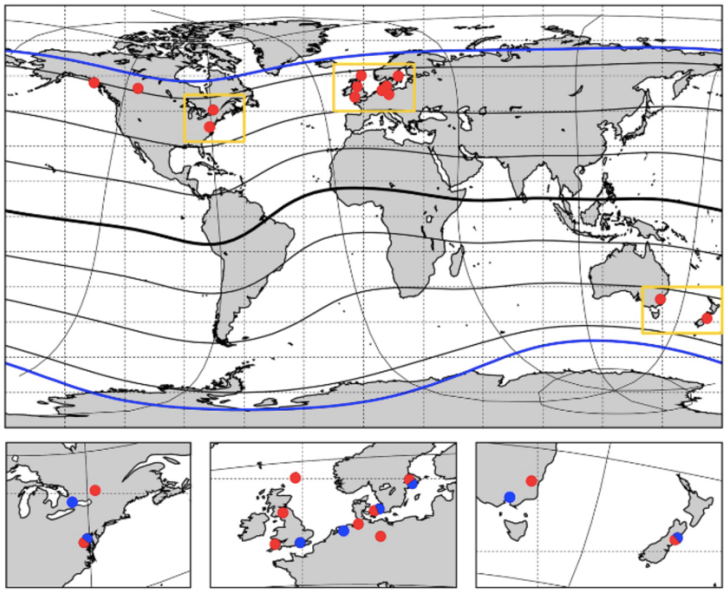


*Figure 2.15. World map of the 13 current Kp-stations (red dots, see also Table 2) with geographic coordinates (dotted lines), QD coordinates (solid lines), geomagnetic equator (thick line at 0° QD latitude) and auroral zones (blue lines at +67° and −67° QD latitude). From (Matzka et al., 2021)*

## 2.2.8. Summary

| Instrument / Source | Type / Platform | Frequency / Parameter Range | Spatial Coverage / Position | Key Derived Metrics | Resolution / Sampling |
|---|---|---|---|---|---|
| LOFAR (Low Frequency Array) | Radio Interferometer (Ground-based) | 10 – 240 MHz(LBA: 10-90 MHz, HBA: 110-240 MHz) | Europe (Mainly Netherlands) | S4, Dynamic Spectra, Velocity | 1s (S4 - 1 or 3 min) |
| GNSS (GPS, Galileo, GLONASS, Beidou) | Satellite Constellation (Ground-based receivers) | L-Band (1 - 2 GHz) | Global | TEC, ROTI, dTEC | 30s (ROTI - 5 min ) |
| Ionosondes | HF Radar (Ground-based) | 1 – 20 MHz | Global (Focus on European Sector) | h', foE,foF2, Electron Density Profiles | ~5 - 15 min |
| Magnetometers (IMAGE Network) | Magnetometer Array (Ground-based) | Magnetic Field Strength (nT)(DC to low frequency) | Northern Europe | IE, IL, IU | 10s |
| Swarm | LEO Satellites (Space-borne) | In-situ Plasma Density | Global Orbit (Polar) | In-situ Ne and Te | 50 Hz |

| | | | | | |
|---|---|---|---|---|---|
| DMSP | LEO Satellites (Space-borne) | UV Spectrum (115-180 nm) & Particle Energy (30 eV - 30 keV) | Global Orbit (Sun-synchronous) | Auroral Oval Boundary | ~90 min |
| IGRF-13 (Model) | Mathematical Model | N/A (Static field model) | Global | B | N/A (Epoch based) |
| Kp Index | Geomagnetic Index | N/A (Derived from ground magnetometers) | Global | Kp (0-9 scale) | 3-hour interval |

# 3. Mathematical Methods

This chapter details the main mathematical framework and analytical methods employed to process the observational data and derive the key geophysical parameters presented in this thesis. The methodology is central to this work, as it leverages the unique configuration of the LOFAR radio telescope to probe the ionosphere in novel ways.

The chapter begins by establishing the geometric model used to calculate the Ionospheric Pierce Points (IPPs), which are essential for projecting observations onto a specific altitude.

The chapters then move to describing the extraction of ionospheric information from GNSS signals and the fundamental signal model for a LOFAR data. Building upon this foundation, the chapter describes the two primary techniques used to determine the velocity of ionospheric irregularities. The first is a cross-correlation method that leverages the spatio-temporal coherence of signals across the dense array of LOFAR core stations. The second is a complementary approach based on the identification of the Fresnel's frequency from the power spectrum of the signal at a single station.

A central and novel contribution of this work is then presented: a unique algorithm that combines the outputs of these two independent velocity estimation techniques to solve for the effective altitude of the ionospheric irregularity layer. This method provides a dynamic, data-driven estimate of the irregular layer height, a parameter typically assumed in ionospheric analysis.

Collectively, these methods form the analytical backbone of this research, providing the tools necessary to interpret the complex datasets and produce the scientific results discussed in Chapter 4.

## 3.1. Ionospheric Pierce Point

The ionosphere is a complex, three-dimensional medium spanning hundreds of kilometres in altitude. However, to analyse the effect of the ionosphere on trans-ionospheric radio signals, it is necessary to map the ground-based observations to a specific location in the atmosphere. It is standard practice to simplify the ionospheric volume into a single thin screen. This model assumes that all plasma content and irregularities are concentrated in a single, infinitesimally thin spherical shell at a fixed effective altitude $h$ concentric with a spherical Earth of radius $R_E$ (~ 6300 km), as shown in figure 3.1. The Ionospheric Pierce Point (IPP) is defined as the point where the signal's line-of-sight (LoS) from the radio source (celestial body or GNSS satellite) to the ground-based receiver intersects the thin ionospheric layer.

Figure 3.1 shows how the location of the IPP is entirely dependent on the assumed ionospheric height $h$. This height is assumed to be located at the altitude of the F-layer and therefore it is typically located at an altitude of 350 km. This specific altitude is not an arbitrary choice but aligns with the standard convention widely adopted by the ionospheric community (Wood et al., 2024).

However, as I will show in chapter 4, this assumption can be dramatically wrong, for example during geomagnetic storms.

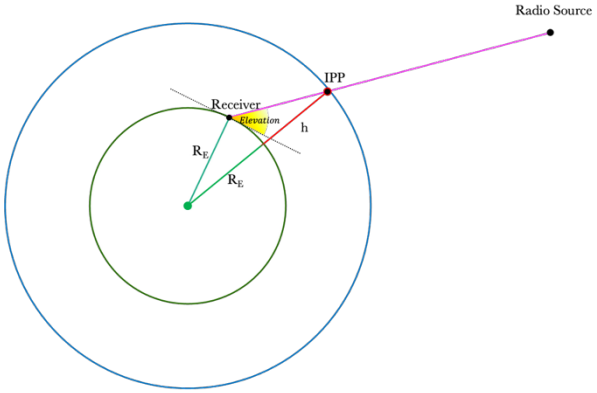



*Figure 3.1. Geometrical scheme of IPP location*

## 3.2. GNSS measurements

### 3.2.1. TEC extraction

TEC is a fundamental parameter of the ionosphere, defined as the total number of free electrons present in a column with a transverse section of $1m^2$ along a path between two points, typically a space-based transmitter and a receiver at ground level. TEC is typically expressed in TEC units (TECu), where 1 $TECu = 10^{16} \frac{e^-}{m^2}$. The variability of TEC, influenced by factors such as solar activity, diurnal cycles, and seasons, introduces a significant error in GNSS positioning accuracy. Consequently, the precise measurement and modelling of TEC are critical for both scientific research in space weather and for improving the performance of high-precision GNSS applications.

It is important here to remember that the ionosphere is a dispersive medium for radio waves. This means that the refractive index of the medium, and thus the signal velocity, is dependent on the signal's frequency.

This property is particularly relevant for GNSS signals, which are high-frequency radio waves passing through the ionosphere on their way from satellites to ground-based receivers. Modern GNSS satellites broadcast signals on multiple frequencies and is therefore possible to compare different phase advance and group delays.

The measurement is typically performed by computing a linear combination of GNSS observables at two different frequencies. A GNSS receiver tracks two types of signals: the pseudorange (or code) measurement and the carrier phase measurement. The pseudorange measurement is a measure of the time of flight, while the carrier phase measurement tracks the number of cycles of the carrier wave. To properly describe the effects on these two parameters, it is necessary to consider the ionospheric nature.

Indeed, to describe the complex refractive index of the ionosphere ($n$), we can consider the Appleton-Hartree equation (Hargreaves, 1992):

$$n^2 = 1 - \frac{X}{1 - iZ - \frac{Y^2 sin^2\vartheta}{2(1 - X - iZ)} \pm \sqrt{\frac{Y^2 sin^2\vartheta}{4(1 - X - iZ)^2} + Y^2 cos^2\vartheta}}. \quad (3.1)$$

The variables $X$, $Y$ and $Z$ are dimensionless ratios defined as $X = \frac{\omega_0^2}{\omega^2}$, $Y = \frac{\omega_H}{\omega}$, and $Z = \frac{\nu_C}{\omega}$. These ratios depend on three characteristic frequencies. $\omega$ represents the angular frequency equals to $2\pi\nu$.

First, $\omega_0$ is the electron plasma frequency, given by $\sqrt{\frac{\mathrm{N_e e^2}}{\epsilon_0 m_e}}$, which is determined by the electron density ($N_e$). Second, $\omega_H$is the electron gyro frequency, calculated as $\frac{B|e^-|}{m_e}$, which depends on the ambient magnetic field ($B$). Third, $\nu_C$is the collision frequency; this term, for the frequency of interest of the GNSS satellites is much smaller than the angular frequency.

Finally, $\vartheta$ is the angle between the ambient magnetic field vector and the wave vector. The terms $\epsilon_0$, $m_e$ and $e^-$ are constants representing the electric permittivity of vacuum, the mass of the electron, and the charge of the electron, respectively.

For the frequencies used for GNSS positioning, it could be possible to consider, as a first order approximation, the Appleton-Hartree approximation considering $X << 1$, $Y \sim 0$ and $Z \sim 0$. This simplifies equation 3.1 as:

$$n = \sqrt{1 - X} \simeq 1 - \frac{X}{2} = 1 - \frac{\mathrm{N_e e^2}}{2\epsilon_0 m_e (2\pi\nu)^2} = 1 - \frac{40.3 N_e}{\nu^2}. \quad (3.2)$$

From the TEC definition we can define the slant TEC (*sTEC*) as:

$$sTEC = \int_{Satellite}^{Receiver} N_e \, dl. \quad (3.3)$$

Therefore, the first order expansion of the optical path Λ of a signal travelling from a GNSS satellite S to a ground receiver R becomes:

$$\Lambda = \int_S^R n \, dl = \int_S^R \left(1 - \frac{40.3 N_e}{\nu^2}\right) dl = D - \frac{40.3}{\nu^2} \int_S^R N_e \, dl = D - \frac{40.3 N_e}{\nu^2} sTEC \quad (3.4)$$

where D is the geometric path between S and R.

We can now define the ionospheric phase advance and code delays (L and $\delta$ respectively):

$$L(cycle) = \frac{\Lambda}{\lambda} = \frac{1}{\lambda}\left(D - \frac{40.3}{\nu^2} sTEC\right) = \frac{\nu D}{c} - \frac{40.3}{c\nu} sTEC \quad (3.5)$$

$$\delta(seconds) = \frac{dL}{dv} = \frac{D}{c} + \frac{40.3}{cv^2} sTEC \tag{3.6}$$

Under the assumed approximation of the Appleton-Hartree formula, it can be therefore obtained that the distance measurements using phase delay and code delay provide with an estimation of actual distance D plus an ionospheric contribution $I$ which, in absolute value, is the same for phase and code, but with opposite sign and is indirectly proportional to frequency.

$$I(v) = \frac{40.3}{cv^2} sTEC \tag{3.7}$$

By comparing the phase and code delays measured by the GNSS receiver at ground level, at two different frequencies, it is theoretically possible to determine both the precise distance between the satellite and the receiver, as well as the signal delays caused by the ionosphere.

It is, indeed, easy to observe that, under those approximations, the difference between the ionospheric effects $I_2 - I_1$ is equal to the difference between the corresponding code delays $\delta_2 - \delta_1$. In this simplified version, the $sTEC$ is therefore equal to:

$$sTEC_{approx} = \left( \frac{v_1^2 v_2^2}{k * (v_1^2 - v_2^2)} \right) * (\delta_2 - \delta_1) \tag{3.8}$$

where $k$ is equal to $\frac{c}{40.3}$.

However, the errors carried by the measured phase and delays are not caused only by the ionosphere, but many other factors influence the effective code delay measured by the receiver. The more precise equations for Code and Carrier phase measurements, provided at a frequency $i$, are:

$$\begin{cases} P_i = D + c \cdot dt + T + I_i + B_{P1} + \epsilon_{P_i} \\ \Phi_i = D + c \cdot dt + T - I_i + \lambda_i \cdot N_i + B_{\Phi_i} + \epsilon_{\Phi_i} \end{cases} \tag{3.9}$$

where:

- $D$ is the true geometric range between the satellite and receiver (~20000 km).
- $c \cdot dt$ is the sum of the receiver and satellite clock offsets multiplied by the speed of light (~500 km).
- $I_i$ is the ionospheric delays measured at frequency $v_i$ (~15 m).
- $T$ is the tropospheric delay (~3 m).
- $\lambda_i \cdot N_i$ is the carrier ambiguity (~2 m).
- B represents the error induced by the hardware for phase and code (~2 m and ~0.05 m, respectively)

- $\epsilon$ represents the noise and the multipath error measurements for the respective observables (~1 m and ~0.01 m, respectively).

The process of deriving a more precise *sTEC* is therefore incomplete. The approximate calculation given by equation 3.8, contains significant systematic errors which must be precisely calibrated to obtain scientifically useful TEC values. They are, indeed, of the same order of magnitude as the ionospheric delay itself and, if not corrected, would render the TEC reconstruction meaningless. The process of removing those non-ionospheric errors is called calibration and can be processed in different ways that all required a lot of mathematical passages. To calibrate for this, these non-ionospheric source of errors must be precisely estimated and subtracted. This is typically done using a multiple GNSS receivers and satellites, where a mathematical model of the ionosphere (like a spherical harmonic expansion) is used to simultaneously solve for the ionospheric parameters and the individual satellite and receiver errors in a least-squares adjustment (Cesaroni, Spogli, & De Franceschi, 2021; Ciraolo et al., 2007).

After the calibration, the comparison of the results from different pairs of satellites/receivers is carried out converting the TEC along the slant path to vertical TEC (vTEC), which represents the total electron content in the vertical column overhead the GNSS receiver. This is done using a mapping function that depends on the satellite's elevation angle. A simple mapping function is the single-layer model, which assumes all electrons are concentrated in a thin layer at a fixed altitude ($h_{ION}$):

$$vTEC = sTEC \sqrt{1 - (\frac{R_E \cdot cos\theta}{R_E + h_{ION}})^2} \tag{3.10}$$

where $R_E$ is the radius of the Earth and $\theta$ is the satellite elevation angle as seen by the receiver (Mannucci et al., 1998).

In this thesis, the calibrated vTEC data, derived from the dense European network of geodetic receivers (Upper panel of figure 4.2), are used to generate vTEC maps. These maps provide a synoptic, large-scale view of the ionospheric plasma distribution over the European sector. They will be used extensively in Chapter 4.2 to provide the large-scale context for the localised LOFAR observations during the May 2024 superstorm.

While the dual-frequency method for the recovery of TEC information is powerful, several challenges and error sources can affect the accuracy of TEC measurements:

- Multipath: Reflected GNSS signals can interfere with the direct signal, corrupting both the pseudorange and carrier phase measurements and leading to errors in the TEC calculation. This can particularly affect the low elevations measurements. Therefore, in my research, I have discharged all the GNSS measurements recorded at an elevation < 20°.
- Carrier Phase Ambiguity: The unknown integer ambiguity in the carrier phase measurements can usually be treated as constant. However, if a cycle slip occurs (e.g. variations of the $\lambda_i \cdot N_i$), the value of the ambiguity changes and the phase-locked loop shifts to a different stability point. This is often the primary challenge in using carrier phase data for absolute TEC determination.
- Receiver and System Noise: Thermal noise in the receiver and other system-related noise sources contribute to the overall measurement error.

In my research, thanks to the abundance of available GNSS data, the observations presenting cycle slips are excluded from the analysis. In particular, the difference between consecutive phase observations is computed. After this the standard deviation of those differences is estimated. A relative threshold is set at 10 times the standard deviation, while an absolute threshold is fixed at 100 TECU. Any phase difference exceeding either of these thresholds is marked as a sudden jump. And, therefore, the observation is discharged. While these thresholds are relatively high compared to standard processing, they were deliberately chosen to prevent the exclusion of genuine, extreme physical variations induced by geomagnetic storms, which can significantly exceed normal ionospheric behavior.

However, this approach does not completely resolve the problem of TEC extraction, as different source of errors can create different patterns on the final measured signal, for this reason it could be difficult to create an algorithm to automatically remove them.

### 3.2.2. ROTI measurement

Raw GNSS phase measurements can be used directly to study dynamic changes in the ionosphere without the need for bias calibration, reducing the computation time need for the analysis.

This is achieved through the "geometry-free" linear combination (GFLC) formed by differencing the carrier phase observations at two frequencies 1 and 2:

$$\begin{aligned} GFLC = \Phi_1 - \Phi_2 = \\ = \left(-I_1 - (-I_2)\right) + (\lambda_1 \cdot N_1 - \lambda_2 \cdot N_2) + B_{\Phi_1} - B_{\Phi_2} + \epsilon_{\Phi_1} - \epsilon_{\Phi_2} = \\ = k \cdot sTEC \cdot \left(\frac{1}{\nu_2^2} - \frac{1}{\nu_1^2}\right) + B_{GF} + \epsilon_{GF} \end{aligned} \tag{3.11}$$

where $B_{GF}$ is a time-constant ambiguity term. This combination effectively removes all geometric terms, leaving only the ionospheric delay term and the constant ambiguity.

The real power of this combination lies in its application to studying ionospheric irregularities. By taking the time derivative of GFLC, we can determine the Rate of TEC (ROT), which measures the change of *sTEC* over a short time interval. ROT, that is defined as $\frac{d(sTEC)}{dt}$ is, in fact, proportional to $\frac{d(GFLC)}{dt}$.

Since the ambiguity term $B_{GF}$ and the instrumental phase biases are constant, they disappear during the differentiation. This means that ROT can be computed directly from raw, uncalibrated GNSS data. From ROT, a key index for quantifying ionospheric turbulence, the Rate of TEC Index (ROTI), is calculated as the standard deviation of ROT over a specified period:

$$ROTI = \sqrt{< (ROT)^2 > - < ROT >^2} \tag{3.12}$$

Traditionally, this technique has been developed for geodetic receivers that, for their primary use, data at a 30-seconds frequency. Therefore, to obtain a sufficiently meaningful statistics, ROTI is usually measured on a 5-minute interval (10 points).

ROTI serves as an excellent proxy for the intensity of medium-scale irregularities, which are responsible for the GNSS phase scintillation (Alfonsi et al., 2021; Carrano et al., 2019; Spogli et al., 2023; Yang & Liu, 2016). Therefore, the $GFLC$ provides a powerful and computationally efficient method to monitor and map ionospheric turbulence globally, completely bypassing the complex and resource-intensive process of TEC calibration described in the following section.

However, there could still be source of errors that are not removed, even using the GFLC. In all my analysis, I have therefore manually verified all the time series containing the ROTI from GNSS and removed the data that presented unphysical patterns, like ROTI constantly been equal to exactly zero.

### 3.2.3. Detrended TEC

The same GNSS raw measurements are also used to reconstruct possible wave-like structures that propagate because of the geospace forcing. Specifically, we make use of the vertical TEC (vTEC) estimates retrieved by applying the vTEC $N_e$ technique, described in (Guerra et al., 2024), to the GFLC data used for the ROTI calculation. This conversion, to a vertical path, allows to create consistent global maps and compare ionospheric conditions over time and location, regardless of the satellite's position. Once the vTEC is derived, a third-order Savitsky-Golay filter (Schafer, 2011) on a 90-minute window is used to remove all the low-frequency components together with a moving average smoothing on a window of 15 minutes to remove all the high-frequency ones. This filtering will highlight the expected signatures of LSTIDs, which are normally defined by periods between 45 and 90 minutes. To investigate the occurrence of TIDs, I exploited, as will be shown in chapter 4, the widely used keograms, a latitude-time plot of δTEC variations to the mean value. The longitudinal sector of interest was between 0° E and 20° E. To reduce the noise, we smoothed the δTEC measurements by averaging over bins of 2.5 minutes in time and 5 km in space. In a keogram, TIDs typically appear as parallel diagonal bands of alternating positive and negative δTEC. The slope of these parallel bands provides insight into the meridional velocity and north-south direction of the TIDs, with steeper slopes indicating faster moving disturbances and shallower slopes corresponding to slower-moving ones. The amplitude of the δTEC variations, as seen in the keogram, reveals the strength of the TIDs, with larger amplitude fluctuations indicating more significant perturbations in the ionosphere's electron content.

## 3.3. Dynamic Spectra

As outlined in Chapter 2, the LOFAR radio telescope comprises a highly distributed array of simple antenna elements. The complexity of this configuration renders the extraction of astronomical parameters from the measured data a non-trivial task. In the following section, the methodology employed to perform this extraction is described in detail.

Let the temporal output amplitude of a LOFAR station $i$ be denoted by $x_i(t)$. This signal, as shown in figure 3.2, is a combination of the receiver response to the sky source signal $s(t)$ and the additive system noise signal $n_i(t)$, related via the formula:

$$x_i(t) = g_i\left[\gamma_i a_i e^{j\phi_i} s(t) + n_i(t)\right] \tag{3.13}$$

with $g_i$ the electronic voltage gain of the telescope receiver system, and $\gamma_i$ representing the relatively slowly varying ionospheric amplitude gain and phase fluctuations. The filter $h_i(f)$ ensures narrow-band operation of the station ($\Delta f < 200\ kHz$), implying that relative geometric delays between stations can be represented as phase shifts. Here $a_i$ and $\phi_i$ represent the station antenna voltage gain and phase related to geometric delay.

The input signals $s(t)$ and $n_i(t)$ are assumed to be independent white Gaussian distributed signals. All signals and parameters in the equation above are assumed to be complex, except $a_i$ and $\phi_i$.

Then, it is possible to obtain the signal power, or intensity, $\mathbf{I_i}(t)$ by the autocorrelation of $x_i(t)$:

$$\mathbf{I_i}(\boldsymbol{t}) = \mathbf{x}(t) \odot \overline{\mathbf{x}(t)} \tag{3.14}$$

From this parameter, is now possible to extract the $S_4$ index, as described in chapter 2.

A schematic diagram of the LOFAR radio telescope signal chain is given in figure 3.1.

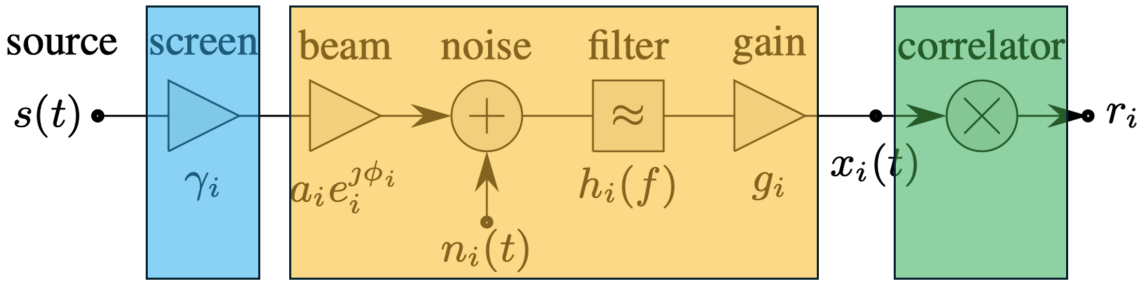



*Figure 3.2. Graphical representation of signal model components for a single station i, measuring the signal s(t) from a radio-source. In blue there is the gain $\gamma_i$ mainly introduced by the ionosphere. The yellow rectangle contains the errors due to the antenna array [beam shape $a_i$, geometric delay (phase) $\phi_i$ , additive system noise $n_i(t)$, narrow-band filter $h_i(f)$, electronic voltage gain $g_i$]. Therefore, the output signal becomes $x_i(t)$, and dynamic auto-correlation spectrum $r_i(t)$.*

Given the different power response, this technique is applied independently to each frequency channel. After this, for a better comparison of the different intensity variations in each frequency channel, a normalisation algorithm is applied on the dynamic spectra recorded by each LOFAR station.

In my research, I have applied a simple running median filter. The window size for the median filter is 30 minutes, which suppresses slow variations in the received signal power, mainly caused by variations of the position of the radio source with respect to the configuration of the main beam of the antennas.

## 3.4. Velocity from Cross-correlation

Given the identical configuration of LOFAR core stations, it is possible to assume the same response to the same ionospheric irregularity. This principle, and the dense distribution of the stations, makes

possible to compare the intensity measured by the stations to extract significant information from the comparison of the measured intensity.

Let $\mathbf{v}_{sc}$ be the ionospheric screen velocity vector in the horizontal plane tangent to the ideal ionospheric thin layer. The time the screen needs to travel from station *j* to *i* is denoted by $\tau_{ij}$ and is given by:

$$v_{sc}\tau_{ij} = \left(\mathbf{p}_i - \mathbf{p}_j\right) \cdot \frac{\mathbf{v}_{sc}}{v_{sc}}, \tag{3.15}$$

where $\mathbf{p}_i$ and $\mathbf{p}_j$ represents the IPP vectors corresponding to station *i* and *j* at the time they cross the same ionospheric irregularity, as shown in figure 3.3.

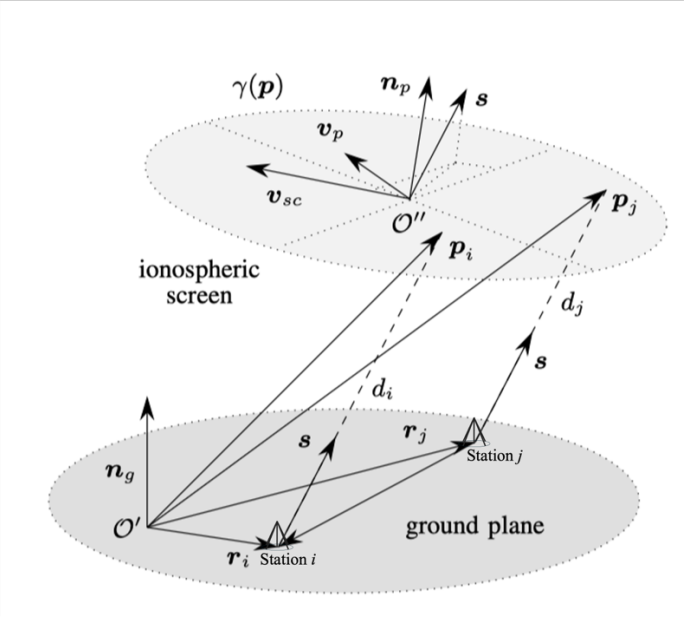



*Figure 3.3. Schematic view of a thin ionospheric screen crossing the IPP of two LOFAR stations i and j.*

These delay times $\tau_{ij}$ can be stacked into a size $(N_{rt}, N_{rt})$ matrix T:

$$T = \begin{pmatrix} \tau_{11} & \cdots & \tau_{1N_{rt}} \\ \vdots & \ddots & \vdots \\ \tau_{N_{rt}1} & \cdots & \tau_{N_{rt}N_{rt}} \end{pmatrix} \tag{3.16}$$

Where $N_{rt}$ represents the number of considered stations. The $T$ elements can be found by finding the lag for which the cross-correlation of the signals measured by the couple of stations is maximum.

Similarly to how the delay matrix *T* is defined, it is possible to create the baselines matrix *B*, of size $(N_{rt}, N_{rt}, 3)$. This matrix contains the distance of each pair of IPPs in the ECEF reference frame.

As reported in (Ghidoni et al., 2025) , the creation of *T* and *B* matrixes is a two-steps process. In the first part, intensity signals from each pair of stations are analysed to find the time lag for which the

cross-correlation is highest. In my research case, I have performed this process considering a Fast Fourier Transform (FFT) convolutions performed on 6-minute windows for the first station and a one-minute windows for the second station and repeating the process on a sliding window of 30 seconds. These parameters follow from a good balance between the accuracy of the results and the computation time. The FFT convolution method results robust against the presence of fast, unphysical data points observed in the signal, which appear as sudden drops or sharp increments over short time intervals and across all frequencies.

Defining the vectorised versions of $B$ and T by $\mathcal{B} = vec(B)$ and $\mathcal{T} = vec(T)$, it is now possible to transform equation 3.15 as:

$$\mathcal{T} = \mathcal{B}\frac{\mathbf{v}_{sc}}{v_{sc}^2}, \tag{3.17}$$

with $B$ and $T$ known (derived from observations), $\mathbf{v}_{sc}$ can be estimated by minimizing:

$$\hat{\mathbf{v}}_{sc} = arg\ min_{v_{sc}}||\mathcal{B}\frac{\mathbf{v}_{sc}}{v_{sc}^2} - \mathcal{T}||_F^2. \tag{3.18}$$

The least square error solution is, therefore, given by:

$$\frac{\mathbf{v}_{sc}}{v_{sc}^2} = \mathcal{B}^{\dagger}\mathcal{T} \tag{3.19}$$

Taking the inner product of the terms in the equation above gives $\frac{1}{v_{sc}^2} = ||\mathcal{B}^{\dagger}\mathcal{T}||^2$, leading to:

$$\hat{\mathbf{v}}_{sc} = \frac{\mathcal{B}^{\dagger}\mathcal{T}}{||\mathcal{B}^{\dagger}\mathcal{T}||^2}. \tag{3.20}$$

In practical observations, outlier results may occur, but these can be suppressed with a $N_{rt}^2$ diagonal weighting function W. The weighted $\hat{v}_{sc}$ estimation approach starts with minimizing:

$$\hat{\mathbf{v}}_{sc} = arg\ min_{v_{sc}}||\mathcal{B}\frac{\mathbf{v}_{sc}}{v_{sc}^2} - \mathcal{T}||_{F,W}^2 = arg\ min_{v_{sc}}(\mathcal{B}\frac{\mathbf{v}_{sc}}{v_{sc}^2} - \mathcal{T})^H W(\mathcal{B}\frac{\mathbf{v}_{sc}}{v_{sc}^2} - \mathcal{T}) \tag{3.21}$$

with W the diagonal matrix containing the weights. As before, the solution is

$$\frac{\mathbf{v}_{sc}}{v_{sc}^2} = (\mathcal{B}^H W\mathcal{B})^{-1}\mathcal{B}^H W\mathcal{T}, \tag{3.22}$$

and therefore, the final equation for the velocity estimation with the cross-correlation method is given by:

$$\hat{\mathbf{v}}_{sc} = \frac{(\mathcal{B}^H W \mathcal{B})^{-1} \mathcal{B}^H W \mathcal{T}}{||(\mathcal{B}^H W \mathcal{B})^{-1} \mathcal{B}^H W \mathcal{T}||^2}. \quad (3.23)$$

### 3.4.1. Spline interpolation

Given the 1-second (low) resolution of the LOFAR data, it was necessary to slightly adapt the algorithm for lag extraction from the cross-correlation algorithm described in section 3.4. Indeed, it is possible to obtain a larger accuracy in lag estimation than just the time bin numbers. In my analysis, this is done using splines fitting on the cross-correlation data measured at the fixed 1-second steps. I used an 11-points interpolation: the correlation lag corresponding to the maximum value, and the five earlier and the five later in time. An example of the spline fit is shown in figure 3.4.

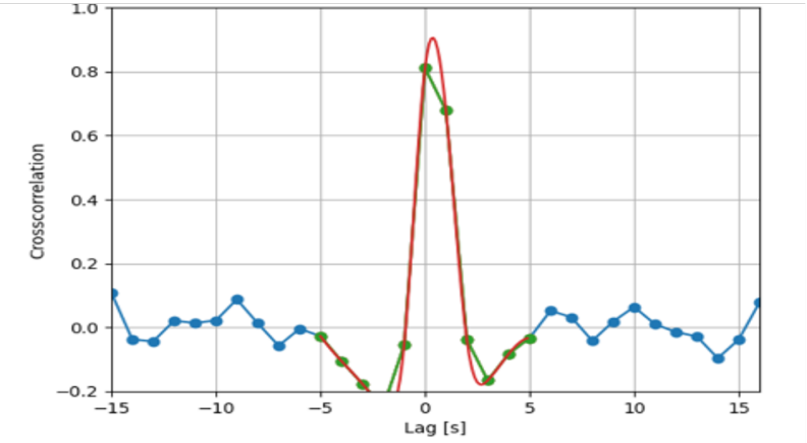



*Figure 3.4 Example of spline fit used to find the best correlation maxima*

To refine the lag estimation, I have applied a cubic spline interpolation on the selected cross-correlation values and determines the corrected maximum using the derivative of the spline. This approach allowed for more precise lag estimations. This is true in particular for small lags, where even a small absolute lag error can result in a large relative error in velocity estimation.

### 3.4.2. Frozen-in approximation

A fundamental assumption underpinning the velocity ionospheric reconstruction algorithms based on cross-correlation is the principle of "frozen-in" flow. This assumption posits that the plasma density irregularities responsible for scintillation are passively carried along, or frozen into, the bulk motion of the background ionospheric plasma (Cesaroni, Spogli, Franceschi, et al., 2021). Consequently, the spatial pattern of these irregularities is assumed to remain rigid and unchanging over short timescale. It is this assumption that allows for the estimation of the ionospheric drift velocity.

As described in detail by (Grzesiak et al., 2022), the frozen-in assumption for the drift estimation states that:

$$C(\zeta, \tau) = C(\zeta - v\tau), \quad (3.24)$$

where $C$ is a correlation function, $\zeta$ is the spatial separation, $\tau$ is the temporal separation (time delay), and $v$ the drift velocity. It means that the temporal dependence of the correlation function might be

seen as a result of change of a reference frame ($\zeta \rightarrow \zeta - v\tau$) and therefore the temporal correlation for a given separation $\zeta 0$ is:

$$C\tau(\tau) = C\zeta(\zeta 0\text{-}v\tau). \quad (3.25)$$

Under this approximation, the time lag that maximizes the cross-correlation between the signals from two different stations can be directly interpreted as the travel time of this rigid pattern across the known projected distance between their ionospheric pierce points. This is what allows the conversion of multiple time delays into a single, coherent velocity vector for the entire "screen" of irregularities.

Having many baselines with significant cross-correlation, it is possible to check the validity of the assumption of frozen drift. According to equation 3.25, cross-correlation in the frozen flow case should be the intersection of the spatial correlation that goes through the separation vector for a given pair in the direction of the velocity vector.

## 3.5. Velocity from Fresnel's Method

An alternative method for estimating the velocity of ionospheric irregularities involves the Fresnel's frequency and the Fresnel's zone.

The absolute value of the relative velocity between the irregularity velocity and the ionospheric pierce point (IPP) velocity can, therefore, be estimated via (Forte & Radicella, 2002; Spogli et al., 2021):

$$v_F = d_F \cdot f_F \quad (3.27)$$

where:

- $v_F$ is the Fresnel's velocity,
- $d_F$ is the Fresnel's zone of the selected frequency,
- $f_F$ is the Fresnel's frequency, calculated as the roll-off frequency of the Fourier transform of the dynamic power spectra every 5 minutes of data.

It is important to remember that this method estimates the relative speed between plasma and the IPP, i.e. the so-called "scan velocity".

In my research, this method is applied to the LOFAR data for which the IPP velocity is significantly lower than the plasma velocity. Additionaly, this calculation yields only the speed, not the velocity vector.

The Fresnel's frequency is determined as the roll-off ($f_R$) frequency of the Power Spectral Density (PSD) based on the Fourier Transform, identified through a fitting procedure at five-minute intervals for each station.

To determine the roll-off frequency, a Fourier transform is applied to a five-minute time series sampled at 60 MHz. Then a piecewise model is fitted to the spectrum to identify the transition point

corresponding to the roll-off frequency. The power spectrum ($P$) is ideally described as a function of frequency $f$:

$$\log(P) = \begin{cases} C, & \log(f) \leq \log(f_R) \\ s \cdot \log(f) + b, & \log(f) > \log(f_R) \end{cases} \quad (3.28)$$

where, $C$ represents the constant power level at low frequencies, while the high-frequency region follows a power-law decay with slope $s$ and intercept $b$. The roll-off frequency is indicated by $f_R$. A least-squares fitting method is applied to optimise the parameters. The roll-off frequency is identified as the point where the two segments of the piecewise fit intersect. Confidence intervals at 95% for the roll-off frequency and the slope are estimated to account for uncertainties in the fit.

To exemplify, figure 3.5 reports an example of this process for data recorded between 23:22:30 and 23:27:30 UT on January 14th, 2022 from the LOFAR CS002 at a frequency of 60 MHz. The red line represents the fitted function. The blue line represents the log-log spectrum. The roll-off frequency is indicated by the dashed blue line while its confidence interval is represented by the light blue box around it. In the grey box, I report the best fit values and their standard deviation for the constant, the slope and the intercept of equation 3.28.

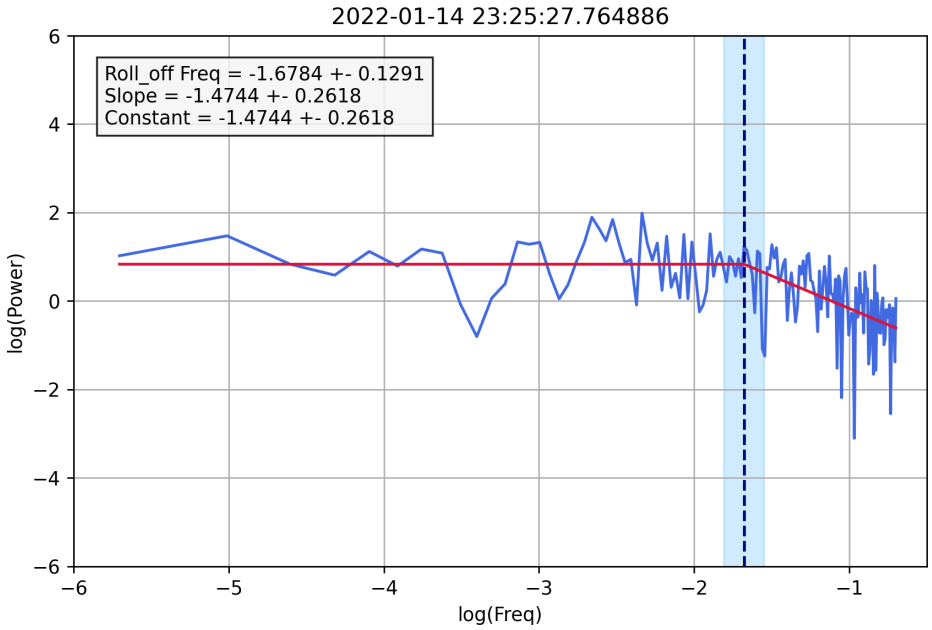



*Figure 3.5. Example of roll-off frequency estimation from the PSD based on FFT of 5 minutes of data between 23:22:30 UT and 23:27:30 UT of January 14th. The blue line represents the log-log spectrum, while the red line shows the fitted function. The roll-off frequency is indicated by the dashed blue line while its standard deviation is represented by the light blue box around it. In the grey box, I report the best fit values and their standard deviation for the constant, the slope and the intercept of equation 3.28.*

Identifying the Fresnel's frequency with the roll-off frequency of the amplitude spectrum introduces some caveats (Song et al., 2025). Within the weak scattering theory, it has been proposed that the amplitude power spectrum bends over when Fresnel-scale structures are present (Yeh & Liu, 1982).

In this case, the roll-off frequency is assumed to approximate the Fresnel's frequency. However, recent findings highlight significant differences between the roll-off and Fresnel's frequencies, suggesting that the phase spectrum method may provide a more accurate determination, particularly in high-latitude scintillation studies. Bearing in mind these limitations, it was, however, possible to retrieve the velocity from Fresnel's frequency estimates and, subsequently, compared it with velocity estimates obtained via the cross-correlation method.

The expression of the Fresnel scale ($d_F$) is:

$$d_F = \frac{\sqrt{2\lambda h}}{(\sin(\theta))^{\frac{3}{2}}} \tag{3.29}$$

in which $h$ is the altitude of the irregularity layer and λ is the wavelength at which the observation is performed. For oblique incidence, the distance between the antenna and the irregularity layer becomes $h/sin(\theta)$, where $\theta$ is the elevation angle of the observation. Additionally, the cross-section is an ellipse, not a circle; this adds another azimuth dependence due to the size of the apparent major axis with respect to the ideal circular irregularity (Teunissen and Montenbruk, 2017).

To accurately model auroral precipitation effects, we also need to move beyond assuming circular irregularities and consider the typical field-aligned sheet-like structures (Wernik et al. 2007). This requires an additional correction of the Fresnel scale based on the angle $\phi$between the magnetic field line ($\vec{B}$) and the Line of Sight ($\overrightarrow{LoS}$) of the observation.

For field-aligned sheets, a structure with a Fresnel scale size, when viewed from a direction parallel to $\vec{B}$ will appear much larger when viewed from a different angle. The correction requires to multiply the Fresnel scale for a factor $\sqrt{\frac{a^2 \cdot (1+tan^2(\phi))}{1+a^2 \cdot tan^2(\phi)}}$.

While we can determine the $\overrightarrow{LoS}$ direction and retrieve $\vec{B}$ from the *International Geomagnetic Reference Field* (IGRF 13) model, we need to assume an elongation ratio ($a$) to correct the Fresnel' scale $d_F$ for $\phi$. The elongation ratio will be assumed as 10, as reported as a reasonable value for the magnetic field–aligned rods by Wernik et al. (2007). A primary limitation of this method is that it estimates only the scan velocity, rather than providing the full velocity vector of the irregularities (see, e.g., Spogli et al., 2021 and references therein). Nevertheless, due to the typically lower LOFAR IPP velocities than plasma ones (for polar sources like Cassiopeia A is of the order of 5-30 m/s, depending on the elevation angle), the resulting error introduced in the analysis is expected to be minimal.

While plasma density irregularities in both the ionosphere (with moderate-to-high relative drift) and the inner heliosphere (with moderate-to-high drift) can produce these Fresnel's frequency values, the variations observed between LOFAR stations suggest that the analysed signals are most likely of ionospheric origin (Forte et al., 2022).

Due to the nature of the algorithm, that is based on the data from a single station the final velocity can be subject to a higher risk of noise-induced errors. To mitigate this, I have opted to independently measure the speed of ionospheric irregularities applying this method to every core station independently. After this I have considered as "true" speed, at each time-step, the median value obtained from the comparison of the different results.

In this paragraph, the Frensel's methodology for velocity reconstruction has been presented specifically applied to the LOFAR intensity data. However, it is important to remember that the same technique can be applied to every time series of intensity measurements. For this reason, this process is widely applied to the data collected by different instruments.

## 3.6. Effective Altitude retrieval

The primary methodological innovation presented in this thesis is a novel algorithm I developed for the retrieval of the effective altitude of the ionospheric irregularity layer. The ionospheric altitude, for the thin layer approximation, is, indeed, traditionally treated as a fixed constant in ionospheric models and representations in geographic coordinates. My technique fundamentally transforms the static thin-screen approximation, which assumes all plasma irregularities are concentrated at a pre-defined height, typically 350 km, into a dynamic, time-resolved measurement. The necessity for such a method arises from the fact that this fixed-altitude assumption can be dramatically incorrect, particularly during severe geomagnetic disturbances where phenomena such as ionospheric uplift can shift the irregularity layer by hundreds or even thousands of kilometres, as demonstrated in the analysis of the Mother's Day May 2024 superstorm described in chapter 4.2.

The algorithm's foundation lies in the strategic combination of the two independent velocity estimation techniques based on cross-correlation, described in chapter 3.4, and Fresnel method, described in chapter 3.5. Those methods exhibit an inverse relationship with respect to the assumed altitude of the ionospheric screen. The first method leverages the dense configuration of the LOFAR Core Stations to track the spatio-temporal evolution of scintillation patterns. The calculated velocity is inversely proportional to the projected baseline distance between the Ionospheric Pierce Points (IPPs) of the station pairs; thus, increasing the assumed screen altitude brings the IPPs closer together, resulting in a lower velocity estimate for a given measured time lag. The second method, based on Fresnel's analysis, utilizes the power spectrum of the signal from a single station. Since the Fresnel's zone size is a direct function of the distance to the screen (i.e., the altitude), an increase in the assumed altitude enlarges the Fresnel zone, leading to a higher calculated velocity.

This opposing dependency creates a unique constraint that could be exploited. For each measurement interval, the altitude is treated as a free parameter and is systematically varied until the velocity magnitudes derived from both the cross-correlation and Fresnel's methods converge to a single, consistent value. The altitude at which this equalization occurs is defined as the "effective altitude." This process yields a powerful, data-driven diagnostic tool, collapsing the complex, three-dimensional vertical structure of the ionosphere into a physically meaningful equivalent layer whose height can be tracked over time.

This novel capability, made possible exclusively by the unique combination of dense spatial sampling and high-fidelity spectral data provided by the LOFAR Core Stations, represents a significant advancement in the ability to probe the dynamic state of the upper atmosphere.

# 4. Results

In this chapter, I will present the main scientific results of my research, derived by applying the mathematical methods described in Chapter 3 to the LOFAR radio telescope and complementary datasets, described in chapter 2. Findings are structured in three distinct parts, moving from detailed analyses of the ionospheric response to specific geomagnetic storms, in sections 4.1 and 4.2, to a broader statistical characterization of ionospheric irregularities in paragraph 4.3.

I begin with an in-depth case study of the geomagnetic storm of January 2022, reporting the results published in (Ghidoni, et al., 2025)a. Through this event, I demonstrate the effectiveness of the cross-correlation technique for characterizing the velocity of sub-auroral ionospheric irregularities. I also provide a direct comparison between LOFAR and GNSS observations, highlighting the fundamental differences in their sensitivity to various irregularity scale sizes.

Following this, I proceed a second major case event: the extreme "Mother's Day" superstorm of May 2024 (Ghidoni, et al., 2025b). I showcase the unique capabilities of LOFAR under the most severe space weather conditions by applying the novel effective altitude retrieval algorithm. Using this method, the dramatic ionospheric uplift event can be quantified, being largely unobservable by conventional ground-based instruments.

Finally, to contextualize these event-based findings, I present the climatological analysis on over two years of LOFAR observations. This statistical study moves beyond individual storms and allows to establish the typical characteristics and dominant behaviours of the ionospheric irregularities that affect LOFAR. Through this, I validated and generalised the conclusions I drew from the specific case studies.

Taken together, such results illustrate LOFAR's significant and unique contributions to the field of ionospheric physics.

## 4.1. January 2022 storm

**The research and analysis detailed in this chapter form the basis of my first-author paper** (Ghidoni, et al., 2025) "**Ionospheric Response to the January 2022 Geomagnetic Storm using LOFAR and GNSS," from which this text is adapted.**

### 4.1.1. The storm conditions

The arrival of an Interplanetary Coronal Mass Ejection (ICME) on January 14th, 2022, caused an increment in the main interplanetary magnetic field (IMF) and solar wind parameters measured at 1 AU (Fig. 4.1, Panels a and b), resulting in a geomagnetic storm (Pedersen et al., 2024; Vanlommel, 2022). The storm development was monitored using data collected by the Deep Space Climate Observatory (DSCOVR) spacecraft (Burt & Smith, 2012), located at the Lagrangian point L1. DSCOVR provides real-time data on solar wind (SW) parameters and the IMF (Loto'aniu et al., 2022). It collects plasma parameters (density, velocity, and temperature) at 1-minute resolution, whereas the IMF measurements are at a 1-second resolution. The disturbance is visible also from the geomagnetic

disturbance indices measured at ground (Fig. 4.1, Panels c, d and e). In fact, the Disturbance Storm Time (Dst, Panel e) reached a minimum of -91 nT on January 14th at around 23:00 UT. Fig. 4.1d shows the three-hourlyindex, in which the colour code indicates the NOAA Space Weather Scale for geomagnetic storms (*https://www.swpc.noaa.gov/noaa-scales-explanation*).

Related to the increment of the Kp index in the night between 14th and 15th, there was an intensification of the Auroral Electrojet in the European Sector. In figure 4.1c are reported the electrojet intensity indexes IU, IL and IE crossing the IMAGE magnetometer network (Kauristie et al., 2017; Viljanen & Häkkinen, 1997). The increment in the electrojet indexes after 20:00 on January 15th is a trace of another geomagnetic storm that occurred concurrently with the main Hunga Tonga eruption (Verhulst et al., 2022), which occurred at around 4:00 UT on the same day. For this study, I focus on ionospheric variations between 16:00 UT on January 14th and 08:30 UT on January 15th, 2022, a period during which LOFAR data were available.

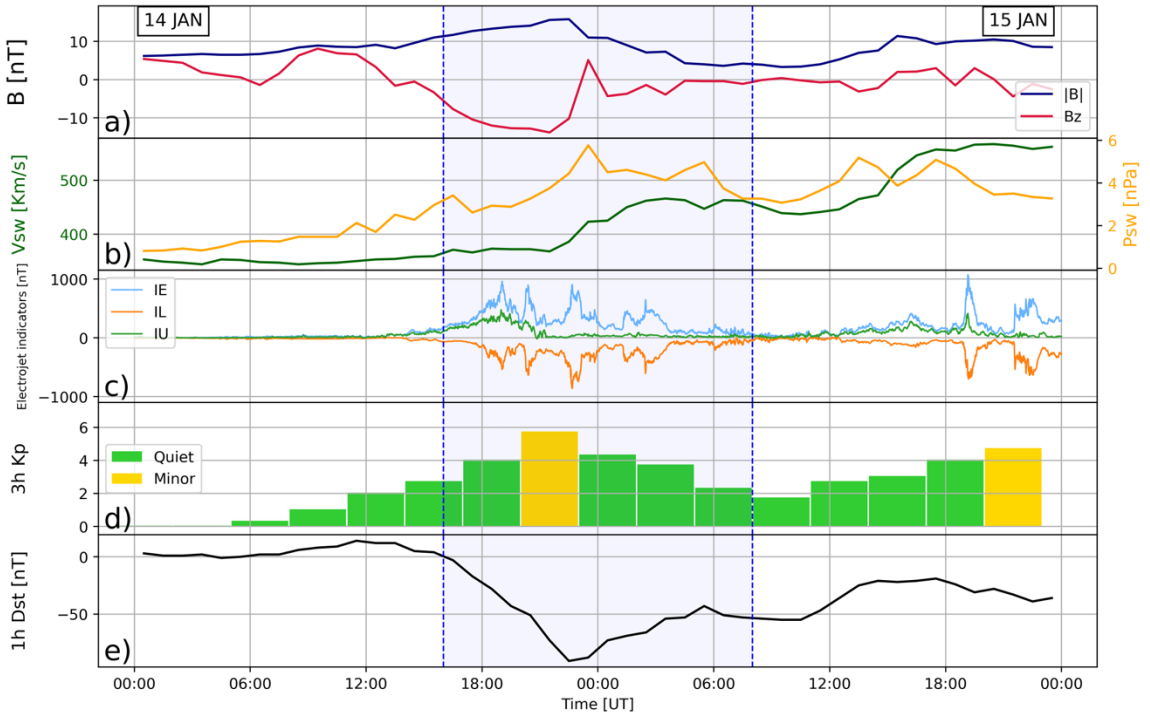



*Figure 4-1Total intensity |B| and Bz component of the IMF (Panel a), Solar Wind speed (Vsw) and pressure (Psw) (Panel b). Data in panel a and in panel b are measured at 1 AU. Other panels report the electrojet indexes IE, IL, IU in the European sector (Panel c), Kp (Panel d) and Dst (Panel e) indices during the storm. The colour code in panel d indicates the NOAA Space Weather Scale for geomagnetic storms. The blue shaded area in all panels represents the period between 16:00 UT of January, 14th and 08:30 UT of January 15th, the focus period of our analysis.*

### 4.1.2. Results and Discussion

Figure 4.2 shows the comparison between the time profiles of 5-minutes resolution ROTI, from the GNSS stations and of 1-minute resolution $S_4$ extracted from the 60 MHz intensity measured by the LOFAR core station CS002 and the international stations. The $S_4$ data are measured considering the median power of all the frequencies in a 2 MHz band around the centre for every temporal interval, to reduce possible noises in single frequencies channels due to non-ionospheric noise. ROTI is evaluated on a 5-minutes basis leveraging 30 s GNSS observables. The dots colour represents the

value of the latitude of the IPP projected at an altitude of at 350 km, which is a reasonable altitude for the ionospheric F-layer, identified as the irregularity layer. Discussion about this assumption is provided later in this section. The GNSS data were dismissed if at an elevation of less than 20°, to minimise the effect of the multipath, which can mimic ionospheric effects. ROTI data only refer to the IPP latitude range between 47.5° and 65°, to match the same range of LOFAR data. It is worth note, however, how the GNSS receivers in Europe cover a larger latitudinal range (Upper panel of figure 2.8), providing useful insights of the irregularities that moves from the Arctic regions toward the equator. In the S4 plot, it is important to note that the brief increment in the S4 value around 18:00 UT of January $14^{th}$ correspond to a few-second increase in a single German station (DE603). Therefore, this increment was not considered to be due to ionospheric effects and a detailed analysis of has not been performed.

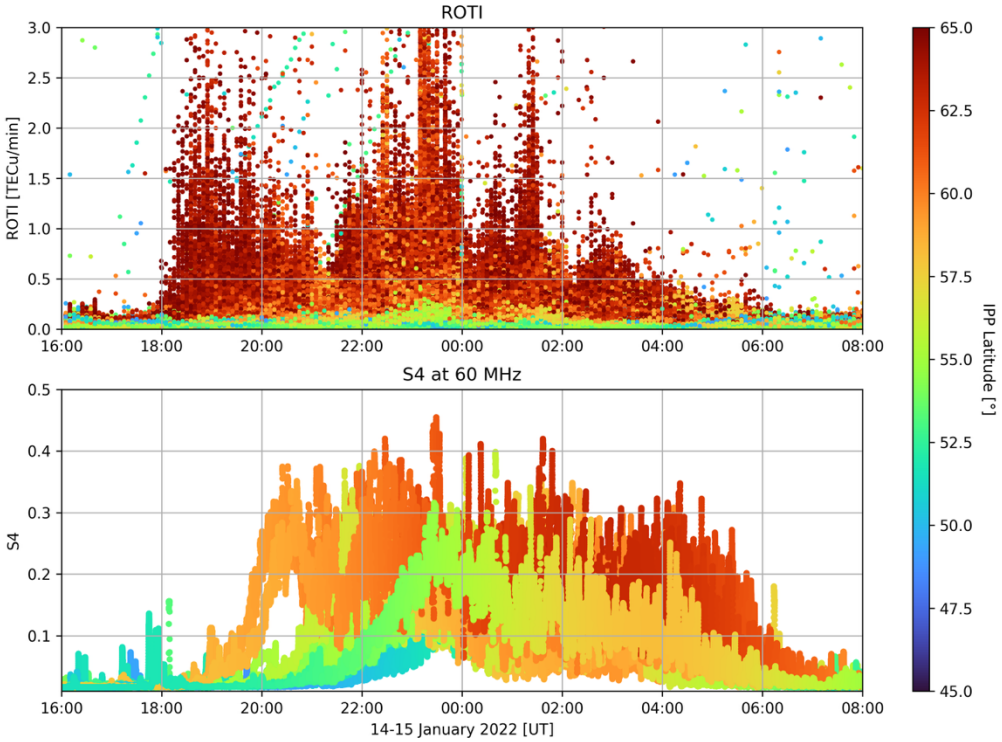



*Figure 4.2. ROTI and S4, measured at 60 MHz, time variability depending on latitude. All the points are projected at an IPP altitude of 350 km. Only data between 45°N and 65°N are shown. This is the same observational range of LOFAR data during the storm.*

After this general investigation of the instruments response to the storm, the analysis moved to a more localised investigation of the ionospheric sectors involved in the formation of irregularities. This was performed by investigating the geographical maps of ROTI and S4 at 5-minute intervals. An animation covering the full storm development is provided in the supplementary material A (*https://drive.google.com/file/d/1QKkwluydEtA_GEX4DXdSnWszPKOZC2qF/view?usp=sharing*). Specifically, the animation shows the period between 16:00 UT of January $14^{th}$, 2022 to 6:00 UT of January $15^{th}$, 2022, with a time step of 5 minutes. Blue dots show LOFAR data from all the international stations and the core station CS002 only. S4 data from other core stations are not reported as they do not differ from CS002, due to their proximity. The blue shade intensity represents the S4 magnitude for the LOFAR selected frequency. If the S4 measured by a station is below the threshold of 0.05, the data is represented with a red cross. On the other hand, the yellow/black points, represents the ROTI value from GNSS above 0.2 TECU/min.

This value was chosen as it effectively accounts for the overall noise level of the observation both prior to 18:00 UT on January 14th and subsequent to 06:00 UT on January 15th, as visible in figure. 4.2. This selection allowed for a better distinction between ROTI increments attributable to the storm and those from other effects. Additionally, according to (Cherniak et al., 2015), the value of 0.2 TECu/min is a reasonable threshold for differentiating between the absence of significant TEC gradients and the presence of the trough walls of the high-latitude ionosphere.

Values below this threshold are indicated with a small grey dot. The red lines represent the edges of the modelled auroral oval, obtained from the closest (in time) imaging data from the DMSP satellite. Both LOFAR and GNSS data are projected at an IPP of 350 km, if outside the auroral oval, or 120 km, if inside of it. This is because, the maximum height of the particle precipitation causing ionospheric irregularities within the oval is expected to be located at around 120 km, while outside, F-layer irregularities are more likely to occur. The validity of the assumption of putting the IPP of LOFAR at 350 km below the auroral oval is confirmed by the Juliusruh ionosonde observations (*https://giro.uml.edu/ionoweb/#*) while the assumption of 120 km as the height within the oval are a reasonable value for the height of the irregularity has been verified by using the ionosonde located in Sodankylä, Northern Finland[1,2]. The title of each map reports the time of the ROTI data. For what concerns LOFAR data, the plot contains the mean S4 value of the data collected by each station in the five minutes before the time shown in the title. The time of the nearest auroral oval position estimation is reported in the title labelled as "Auroral time". For the sake of clarity, figure 4.3 reports the map at 20:05 UT of January $14^{th}$, when irregularities are being observed by both instruments.

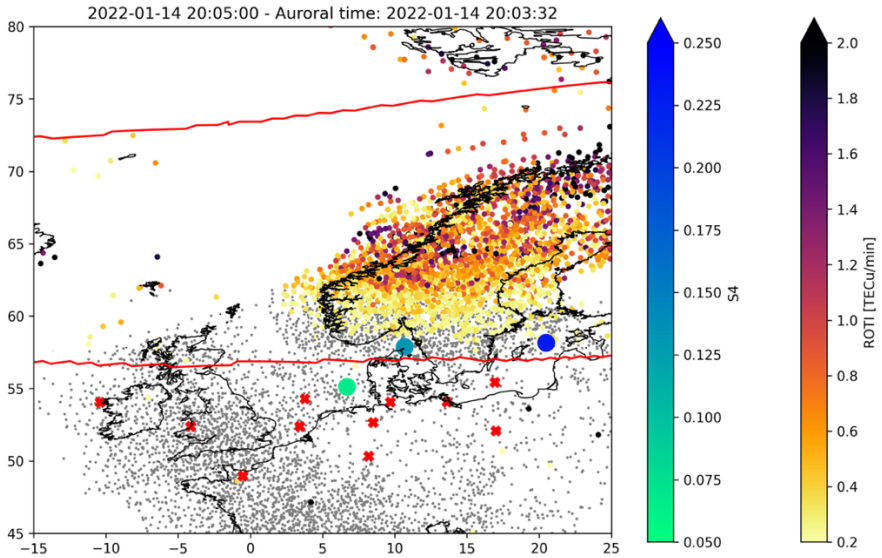



*Figure 4.3. Map of the ionospheric irregularities measured around 20:05 UT of January$14^{th}$ over the European sector at latitudes between 45° and 80° N and longitudes between -15° and 25° E. The red lines represent the boundaries of the auroral oval modelled by the DMSP. The ROTI data are represented in the yellow-black scale if over the threshold of 0.2 TECU/min or as simple grey dots is*

[1] *https://www.sgo.fi/pub_ion/IonoDaysView/IonoView_2022/IonoDay_2022_01_14.pdf*

[2] *https://www.sgo.fi/pub_ion/IonoDaysView/IonoView_2022/IonoDay_2022_01_15.pdf*

*under it. The LOFAR S4 follow logic with a threshold of 0.05 and a scale green/blue and red crosses..*

Figure 4.4 reports the results at 22:00 UT of January $14^{th}$,where the stronger structuring of the irregularities is found. It is interesting to notice how inside the auroral oval it is possible to observe irregularities measured by both GNSS and LOFAR. This was expected, considering the auroral oval is the region of main ionospheric activity during a geomagnetic storm. The same is true near the lower boundary of the auroral oval, where it is possible to observe the effects of the ionospheric through, in agreement with what found by Cherniak and co-author during the 2015 St.Patrick's Day Storm (Cherniak et al., 2015).

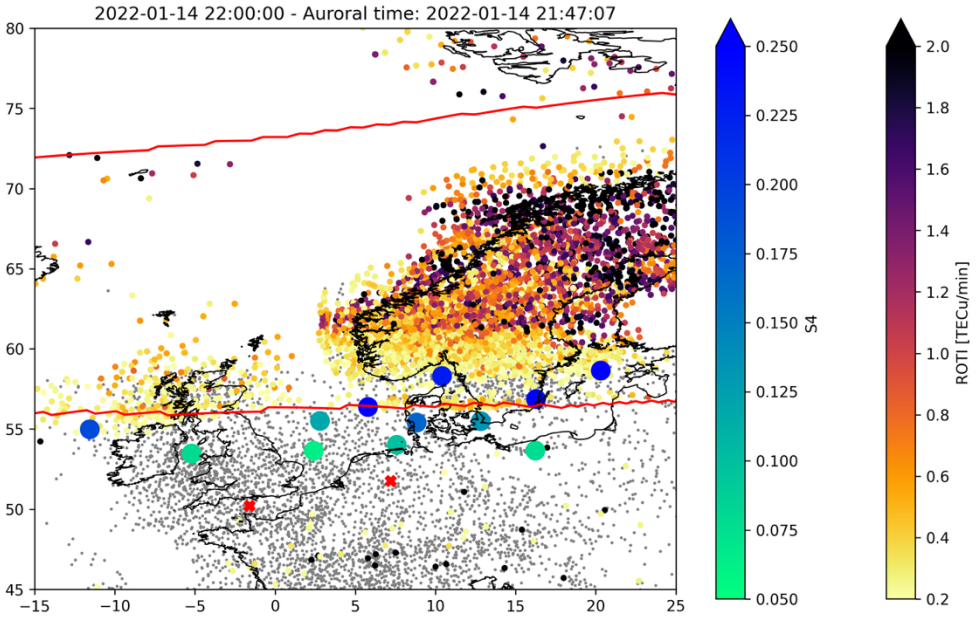



*Figure 4.4. Map of the ionospheric irregularities measured around 22:00 UT of January$14^{th}$ over the European sector at latitudes between 45°N and 80° N and longitudes between -15° and 25° E. The red lines represent the boundaries of the auroral oval modelled by the DMSP. The ROTI data are represented in the yellow-black scale if over the threshold of 0.2 TECU/min or as simple grey dots is under it. The LOFAR S4 follow the same logic with a threshold of 0.05 and a scale green/blue and red crosses.*

The presence of a steep ionospheric through is, for example, proved also in the electron density data collected by ESA Swarm Bravo satellite from 23:07 UT and 23:16 UT of January $14^{th}$. Figure 4.5a shows the map of the ionospheric irregularities measured around 23:10 UT of January $14^{th}$ over the European sector at latitudes between 45° and 80° N and longitudes between -15° and 25° E. The dark green line represents the trajectory of the Swarm Bravo satellite passing over Europe, from South to North, between 23:07 UT and 23:16 UT of January $14^{th}$. The light green line indicates the in-situ plasma density of Swarm Bravo with a higher longitudinal positive deviation from the ground track, the higher the plasma density is.

Figure 4.5b shows the in-situ electron density measured by Swarm Bravo (red line) between 23:07 UT and 23:16 UT of January 14th over the European sector. The blue dots represent the ROTI values measured by the GNSS. The yellow band represents the represents the enhancement of ROTI between

0.2 and 0.5 TECU/min, from which it is possible to see how values in such a range nicely corresponds to the poleward boundary of the ionospheric trough.

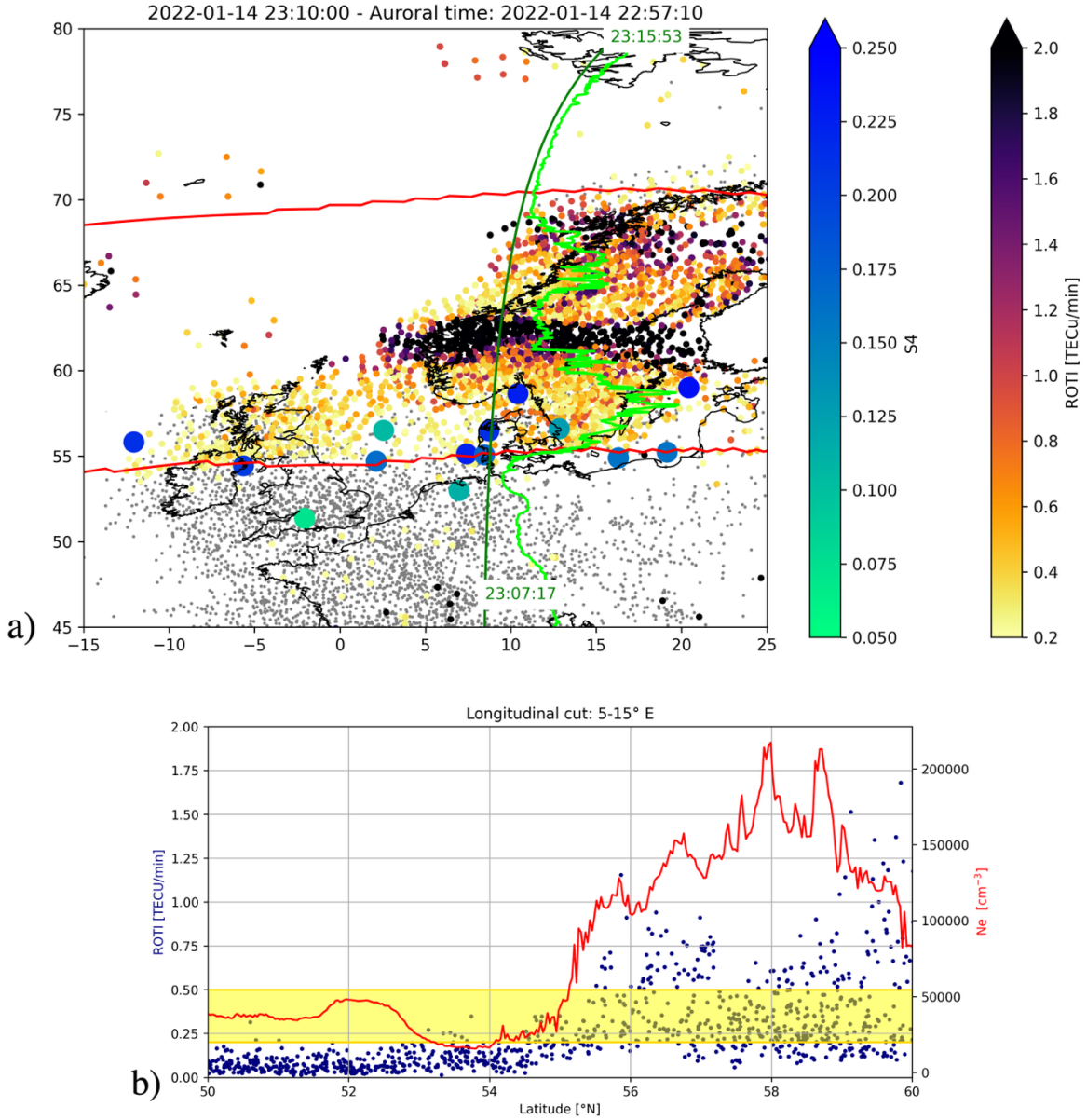



*Figure 4.5. Plot a) shows the map of the ionospheric irregularities measured around 23:10 UT of January14$^{th}$ over the European sector at latitudes between 45° and 80° N and longitudes between -15° and 25° E. The red lines represent the boundaries of the auroral oval modelled by the DMSP. The ROTI data are represented in the yellow-black scale if over the threshold of 0.2 TECU/min or as simple grey dots is under it. The LOFAR S4 follow logic with a threshold of 0.05 and a scale green/blue and red crosses. The dark green line represents the trajectory of the Swarm Bravo satellite passing over Europe, from South to North, between 23:07 UT and 23:16 UT of January 14$^{th}$. The light green line indicates the in-situ plasma density of Swarm Bravo with a higher longitudinal positive deviation from the ground track, the higher the plasma density is. Plot b) shows the in-situ electron density measured by Swarm Bravo (red line) between 23:07 UT and 23:16 UT of January 14th over the European sector. The blue dots represent the ROTI values measured by*

*the GNSS. The yellow band represents the represents the enhancement of ROTI between 0.2 and 0.5 TECU/min due to the presence of the poleward boundary of the ionospheric trough.*

However, the most intriguing region in figure 4.4 is the one below the auroral oval, where irregularities are measured by LOFAR, but not by GNSS. This is probably due to the scales of the irregularities that are active for LOFAR S4 and not effective in increasing the GNSS ROTI values.

To investigate the ROTI/S4 mismatching at sub-auroral latitudes, I analyse the normalised power data from the LOFAR core stations. An example of this analysis is reported, in the period between 21:20:00 UT to 21:24:59 UT of January 14 $^{th}$ , is reported in the supplementary material B (*https://drive.google.com/file/d/1DlhCtEXTjutlAGK2Qu_DmB_afW0gNwo3/view?usp=sharing*). During this period, ionospheric structuring increases, due to the response to the storm. In the animation in supplementary material B, IPPs of all the core stations are reported, considering an altitude of 350 km. The colour of the dots represents the normalised power measured by each LOFAR station at 60 MHz. During this period, it can be observed a wave-like perturbation crossing all IPPs. Specifically, figure 4.6 shows four consecutive instants of the animation, i.e., from 21:23:02 UT to 21:23:05 UT on January 14$^{th}$. The grey arrow indicates the direction of the velocity of the perturbation using the cross-correlation method. The velocity is measured every 30 seconds so, for every frame, the nearest available velocity is reported, and the corresponding time is visible in the plot title. The IPPs of the entire LOFAR observations (blue line) is shown in the upper left corner, with the position at the considered time indicated by a red dot. In the upper right corner of each plot the amplitude and direction numerical values of this measured velocity are reported.

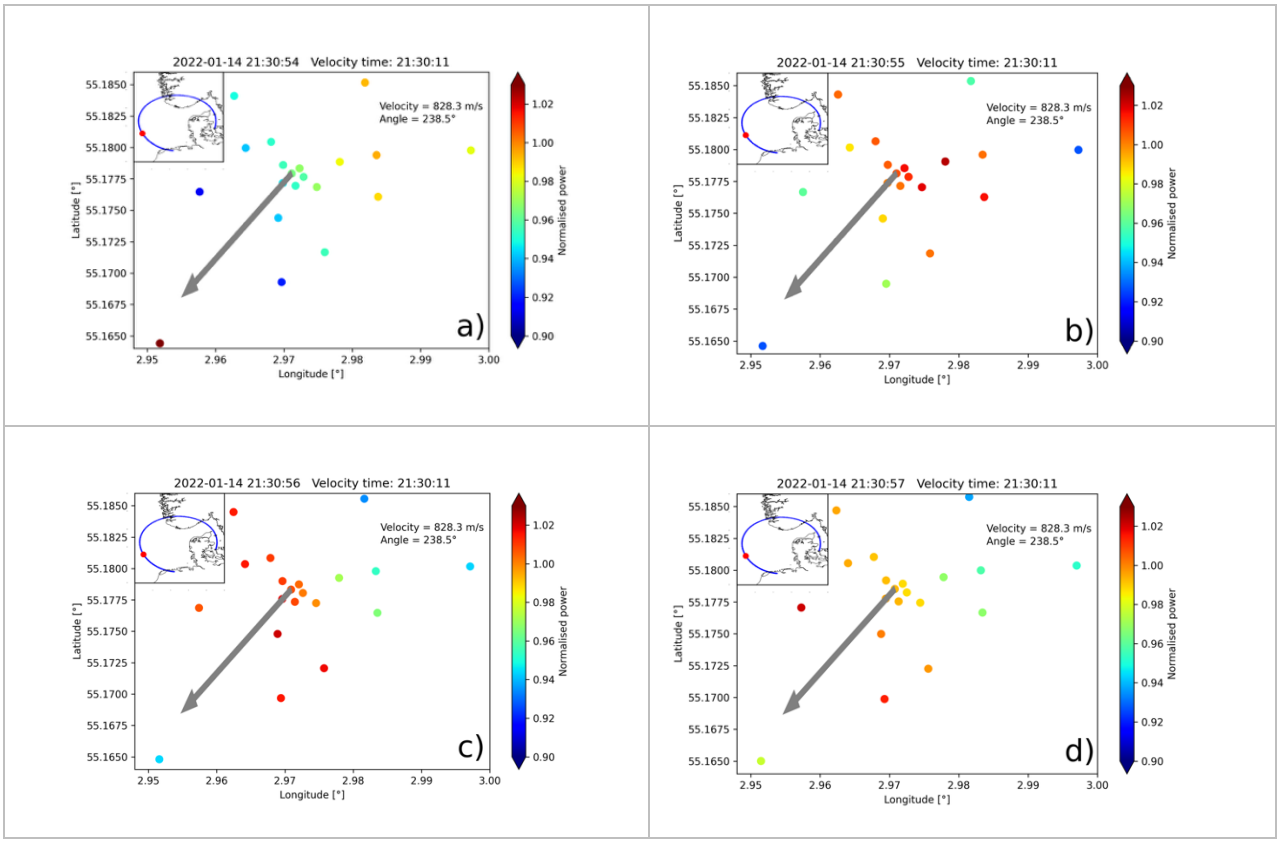



*Figure 4.6. Normalised power measured by the LOFAR core stations projected at an IPP of 350 km for four consecutive instants, i.e., 21:23:02 UT to 21:23:05 UT of January 14$^{th}$. The grey arrow reports the direction of the velocity of the perturbation. I report the nearest velocity available, for*

*which the time is in the plot title. The trajectory of the LOFAR observations (blue line) is shown in the upper left corner, with the position at the specified time indicated by a red dot.*

To measure the velocity of the irregularities seen by the LOFAR core stations it is possible to also use the Fresnel's method (Equation 3.27).

Figure 4.7 shows the velocities obtained by the two methods applied to the data at 60 MHz. The blue line represents the mean velocity of all the core stations obtained using the Fresnel's algorithm while the black line represents the velocity obtained by the cross-correlation algorithm (Equation 3.23). The colour of the dots represents the mean cross-correlation coming from every baseline of the LOFAR core stations at an interval of 30 seconds.

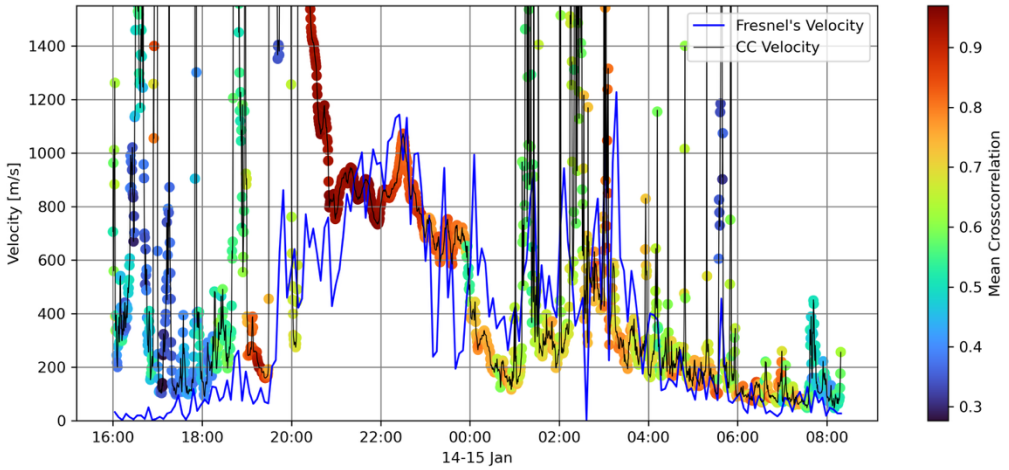



*Figure 4.7. Velocity estimates during the storm by using cross-correlation and velocity from Fresnel's Frequency identification. The blue line represents the mean velocity of all the core stations obtained using the Fresnel's algorithm (Equation 3.27) while the black line represents the velocity obtained by the cross-correlation algorithm (Equation 3.23). Both algorithms refer to LOFAR intensity data at 60 MHz.*

The similarity between those two algorithms, in the most part of the entire observation, supports the robustness of the obtained results. The main discrepancies between the two methods occur at the beginning of the observation (between 16:00 UT and 18:00 UT of January $14^{th}$), in regions where the cross-correlation is low, which in turn reduces the capability of the method to provide reliable values of the velocity. In such cases, the cross-correlation method is less accurate, and the velocity estimation becomes less certain. Additionally, within the same time window, the S4 values are also low, which further limits velocity estimates from the power spectra density due to the absence of Fresnel's filtering mechanism acting on the recorded signals. Another time window, characterised by significant differences in the retrieved velocity with the two methods, is between 20:00 UT and 21:00 UT of January $14^{th}$. One possible reason is that this period corresponds to the highest velocity values ($\geq$ 800 m/s), leading to a greater likelihood of errors associated with the previously described spline-based method for lag estimation in the cross-correlation algorithm. However, the method appears to properly reconstruct the lag, as evidenced by the very high cross-correlation values, shown in red (indicating cross-correlation close to 1) in figure 4.7. However, it is important to consider that the Fresnel's method, using 1-second resolution data, is limited to a finite range of possible roll-off frequency. The greater one is $e^{-0.5}$ Hz. This, combined with the Fresnel's scale of around 2 km,

between 20:00 and 21:00 UT (Figure 4.8) results in a maximum velocity reconstruction from LOFAR data of around 1200 m/s. On the other hand, the cross-correlation algorithm is not limited by this threshold, therefore, I have decided, for the data between 20:00 UT and 21:00 UT of January $14^{th}$, to consider the velocities obtained from the cross-correlation algorithm as more reliable that the velocities obtained from the Fresnel's algorithm.

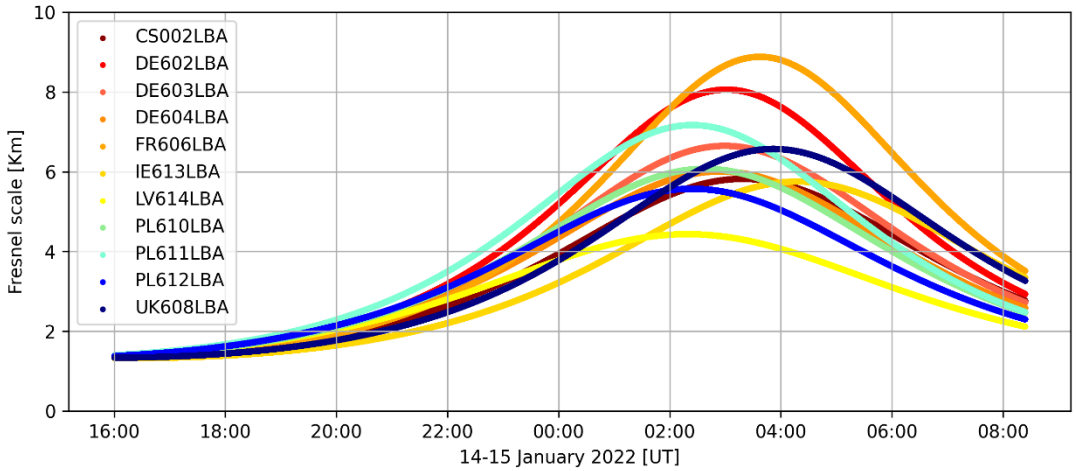



*Figure 4.8. LOFAR Fresnel's scales at a frequency of 60 MHz considering the altitude of a single ionospheric layer at 350 km.*

Additionally, velocity estimates derived from the cross-correlation algorithm allow us to compute both the North-South and East-West components of the velocity, providing essential directional information for understanding the ionospheric flow. In contrast, velocity retrieval based on Fresnel's frequency only measures the magnitude of the relative velocity between ionospheric plasma and IPPs.

The cross-correlation method enables the determination of both the absolute velocity and its North-South and East-West components, offering valuable insights into directional movement, which is critical for understanding the dynamics of the ionospheric irregularities.

Figure 4.9 shows the magnitude and the East-West (E-W) and North-South (N-S) components of the velocity measured by the LOFAR core stations. The colour code follows from the mean cross-correlation evaluated from all the baselines every 30 s. The cross-correlation provides a measure of the reliability of the velocity estimates: the larger the cross-correlation, the more reliable is the measurement. To this scope, it was considered the mean cross-correlation of all baselines, evaluated every 30 seconds. A negative sign in the velocity components indicates a wave propagating from East to West and from North to South. The speed is of the order of some hundreds of m/s, with slightly higher values for the E-W direction. However, before about 20:00 UT and after about 01:30 UT, the reconstruction of the velocity is not reliable presenting speed jumps and low cross-correlation values. Between 00:00 UT and 01:30 UT, there are no meaningful speed jumps; however, the cross-correlation is lower (ranging from about 0.5 to 0.7) compared to the period between 20:00 UT and 00:00 UT.

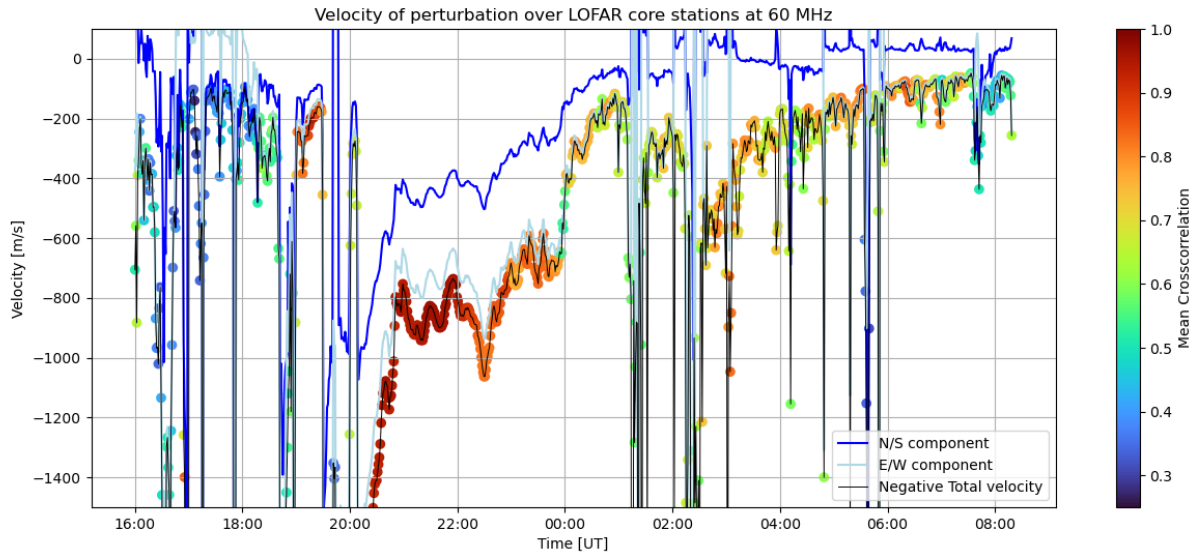



*Figure 4.9. Components (blue for North-South, light blue for East-West) and magnitude (black) of the velocity measured by the LOFAR core stations. The negative sign represents a wave propagating from East to West and from North to South. The colour code represented on the mean cross-correlation coming from all the baselines every 30 seconds. The algorithm is applied to LOFAR intensity data at 60 MHz*

Another notable feature shown in figure 4.9 is that the two velocity components, when the cross-correlation is high, tend to exhibit very similar behaviour, regardless of their numerical values. To investigate this behaviour, the analysis of the azimuthal angle of the velocity was performed, as reported in figure 4.10. In the figure, the black line represents the azimuth of the velocity as a function of time between 16:00 UT on January $14^{th}$ and 08:00 UT on January $15^{th}$. Similarly to figure 4.7, the colour represents the mean cross-correlation. A regular trend appears particularly during the period with high cross-correlation. The magenta lines represent the azimuthal angle of the vector obtained by the cross product of the Earth magnetic field line $B$ and the $LoS$ projected along the plane tangent to the Earth's spheroid at 350 km. For sake of brevity, in the reminder of the text, I will refer to the vector $B \times LoS$ project along the plane tangent to the Earth's spheroid at 350 km simply as $B \times LoS_{tg}$.

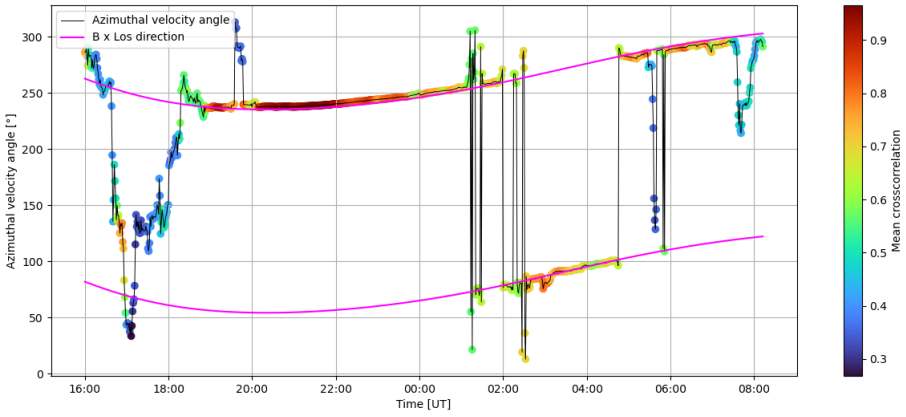



*Figure 4.10. Direction of the ionospheric velocity measured using the LOFAR power data in terms of the azimuthal angle of the velocity. The colour represents the mean cross-correlation of all the baselines every 30 seconds while the magenta lines represent the possible azimuthal angle of $B \times LoS_{tg}$ vector. The algorithm was applied to LOFAR intensity data at 60 MHz.*

A scheme of the geometrical construction used to measure the evolution of the $B \times LoS_{tg}$ is reported in figure 4.11:

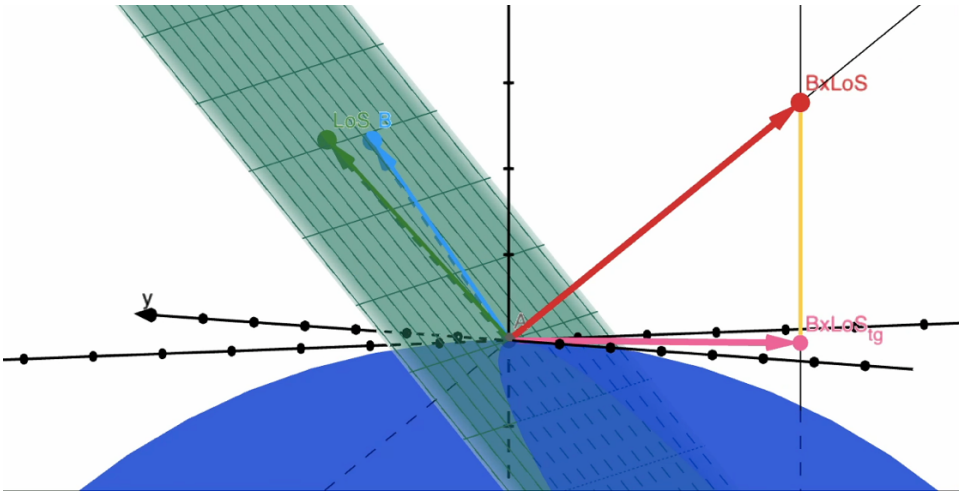



*Figure 4.11. Example of the direction of the velocity reconstructed by the cross-correlation algorithm applied to the intensity data of the LOFAR core stations. The green vector represents the direction of the LoS, while the blue vector represents the direction of the magnetic field line at the IPP of the LOFAR observation. The red vector is given by the cross product of B and LoS and is therefore perpendicular to the green plane generated by the green and the blue vector. Then the velocity is projected on the plane tangent to the idealised ionospheric thin layer, obtaining the magenta vector* $B \times LoS_{tg}$.

This phenomenon can be explained by considering the nature of LOFAR observations and the adopted methods. First, it is important to note that the LOFAR antennas simultaneously observe Cassiopeia A. Given the proximity of the core stations relative to the distance from Cassiopeia A, the *LoS* vectors connecting the antennas to the star can be assumed to be parallel, i.e. the geometrical optics approximation can be assumed. Along these lines, the signal originating from Cassiopeia A and directed towards the LOFAR core stations undergoes variations caused by the ionosphere. However, because of the observational geometry, determining the exact location of these variations is not possible. This is because LOFAR is sensitive only to the integral of the effects along the *LoS* and it is possible to estimate velocities by assuming an irregularity layer like a thin layer, located at 350 km.

Moreover, the role of the Earth's magnetic field lines, along whose lines the ionospheric irregularities tend to elongate, must be considered. The direction of *B* was extracted by the International IGRF-13th Generation, as reported in chapter 2.2.6.

Hence, it was evaluated the cross-correlation between every couple of core stations, considering no time delay ($dt = 0$) between signals, as function of IPP distances.

Figure 4.12 shows an example of cross-correlation of all baselines by considering no delay (dt = 0) among received signals at 21:02 UT of January $14^{th}$. The cyan line represents the component tangent to the Earth's spheroid at 350 km of the magnetic field line at the IPP projected on the plane perpendicular to LoS. It is noteworthy that the points with maximum cross-correlation align almost perfectly with the cyan line. The magenta lines reported in figure 4.10 corresponds to the direction perpendicular to such a cyan line. The good match with the azimuth of the velocity, when the mean cross-correlation is high, means that the measured velocity refers to the projection of those structures, elongated the magnetic field lines, on the plane perpendicular to *LoS.* In other words, LOFAR core

stations measure a component of the velocity projected on a direction that varies with the observational geometry and then, with time.

This provides evidence that the ionospheric structures seen by LOFAR, the measured velocity, are elongated along the aforementioned magnetic field line projection, whose orientation changes with the observational geometry. This comes with a price: no information can be obtained by LOFAR about the velocity component along these projections. Therefore, using the cross-correlation method to retrieve the irregularity velocity, the only perturbations that LOFAR core stations can jointly distinguish are those perpendicular to both *B* and *LoS*.

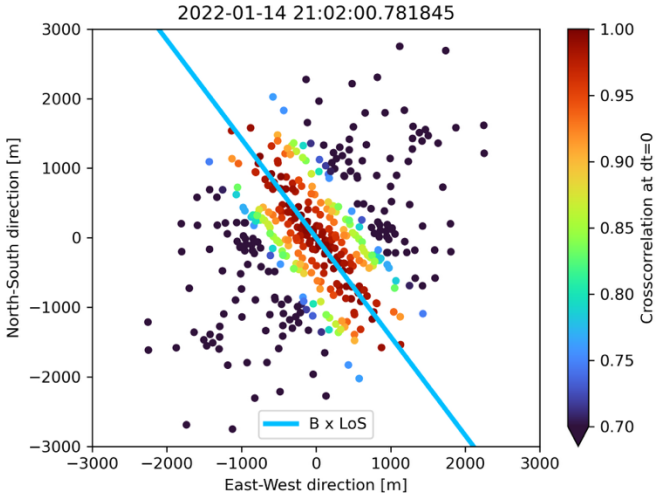



*Figure 4.12. Cross-correlation of all baselines at $dt = 0$. The cyan line represents the component tangent to the Earth's spheroid at 350 km of the magnetic field line at the IPP projected onto the plane perpendicular to LoS. The cross-correlations refer to LOFAR intensity data at 60 MHz.*

Another feature to investigate in figure 4.10 is the presence of a stable flip in the azimuth of the velocity, observed around 02:00 UT of January $14^{th}$ and 06:00 UT on January $15^{th}$. These correspond to small absolute values of the E-W and N-S components of the measured velocity. Therefore, those flips probably happens when the ionospheric velocity is fairly aligned with the magnetic fields line and, consequently, the algorithm struggles to reconstruct the projection of the velocity on the times *LoS* direction.

Bearing this consideration in mind and although the technique to retrieve the velocity suffers some limitations, it still provides useful information about the dynamics of the identified ionospheric structures. For instance, it is possible to use this velocity estimate to verify the hypothesis that the S4/ROTI mismatch in the sub-auroral region is due to the different scales of the measurable irregularities.

During the period of main activity of the storm, around 22:00 UT of January $14^{th}$, the velocity of the perturbation was of about $\sqrt{(400\,\frac{m}{s})^2 + (700\,\frac{m}{s})^2} \sim 800\,\frac{m}{s}$. From this and from the Nyquist frequency of the ROTI observation ($2 \cdot 30$ s), it is possible to obtain a rough estimate of the minimum dimension of the measurable irregularity from GNSS observation, under the approximation of the perpendicular velocity beten the ray path and irregularity velocities. This is equal to 800 m/s · 60s = 48 km, meaning that for GNSS data at 30 s temporal resolution it is impossible to measure

irregularities caused by irregularities below about 10 km, as seen by LOFAR. For LOFAR, the minimum dimension of the perturbation is given by its Fresnel's scale. The difference of measurable scale between LOFAR and GNSS is likely the main cause of the different perturbations seen by LOFAR and GNSS in the sub-auroral region in figure 4.4.

However, the nature of these wave-like irregularities needs further investigation. Bearing in mind the limitation of the velocity retrieval, it is still possible to obtain that: (i) they are irregularities with a typical scale size below 10 km; (ii) they have a speed ranging between from about 1500 m/s and 100 m/s; (iii) they have a E-W component whose speed is larger than the N-S component.

To further investigate such a nature, the velocity reconstructed by LOFAR is compared with the one retrieved by means of GNSS data. Specifically, I considered the detrended TEC (dTEC) measurements from GNSS and the related keogram, as explained in chapter 3.2.3. The keogram in figure 4.13 shows the dTEC variations in a time window between 15:30 UT and 09:00 UT of the night of between January $14^{th}$ and $15^{th}$, and a latitudinal range between 35°N and 65°N. The data were processed using a 15-minute bandpass filter, as described in chapter 3.2. The alternating positive and negative variations in the dTEC values, represented by diagonal red and blue stripes, are a clear signature of Large-Scale TIDs (LSTIDs) propagating in the N-S direction. The yellow line represents the average position of the equatorward boundary of the auroral oval in the European sector, as retrieved by the DMSP-based model. The black line represents the latitudinal IPP position of the LOFAR LBA core station CS002 at an altitude of 350 km and the grey area below that line is the corresponding N-S component of the velocity measured every 30 seconds. The green line highlights a LSTID propagating N-S at around 630 m/s and intersecting the IPPs of the core stations right after 20:00 UT. Numerous other LSTID signatures are evident in the keogram; however, this particular signature clearly crosses the LOFAR field of view, making a direct comparison with LOFAR data and associated velocity possible. When the TID crosses the LOFAR position the algorithm measure a velocity in the North-South direction of around 930 m/s. Then, the speeds of the irregularities reconstructed with LOFAR and with GNSS, despite numerically different, present the same order of magnitude.

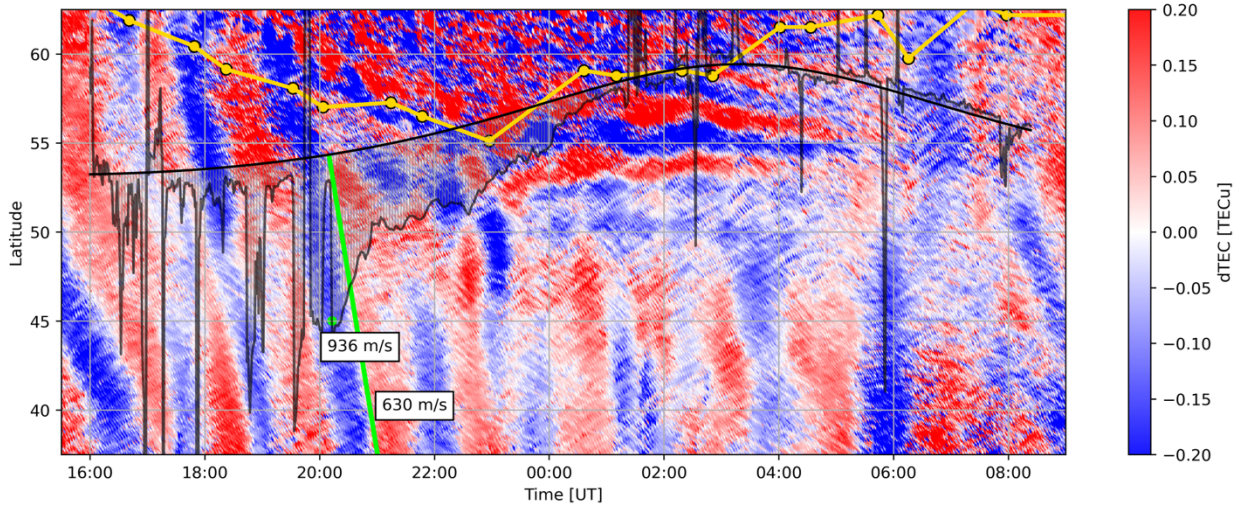



*Figure 4.13. Keogram reporting the latitudinal distribution of the dTEC from 35° to 65° N for the time interval 15:30 to 09:00 between January $14^{th}$ and $15^{th}$, 2022. The yellow line represents the position of the lower boundary of the auroral oval. The black line represents the latitude of the LOFAR observation projected at an IPP of 350 km. The grey segments represent the Latitudinal*

*component of the velocity measure at the corresponding time, one degree corresponds to 100 m/s. The green segment highlights the alternations of positive and negative dTEC, showing the presence of a TID. The green dot represents the velocity measured by LOFAR at the same time and latitude of the TID seen by GNSS.*

The most reliable reconstruction of the velocity using LOFAR is obtained between 22:00 UT and 00:00 UT. During this period, the IPPs of the core stations were close to the boundary of the oval. As a result, it was possible to obtain a trustworthy velocity only within a narrow band of few degrees equatorward to the to the auroral oval. When the IPPs are at lower latitudes or inside the auroral oval, the cross-correlation weakens, indicating a loss of coherence in the structures.

A possible explanation about the nature of the small-scale (<10 km) wave-like disturbances is that they are related to the triggering process of LSTIDs. In fact, the reconstruction of the coherent wavelike structure is possible only in 'far field' relatively to the auroral precipitation, likely capturing TID-related disturbances in which LSTID are forming. In the 'near-field' region, i.e., when IPPs are crossing the selector in which particle precipitation occurs, the irregularities are neither large nor persistent enough to coherently traverse all baselines. This is also true when the IPPs fall below the previously mentioned narrow latitudinal band below the oval, i.e. before 20:00 UT. Despite this, that period is marked by IPPs crossing LSTID signatures in the keogram, particularly around 18:30 UT to 19:00 UT. Then, in this case, no apparent relationship seems to exist between the LOFAR-detected wavelike irregularities and the LSTIDs.

Since the LOFAR irregularities have an E-W component whose speed is larger than the N-S component, it was not possible to be completely sure that disturbances observed in LOFAR may have triggered the occurrence of TIDs seen by GNSS, which are conversely featured by larger values on the N-S component.

Another option deals with the association of these wavelike structures to a series of phenomena occurring in the ionospheric sub-auroral region. This is region is highly dynamic, especially during storm and substorm activity. In our case, the larger values of cross-correlation occur in correspondence with the larger activity of the westward currents, as demonstrated by the IL behaviour, especially between 20:00 and 22:00 UT. This marks the possible intensification of enhanced westward flows (< 1 km/s), such as polarisation jets, sub-auroral ion drifts (SAIDs), and sub-auroral polarisation streams (SAPS) (Horvath & Lovell, 2021). The very large speed featuring these classes of sub-auroral phenomena matches with the velocity of the irregularities reconstructed by LOFAR and with fact that these structures, whenever coherent, are confined in a narrow latitudinal band of few degrees, in agreement with the literature. In other words, this would justify why, right after 20:00 UT, the obtained velocity is $\sim 1500\,\frac{m}{s}$ with such a good mean cross-correlation right below the auroral oval.

### 4.1.3. Final remarks

In this study, I successfully leverage the combined capabilities of LOFAR and GNSS to investigate ionospheric irregularities during the geomagnetic storm of January 14th -15th, 2022. While the LOFAR and GNSS observations reveal distinct aspects of the ionospheric response to the geomagnetic storm, the specific nature of a direct causal link between small-scale irregularities detected by LOFAR and large-scale TIDs remains an open question that warrants further investigation. By integrating data from these two systems however, it was possible to provide a comprehensive analysis of ionospheric disturbances, focusing particularly on the sub-auroral sector. The analysis identified three distinct phenomena associated with the geomagnetic storm: the

enhancement of direct particle precipitation within the auroral oval, the steepening of the equatorward edge of the high-latitude ionospheric trough and the propagation of wave-like structures in the sub-auroral latitudes, characterised by scales of a few kilometres and velocities of several hundred metres per second.

Thanks to the higher resolution of LOFAR data, it was possible to apply set up two methods to reconstruct the velocity of these wavelike structures. Those methods provided evidence that with LOFAR core stations it is possible to measure the component of the component of the velocity perpendicular to both *B* and *LoS* and then projected on the plane tangent to the Earth's spheroid at an altitude of 350 km. From the same algorithm, it was also possible to obtain a measure of the goodness of the algorithm itself. These observations contribute to a deeper understanding of the dynamic processes occurring in the ionosphere during this geomagnetic storm.

## 4.2. May 2024 Mother's Day Superstorm

**The research and analysis detailed in this chapter form the basis of my first-author paper (Ghidoni et al., 2026), "LOFAR uniqueness under extreme ionospheric conditions: The May 2024 Mother's Day Superstorm," from which this text is adapted.**

### 4.2.1. Note on the naming convention

In this thesis, the extreme geomagnetic event of May 2024 is referred to as the "Mother's Day Superstorm," a designation widely adopted across Europe, Asia, and Africa due to the storm's coincidence with Mother's Day in many nations. However, it is important to acknowledge the current lack of a standardised international nomenclature for space weather events, which has led to varying designations for the same phenomenon. For instance, in the United States, the event has been referred to as the "Gannon Storm" in honor of a recently deceased scientist, while in China it is known as the "Han Anniversary Storm", and some Russian scientists have used "Victory Day Storm". Furthermore, the classification of the event as a "superstorm" versus a "storm" remains a subject of scientific discussion, often depending on the specific geomagnetic indices and thresholds applied. The term "Mother's Day Superstorm" is used here to align with the nomenclature proposed by the European Space Weather and Space Climate Association (E-SWAN) and to reflect the widespread public and scientific usage within the European sector (Chabanski et al., 2025). This usage underscores the broader need for a unified, scientifically grounded naming framework to enhance clarity and public communication regarding space weather risks.

### 4.2.2. Introduction

The May 2024 Mother's Day Superstorm, the strongest since November 2003, triggered significant ionospheric disturbances (Jin et al., 2025; Spogli et al., 2024; Themens et al., 2024). Indeed, during the superstorm, the ionosphere above Europe was transformed into a severely depleted, super-high-altitude plasma structure extending beyond 1500 km above Earth's surface.

In this chapter I will highlight the unique contributions of the LOw Frequency ARray (LOFAR) to ionospheric weather research on this extreme event. I will demonstrate how, leveraging LOFAR measurements, it was possible characterise a plethora of ionospheric effects that occurred during the main and early recovery phases of the storm. This was made possible by observing significant signal fading associated with the equatorward expansion of the auroral oval during the main phase and by

capturing high-speed moving ionospheric irregularities (up to ~800 m/s), and quantifying extreme ionospheric uplift (up to 1500 km) under conditions where conventional HF instruments were not usable due to the occurrence of D-layer absorption, ionospheric G-conditions and uplift above ionosonde altitude range.

These results further confirm LOFAR as an insightful instrument for ionospheric research, offering critical capabilities for advancing storm impact assessment, forecasting, and mitigation strategies.

The paper is structured as follows. Section 2 describes the LOFAR data and companion datasets, along with the velocity estimation techniques and the method for deriving an effective ionospheric altitude; Section 3 presents and discusses the key observational results, in particular during the main and recovery phases of the storm, focusing on the high-speed moving irregularities and extreme uplift. Finally, Section 4 provides the concluding remarks.

### 4.2.3. The storm conditions

In May 2024, several X-class solar flares originating from Active Region (AR) 13664 triggered multiple coronal mass ejections (CMEs)(Ippolito et al., 2025; Romano et al., 2024). These events culminated on May 10th–11th in the most significant geomagnetic storm since those observed in late 2003, hereafter referred to as the May 2024 Mother's Day Superstorm (Elvidge & Themens, 2025; Jin et al., 2025; Spogli et al., 2024), following the name convention which have been mostly used in Europe (Chabanski et al., 2025). Classified as an extreme G5-level geomagnetic storm, it was marked by the Kp index reaching its maximum value of 9 for a sustained period, a Dst index drop to –412 nT, and a SYM-H index minimum of –518 nT (Tulasi Ram et al., 2024). While the storm's peak intensity was estimated as a 1-in-12.5-year event, its prolonged duration, with Kp exceeding 8 for at least 24 hours, was exceptionally rare, corresponding to a 1-in-41 year event (Elvidge & Themens, 2025).

This superstorm triggered vast disturbances at global level, including widespread auroras seen at unusually low latitudes (Chernyshov et al., 2025; Elvidge & Themens, 2025; Foster et al., 2024; Kataoka et al., 2024; Spogli et al., 2024) and significant impacts on the ionosphere-thermosphere system (Jin et al., 2025; Ranjan et al., 2024; Themens et al., 2024; Tulasi Ram et al., 2024).

In the European sector, the storm prompted dramatic ionospheric disturbances, including fast-moving TEC enhancements, equatorward expansion of the auroral oval, poleward expansion of the Northern crest of the Equatorial Ionospheric Anomaly (EIA), and intense ionospheric scintillation phenomena triggered by ionospheric irregularities across a large range of scales.

Specifically, both in situ satellite measurements and ground-based Global Navigation Satellite System (GNSS) observations revealed a significant and rapid depletion of plasma density across high-to-mid latitudes (above 50° magnetic latitude) starting shortly after the storm onset (Jin et al., 2025). This plasma density depletion has been found to be prominent over the Mediterranean sector and Italy (Spogli et al., 2024), originated from a significant ionospheric trough and polar holes and expanded equatorward, lasting for approximately three days before recovering (Jin et al., 2025). This negative ionospheric storm phase is largely attributed to thermospheric composition changes, specifically a decrease in the [O]/[N_2] ratio driven by storm-time heating and circulation changes (Jin et al., 2025; Spogli et al., 2024). The depletion was so severe that the F2-layer was effectively absent over high latitudes on May 11th (Themens et al., 2024) and decreased by about 70% with respect to quiet conditions over the Italian mid-latitudes (Spogli et al., 2024). As highlighted by (Pierrard et al., 2025), the observed plasma depletion is likely attributable not only to reduced ionization within the F2 layer,

but also to a contracted plasmapause position. This interpretation supports the hypothesis that the pronounced electron density depletion is associated with plasmaspheric erosion processes.

In the initial storm phases, substantial plasma lifting occurred within the Storm Enhanced Density (SED) plume, with ionospheric peak heights (hmF2) increasing by 150-300 km, reaching up to 630 km over mid-latitudes in the American sector (Themens et al., 2024). Similar hmF2 increases were noted over Italy (Spogli et al., 2024). It has been also reported at low latitudes because of the prompt penetration of electric fields of magnetospheric origin (Fagundes et al., 2025) following the strongly undershielding conditions of the Region 1 and Region 2 Field Aligned Currents at the Interplanetary CME shock arrival (Wei et al., 2015). Wei This lifting contributed to initially enhanced plasma densities before the depletion phase dominated.

In this context, the extensive network of LOFAR radio antennas provides the precious opportunity to investigate the ionospheric response, focusing on the severely depleted, super-high-altitude plasma structuring found in Europe.

### 4.2.4. LOFAR data

The locations of the LOFAR antennas across Europe, with respect to other instruments, are reported in figure 4.14. The map shows the locations of the International Stations (red dots), along with the magnetometers of the IMAGE networks (blue dots) and European ionosondes (green dots).

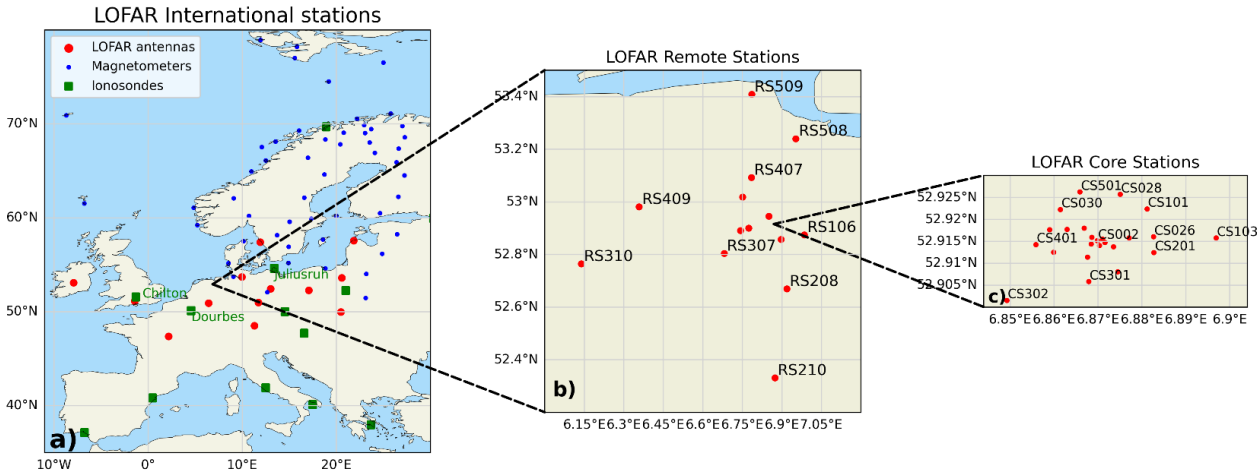



*Figure 4.14. Location of LOFAR International stations (red dots), IMAGE magnetometers (blue dots) and Ionosondes (green dots).*

There is a high density of ionosonde stations covering Europe with extensive East-to-West span and multiple local time zones as seen in figure 4.14. This spatial and temporal coverage is optimal for the validation of the East-to-West plasma drift in the vertical TEC (vTEC) maps, described below. As the plasma structures traverse the continent, the suggested station location at successively offset longitudes enables the same disturbance to be traced sequentially through multiple local-time sectors. The overview of ionosonde's data availability at various European stations between 9th May and 13th May 2024, colour-coding each ionospheric parameter (e.g., *hm*F2, *fo*F2, etc.) is seen in Annex A. White intervals represent periods where no data were collected, or the observation failed to produce valid measurements or if the confidence level of the data collected is unknown. Stations showing predominantly continuous colour bands have more complete records during the specified timeframe, whereas those with frequent white spaces or short colour segments indicate missing data thus resulting

in a lack of complete coverage of the ionosphere during that time period. The majority of the ionosondes were unable to produce a result in the morning of the 11th May, highlighting the importance of alternative measurements, at times when such "information blackout" is observed. For this reason, and for the needs to manually calibrate all ionograms due to the hardship of the storm, the following analysis from the ionosondes will focus only on the Juliusruh, Chilton and Dourbes ionosondes.

During the May 2024 Mother's Day superstorm, LOFAR was performing various standard interferometric observations for radio astronomical purposes either with the low band antennas (LBA: 10-90 MHz) or with the high band antennas (HBA: 110-190 MHz). The solar and ionospheric activity during geomagnetic storms make it difficult to interpret the data for astronomical sciences. However, the station autocorrelations of bright sources show rapid flux amplitude variations due to ionospheric scintillation and can and have therefore been used to study the ionosphere. Every LOFAR dataset contains the intensity of the signal coming from the source selected for the observation measured by every antenna. Data are at a 1 second temporal resolution and at a 0.195 MHz frequency resolution.

Among the LOFAR observations, it has also utilised the Incremental Development Of LOFAR Space Weather (IDOLS) dataset (*https://spaceweather.astron.nl/SolarKSP/data/website/#/*). IDOLS represents a unique operational mode within LOFAR's ionospheric monitoring capabilities, in which a single LOFAR core station (CS032LBA) collects high-resolution intensity data continuously over extended time periods. This setup enables long-duration tracking of ionospheric activity at a fixed location for space weather purposes, offering an uninterrupted view of scintillation and signal variability throughout the storm's evolution.

The period of available LOFAR observations, along with the K-index from Dourbes magnetometer and the electrojet indexs IE, IL, and IU derived by IMAGE magnetometers, are shown in Figure 4.15 and summarised in table *4.1*.

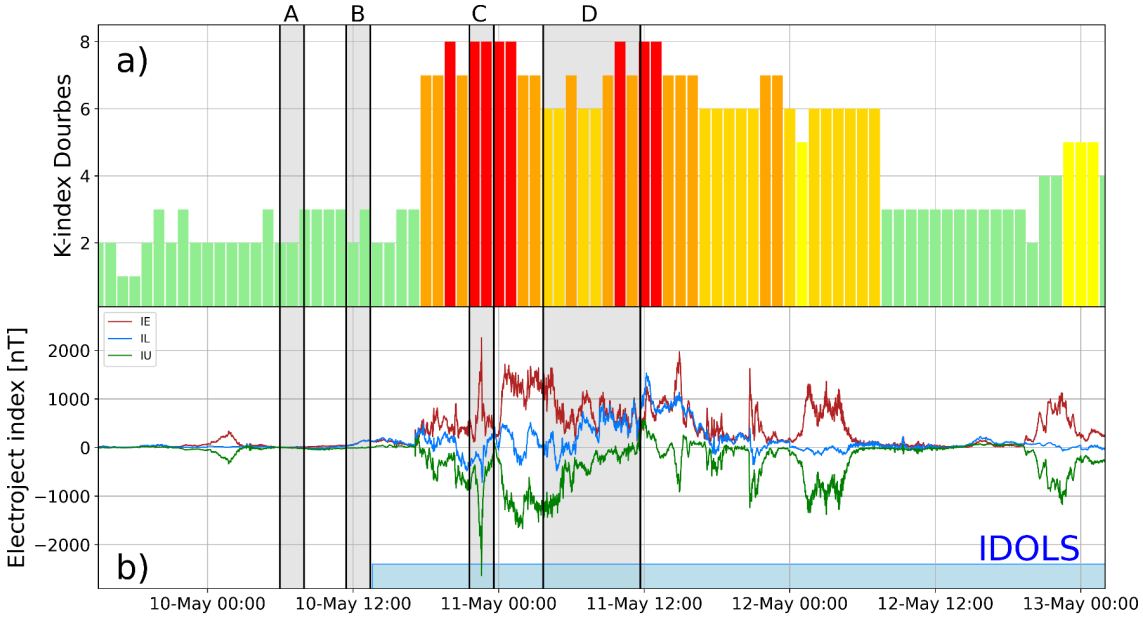



*Figure 4.15. Panel a) shows the K-index from Dourbes from 15:00 UT of May 9th until 02:00 UT of May 14th. The color of the bars indicates the NOAA Space Weather Scale for geomagnetic storms (*https://www.swpc.noaa.gov/noaa-scales-explanation*). Panel b) shows the electrojet indexes IE, IL and IU*

*for IMAGE magnetometers. The grey bars represent the five all-stations LOFAR observations while the blue one represents the period of available IDOLS data.*

| **Associated Letter** | **A** | **B** | **C** | **D** |
|---|---|---|---|---|
| **Observation ID** | L2040063 | L2040071 | L2040075 | L2040001 |
| **Source** | 3C48 | 3C196 | 3C380 | Cassiopeia A |
| **Antennas type** | LBA | LBA | LBA | HBA |
| **Date and Time (UTC)** | May 10th: 05:58 - 07:58 | May 10th: 11:25 - 13:25 | May 10th: 21:35 - 23:35 | May 11th: 03:40 - 11:40 |

**Table 4.1.** Details of the LOFAR observations employed in the analysis. The table provides the associated letter code for each observation, as reported in figure 2, the LOFAR observation ID, the observed celestial radio source, the antenna type used (LBA or HBA), and the start and end times (UTC) for each observation period.

### 4.2.5. May 10th 21:35-23:35 UTC (LOFAR dataset C - source: 3C380)

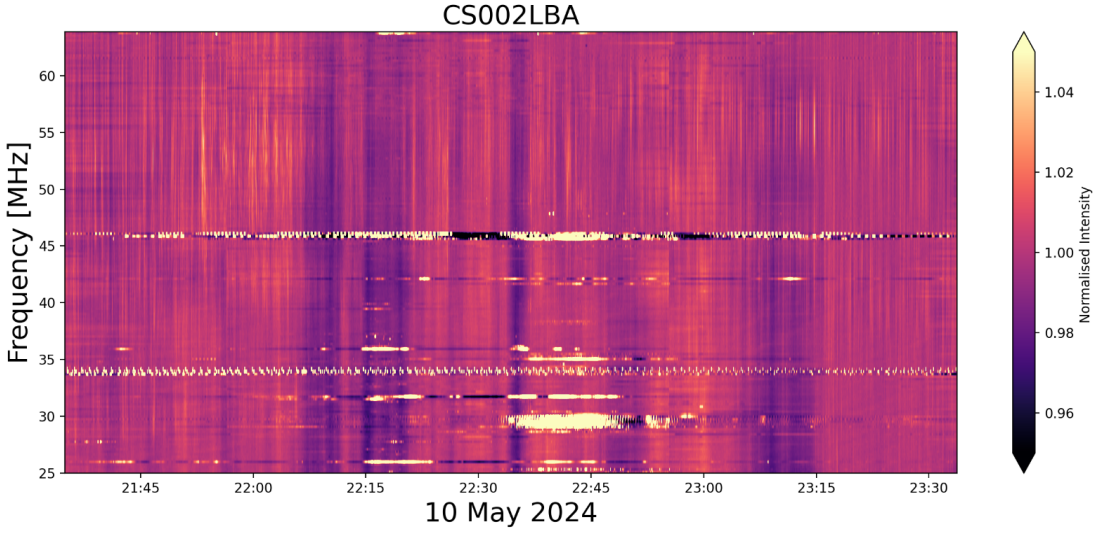



*Figure 4.16 LOFAR CS002LBA dynamic spectra for observation L2040075, covering the period of May 10th from 21:35 until 23:35 UTC. The astronomical source of the signal is 3C380.*

During the period from 21:35 to 23:15 UTC on May 10th, the dynamic spectra were recorded for both the Core and International LBA LOFAR stations, using 3C380 as the target radio source. An example of the dynamic spectra (CS002LBA) is shown in figure 4.16 while the other spectra are reported in

Annex B. It is noteworthy that 3C380's flux density is lower than other sources (i.e. Cassiopeia A), a factor that may introduce a significant challenge in achieving coherent signal reception. The data reveal that during periods of intense ionospheric activity, the ionosphere exhibits increased absorption of radio waves, particularly around 22:15 UTC and 23:15 UTC, as depicted by the darker stripes in all the core stations signals. To substantiate this observation, the complementary observational data were used to investigate the co-temporal ionospheric conditions. The resulting vTEC maps at six distinct time intervals during the LOFAR observation period are presented in figure 4.17. The colourbar in this plot is intentionally saturated at 25 TECu to enhance the visualization of the primary ionospheric behaviour within the 0-25 TECu range. In these maps, the green dots represent the IPPs of the LOFAR Remote and International LBA stations, projected to an altitude of 350 km. The rapidly evolving auroral oval is visible in yellow as a vTEC enhancement which is intersected by the IPPs, showing that LOFAR's line-of-sight passed directly through the auroral oval for a period of at least 2-hours during the peak of the storm.

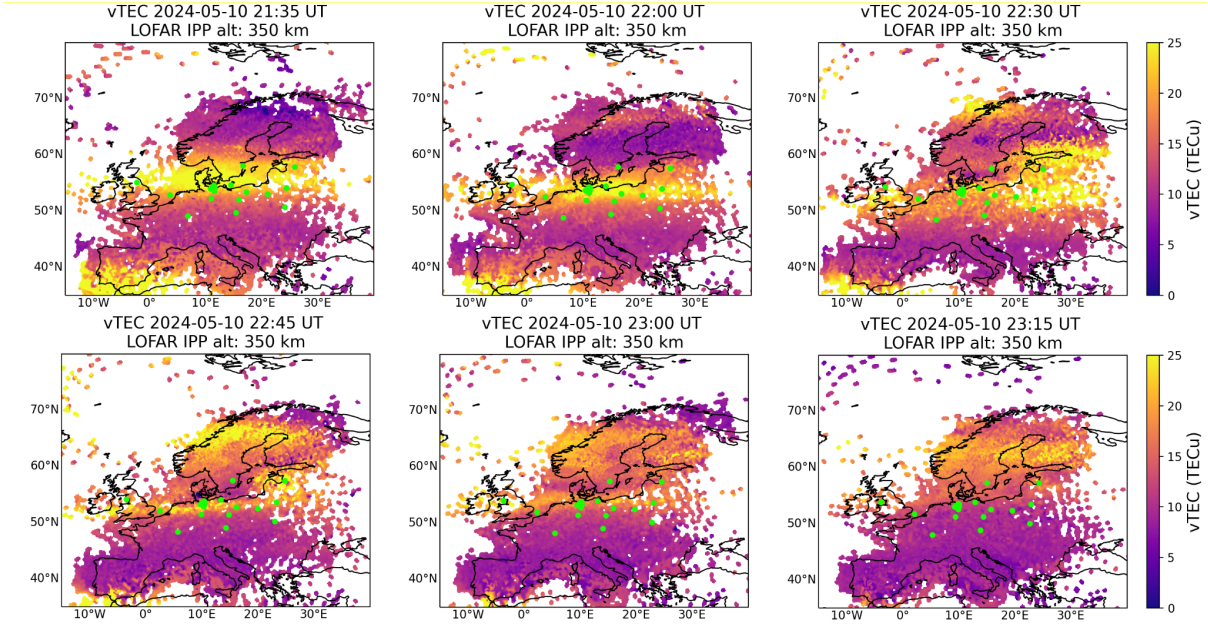



*Figure 4.17. Selected vTEC maps in the European sector for the period of May 10th from 21:35 until 23:15 UTC. The resolution is 1° in latitude and 1° in longitude. The green dots represent the position of the IPPs of LOFAR remote and international stations projected to an altitude of 350 km. Units are in TECu.*

The auroral nature of this disturbance is further confirmed by ionosonde observations from Juliusruh (top panels), Chilton (middle panels), and Dourbes (bottom panels) in figure 5.
Figure 4.18 shows a clear decrease in total echo power at Juliusruh, indicative of either attenuated echoes or a reduced number of echoes at 22:13, 22:18, 22:38, 22:43, and 22:48 UTC. Examining the ionograms (not shown), these decreases in total echo power is associated with an increase in the lowest frequency for which there is a return from the ionosphere (*fmin*) and reduction in echo power. These periods of elevated *fmin* and reduced echo power correspond well with the decreases in LOFAR amplitude seen at the German stations (Annex B), suggesting that those decreases in power were likely the result of enhanced medium and high energy particle precipitation, rather than scattering. Similarly, at Chilton, there is an increment of *fmin* at 22:10 UTC and 22:20 UTC (reduced total power after 23:10 UTC is due to there being fewer E-Region echoes rather than attenuation), and at Dourbes an

increment of *fmin* at 22:20, 22:25, and 22:35 UTC, which also correspond with the observed decreases in source power detected by LOFAR.
This type of absorption observed in LOFAR source data is typically associated with flaring activity. However, it is reported here to result from intense structuring of lower ionospheric layers due to the superstorm.

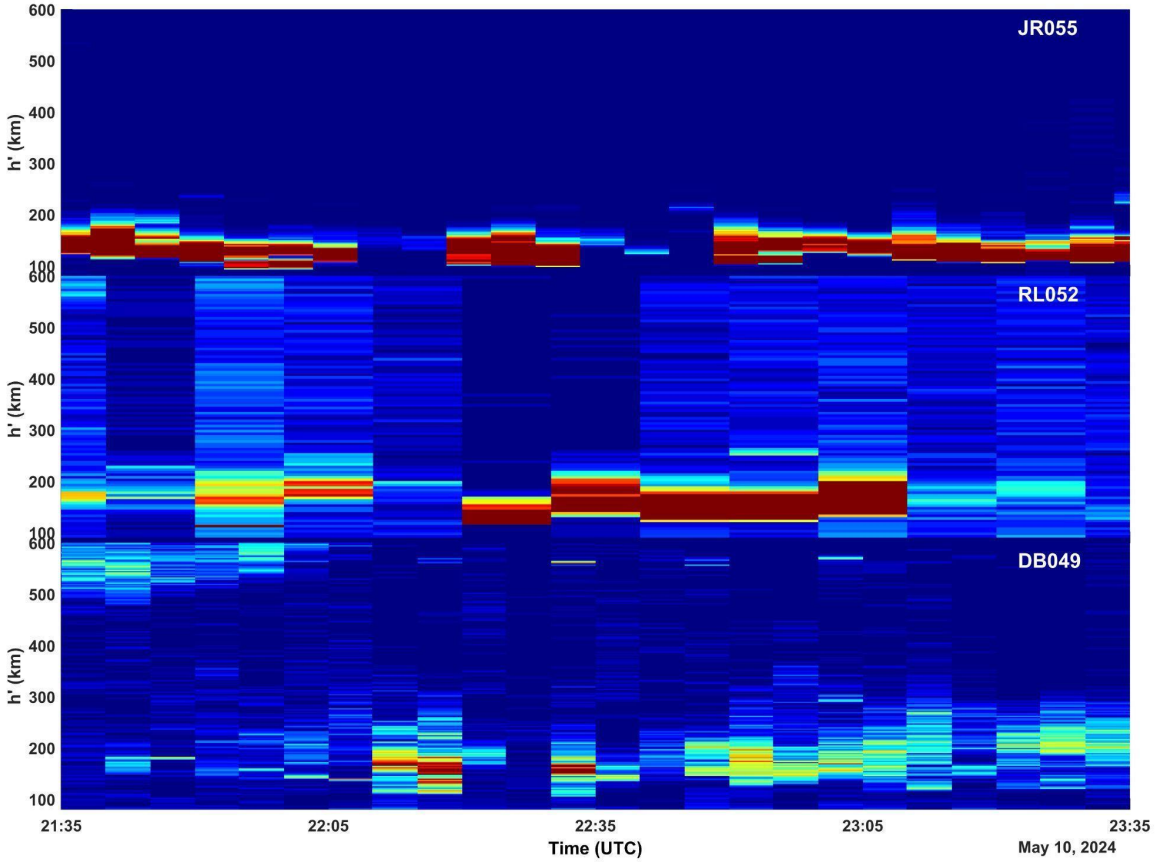



*Figure 4.18. Total echo power summed across all ionospheric echoes from the Juliusruh (top), Chilton (middle), and Dourbes (bottom) ionosondes between 21:35 UTC and 23:35 UTC on May 10$^{th}$, 2024. The plots were generated in arbitrary decibel units. Interpretation should be considered only qualitatively.*

To further corroborate that ionospheric irregularities sensed by LOFAR during the considered time interval are due to the equatorward displacement of the auroral oval, the disturbed magnetic field was analysed.

Figure 4.19 shows disturbed magnetic field reconstructed by the magnetometers in a latitudinal range from 40° - 70° N for the entire duration of the LOFAR observation. The solid black line represents the equatorward boundary of the auroral oval while the two white dashed lines represent the minimum and maximum latitude reached by the LOFAR IPPs projected at an altitude of 120 km, similar to what is reported in Figure 5. By further inspecting the available data from networks of SuperDARN radars (not shown) produced at temporal resolution of 2 minutes, fully demonstrates the equatorward expansion of the auroral boundary throughout the storm interval to be consistent with the solid black line illustrated within figure 4.19.

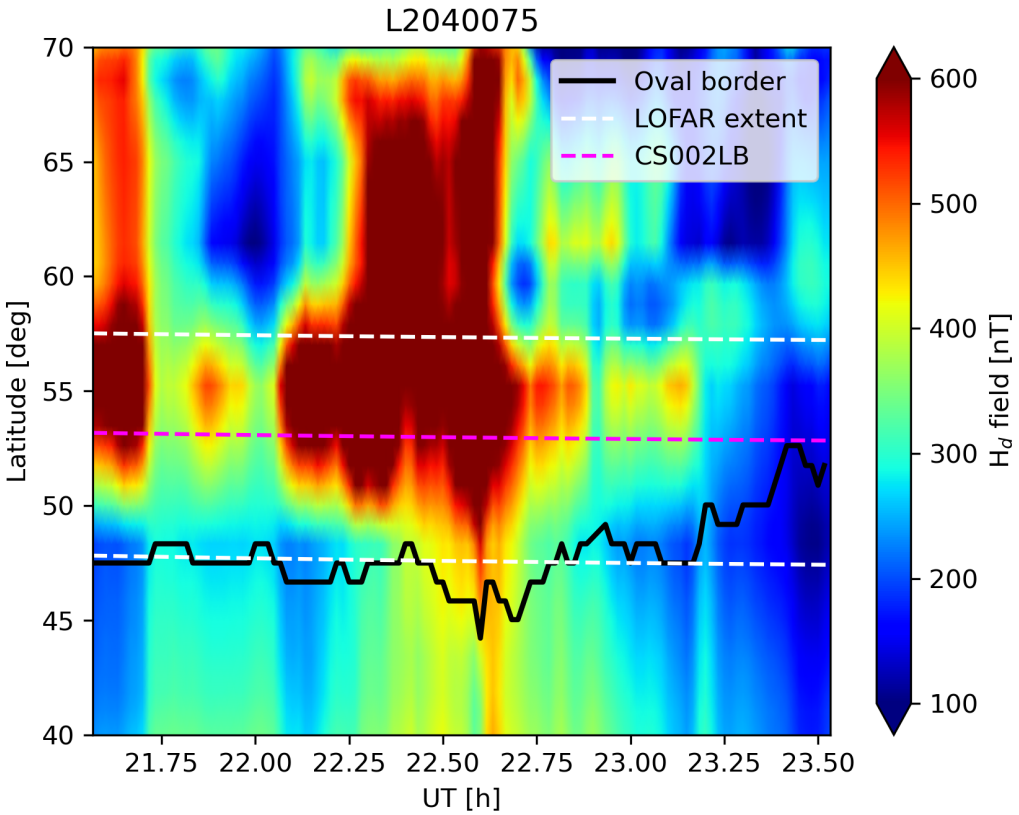



*Figure 4.19. Disturbance field measured by the magnetometers as a function of time and latitude. The solid black line represents the equator-ward position of the auroral oval while the two white dashed lines represent the minimum and maximum latitude reached by the LOFAR IPPs (from FR and SE stations respectively), while the magenta line represents the position of the CS002 IPPs. All the data are projected at an altitude of 120 km*

Additionally, figure 4.19 illustrates further that the LOFAR CS002 IPPs, projected at an altitude of 120 km, are located inside to the estimated boundary of the auroral oval, thereby supporting our hypothesis that the observed ionospheric disturbances are associated with E-layer irregularities located within the displaced auroral oval.

Taken together, these results — LOFAR fading, GNSS TEC enhancement, ionosonde evidence of auroral plasma, and magnetometer boundary shifts — all converge on a consistent physical interpretation: the LOFAR stations observed direct ionospheric effects from the equatorward expansion of the auroral oval during the peak of the May 10th storm. This multi-instrument validation highlights LOFAR's value in capturing mesoscale ionospheric responses.

### 4.2.6. May 11th 03:40-11:40 UT (LOFAR dataset D - source CASSIOPEIA A)

At the beginning of the superstorm's recovery phase, LOFAR demonstrated its uniqueness by capturing ionospheric dynamics under conditions in which all other ground-based instruments failed to provide a complete picture. To corroborate this, the first step is to examine the S4 index to assess the overall scintillation activity during the morning of May 11th. Figure 4.20 presents the S4 index

calculated over 180-second intervals for the LOFAR station CS002HBA0, spanning the period from 03:40 to 11:40 UTC on May 11th and across a frequency range of 110 to 190 MHz. The S4 measured for all the other core and international stations are reported in Annex C.

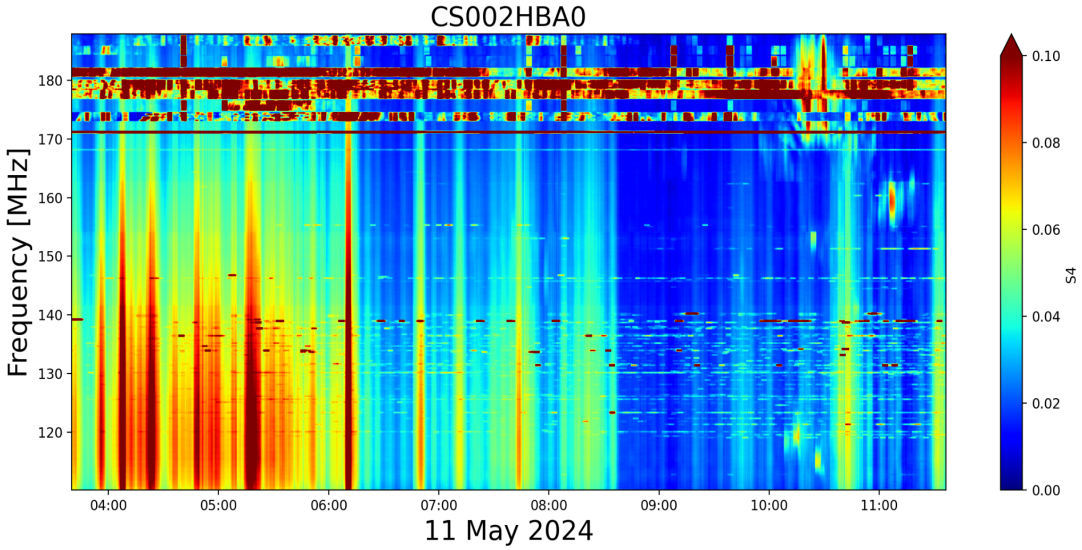



*Figure 4.20. LOFAR S4 data from CS002HBA0 for observation L2040001, covering the period of May 11th from 3:40 until 11:40 UTC. The astronomical source of the signal is Cassiopeia A. The plot represents the S4 index, measured at 180s.*

As expected, S4 patterns are very similar at all CSs, except for CS103HBA0, which displays elevated noise levels potentially originating from antenna-specific factors rather than ionospheric effects. The largest S4 values are observed before 06:00 UTC, while scintillation activity is almost absent after 09:00 UTC. The concurrent ionospheric conditions using vTEC maps at six distinct time intervals (04:00; 05:00; 06:00; 07:00; 08:00; 09:00 UTC) were investigated. These maps (Figure 4.21a) have a spatial resolution of 1° in latitude and 1° in longitude. In the maps, the green and the red dots represent the IPPs of LOFAR RSs and ISs projected to an altitude of 350 km.

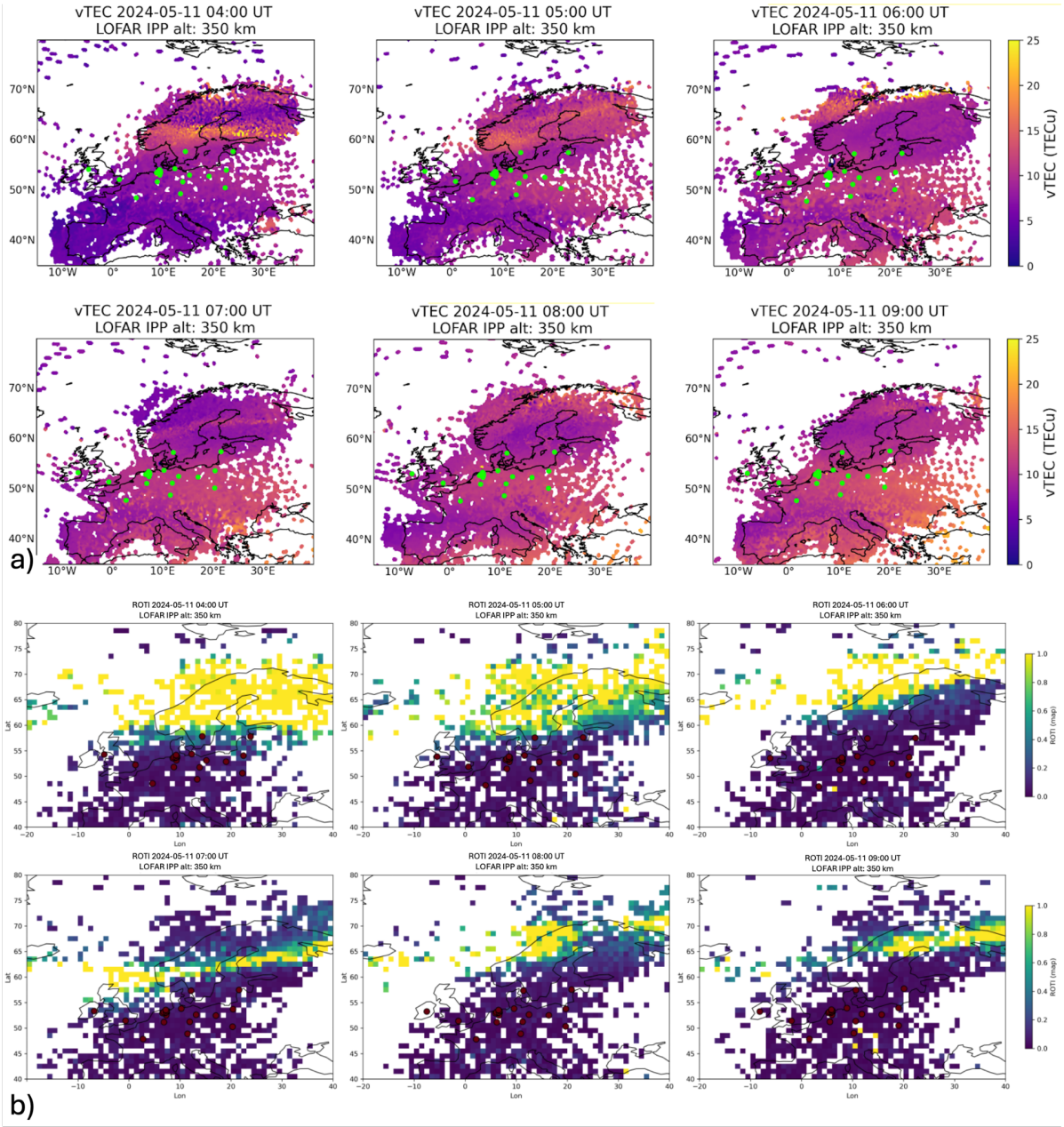



*Figure 4.21. vTEC (panel a) and ROTI (panel b) map on the European sector every hour for the period of May 11th from 04:00 until 09:00 UTC. The resolution is 1° in latitude and 1° in longitude. The green dots (Panel a) and the red dots (Panel b) represent the position of the IPPS of LOFAR Remote and International LBA antennas. All the data are projected at an altitude of 350 km. Units are in TECu.*

The vTEC maps in Figure 4.21a reveal consistently low values (always < 25 TECu) throughout the observational period, particularly evident after 05:00 UTC. ROTI maps (Figure 4.21b) highlights the boundaries of the auroral oval, however the geographical position of the oval depends on the assumed altitude for the projection of the IPPs. All the points of figure 4.21 are projected at an altitude of 350 km, which is questionable, as anticipated in the text and demonstrated further. This ambiguity complicates the interpretation of the physical processes responsible for the observed signal disturbances. To further investigate this phenomenon of reduced TEC and its potential implications

for auroral oval identification, the ionograms were analysed. In particular, the analysis focus on the data obtained from the Chilton, Dourbes, and Juliusruh ionosondes recorded from 04:00 UTC to 11:00 UTC on May 11th. The analysis of the ionograms reveals a dominance of absorption features and an absence of discernible traces. These types of the absorption features are also apparent within the spectrometers provided by Sodankylä Geophysical Observatory (*https://www.sgo.fi/Data/SpectRiometer/spectrioData.php*). During this period the ionosphere is in G-condition, meaning that the F2 layer has been significantly depleted and is either not present or is present but at a density lower than that of plasma density at peak F1 layer, $N_m F_1$. G-conditions make the reconstruction of the ionospheric vertical electron density profile, from the ionosondes data, impossible during the negative phase of the storm and the uplift event, as shown in Annex A.

To investigate the position of the LOFAR IPPs (at 120 km) with respect to the position of the AEB, figure 4.22 shows the disturbed magnetic field reconstructed by the magnetometers in a latitudinal range from 40° - 70° N for the entire duration of the LOFAR observation. The solid black line represents the position of the equator-ward position of the auroral oval while the two white dashed lines represent the minimum and maximum latitude reached by the LOFAR antennas - French (FR) and Swedish (SE) stations respectively -, while the magenta line represents the position of the CS002. In this case, the magenta line lies closer to the equatorward boundary of the auroral oval than it did on the night of May 10th, even extending below it at times.

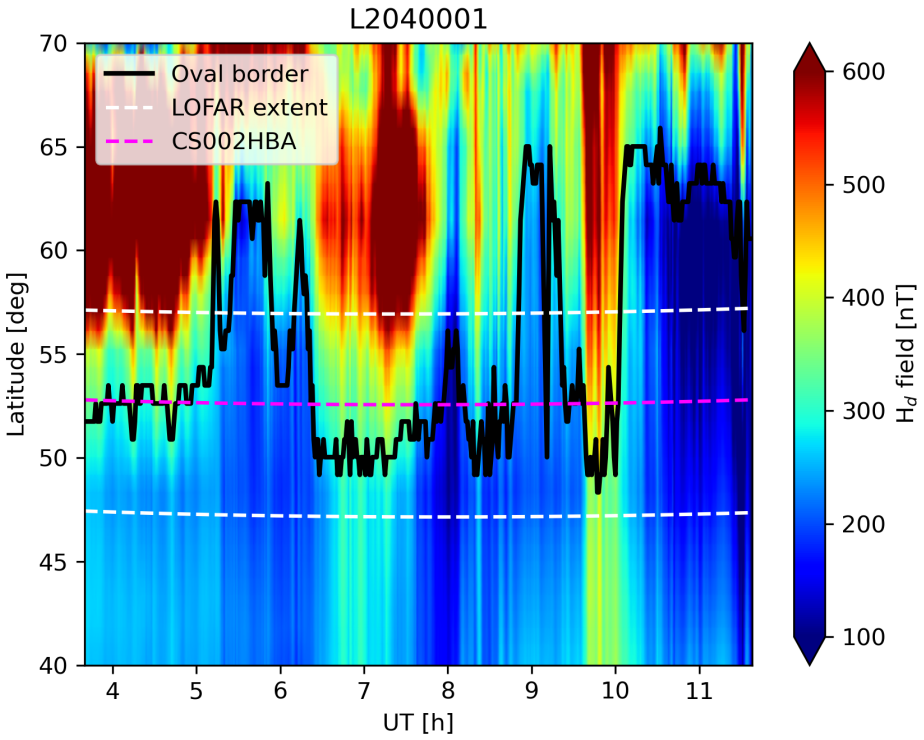



*Figure 4.22. Disturbance field measured by the magnetometers as a function of time and latitude. The solid black line represents the equator-ward position of the auroral oval while the two white dashed lines represent the minimum and maximum latitude reached by the LOFAR IPPs (from FR and SE stations respectively), while the magenta line represents the position of the CS002 IPPs. All the data are projected at an altitude of 120 km.*

Bearing in mind the limitations in assuming 120 km as the height of the IPPs, this configuration is associated with a weaker spectral disturbance, thereby enabling more reliable measurements of the velocity of sub-auroral structures, highlighted in the paper by Themens et al. (2024). Then, before proceeding with the velocity estimates with the methods reported in section 2.1.2 and 2.1.3, the robustness and reliability of Fresnel algorithm was checked against IDOLS observations and details of such a consistency check are provided in Annex D.

Figure 4.23 reports the velocities estimated by the two independent methods applied to the data at 140 MHz. The orange line represents the mean velocity of all the CSs obtained using Fresnel algorithm while the blue line represents the velocity obtained by the cross-correlation algorithm. The colour of the dots of the cross-correlation velocity represents the mean cross-correlation of every baseline at every time interval. To exemplify the comparison between the methods, both project the IPPs at an altitude of 350 km and the cross-correlation velocity has been projected in the same plane observed by the Fresnel algorithm, the plane perpendicular to the line of sight of the core stations' antennas.

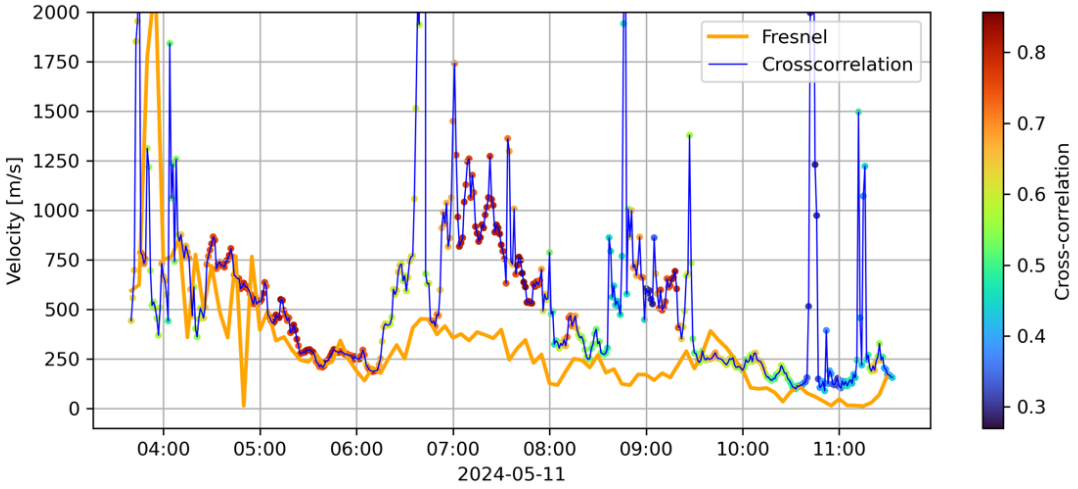



*Figure 4.23. Velocity estimates during the storm by using cross-correlation and velocity from Fresnel Frequency identification. The orange line represents the mean velocity of all the core stations obtained using Fresnel algorithm while the blue line represents the velocity obtained by the cross-correlation algorithm. The colour of the dots of the cross-correlation velocity represents the mean cross-correlation of every baseline at every time interval. Both algorithms refer to LOFAR intensity data at 140 MHz projected at an altitude of 350 km.*

When considering 350 km altitude for the ionospheric layer producing scintillations, both algorithms yield velocities of a similar order of magnitude (hundreds of m/s); however, discrepancies in the numerical values are evident, particularly during the interval from 06:00 to 09:30 UTC. After 9:30 UTC the mean cross-correlation starts lowering, this also corresponds to the period when the frozen-in assumption begins to fade, as checked by means of the method reported in Grzesiak et al. (2022).

#### *4.2.6.1. Effective altitude evaluation and comparison with ionosonde measurements*

Following the method described in Section 2.1.4, I estimate the effective altitude of the irregularity layer. The reader is reminded that, in principle, the Fresnel-based velocity can be retrieved with any instrument that has single-frequency capability roughly in the HF to L-band range and records signals with a Nyquist frequency meaningfully exceeding the Fresnel frequency for a specific wavelength and

observation geometry. In contrast, the cross-correlation-based velocity is specific to LOFAR CSs configuration, which enables the unique determination of the effective ionospheric altitude.

In figure 4.24a, the green line represents the effective altitude reconstructed by the comparison of the cross-correlation and Fresnel algorithms for the velocity reconstruction. The colour of the scatter plots represents the relative percentage error between the two velocity methods at the found effective altitude. S4 values, measured at the same frequency of 140 MHz, are also shown as a red line. The yellow line represents the $h_m F_2$ reconstructed by the Dourbes ionosonde, used as a reference. Data stopped around 4:35 UTC, after this time the ionosonde could not reconstruct the altitude. However, the result shows, even for just a short period of time, a reasonable match. The comparison algorithm can reconstruct a velocity for the entire duration of the observation. The altitude remains around 500 km until 6:00 UTC in the morning. Then there is a sudden jump over 1000 km. Around 8:30 UTC then the altitude starts uplifting and reaches 3000 km. This corresponds, however, to a region with a low S4 (<0.03). This decreases the reliability of both the cross-correlation and Fresnel algorithms and so the accuracy of the reconstructed altitude. It is indeed hard to believe that the ionosphere could have reached such a huge height, reminding how the meaning of the effective altitude must be carefully interpreted. This strong uplift in the European sector is among the most striking phenomena triggered by the superstorm, and LOFAR is currently the only instrument capable of providing an estimate of its actual magnitude. The upward displacement resulted mostly from increased Joule heating, which caused the thermosphere to expand rapidly. The heating in an expanded oval drives powerful storm-time thermospheric winds that blow equatorward. This created disturbed neutral composition changes and the large-scale plasma transport which produced the dramatic uplift (Pierrard et al., 2025).

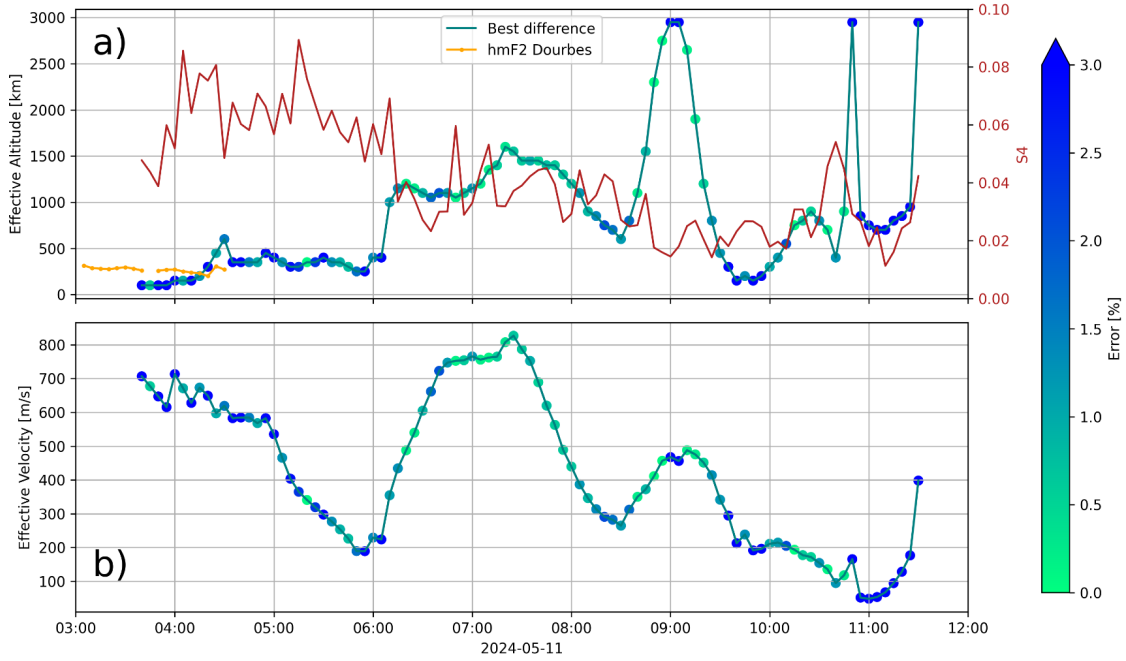



*Figure 4.24. In panel a) the green line represents the effective altitude reconstructed by the comparison of the cross-correlation and Fresnel algorithms for the velocity reconstruction. The color of the scatter plots represents the relative percentage error between the two velocity methods. The comparison is done with the velocities measured using the 140 MHz data, as reported in the*

*plot title. S4 values, measured at the same frequency, are also shown as a red line. Panel b) shows the velocity obtained, by the cross-correlation method, measured at the effective altitude. The color of the scatter plots represents the relative percentage error between the two velocity methods.*

Figure 4.24b shows the velocity obtained by the cross-correlation method at the effective altitude, with scatter plot colours representing the relative percentage error between the two velocity methods. At the maximum vertical displacement, the velocity was observed to ramp up to more than 800 m/s. This fast, mostly westward plasma flow is consistent with phenomena such as Polarisation Jets/Sub-Auroral Ion Drifts, similar to those reported in the American sector by (Themens et al., 2024) and in Eastern Europe by (Chernyshov et al., 2025). These phenomena are here detected by LOFAR as km-scale irregularities occurring below the AEB. This differentiate from the small-to-medium scale irregularities detected by the scintillation receivers in the Scandinavian sector within the auroral oval, reported partly in (Themens et al., 2024), and further investigated by checking the scintillation data from receivers in Finland managed by the Finnish Meteorological Institute and available in the electronic Space Weather upper atmosphere (*www.eswua.ingv.it*), managed by Istituto Nazionale di Geofisica e Vulcanologia (not shown). Furthermore, the increased westward flow is also consistent with the very low (down to about -1500 nT) values of the IU index (Figure 4.15b) that characterised the first half of May 11th. This indicates that strong electric fields in the inner magnetosphere map down to the subauroral region and drive the extremely fast plasma drift. To the best of our knowledge, LOFAR enabled this first and unique simultaneous observation of a deeply upward displaced and fast-moving ionosphere following the superstorm.

The retrieval of the effective altitude also provides a clearer picture of the geographical location of the irregularity layer, which is imprecise in TEC-based and other representations that assume a fixed altitude for the IPPs. Specifically, figure 4.25 illustrates the IPPs of LOFAR station CS002HBA0. These IPPs are projected onto both the effective altitude of the ionospheric irregularities (yellow-red markers) derived through our methodology and a fixed altitude of 350 km (blue markers). Notably, a discernible spatial displacement is observed between the IPP locations determined using the inferred effective altitude and those predicated on the conventional 350 km assumption. This discrepancy underscores the utility of our approach in refining the localisation of ionospheric irregularities perturbing LOFAR observations. The retrieved effective altitude demonstrates to be particularly valuable in conditions where ionosonde data are unavailable or inconclusive and constitute a peculiar measurement, possible only because of the joint use of the two methods on LOFAR data.

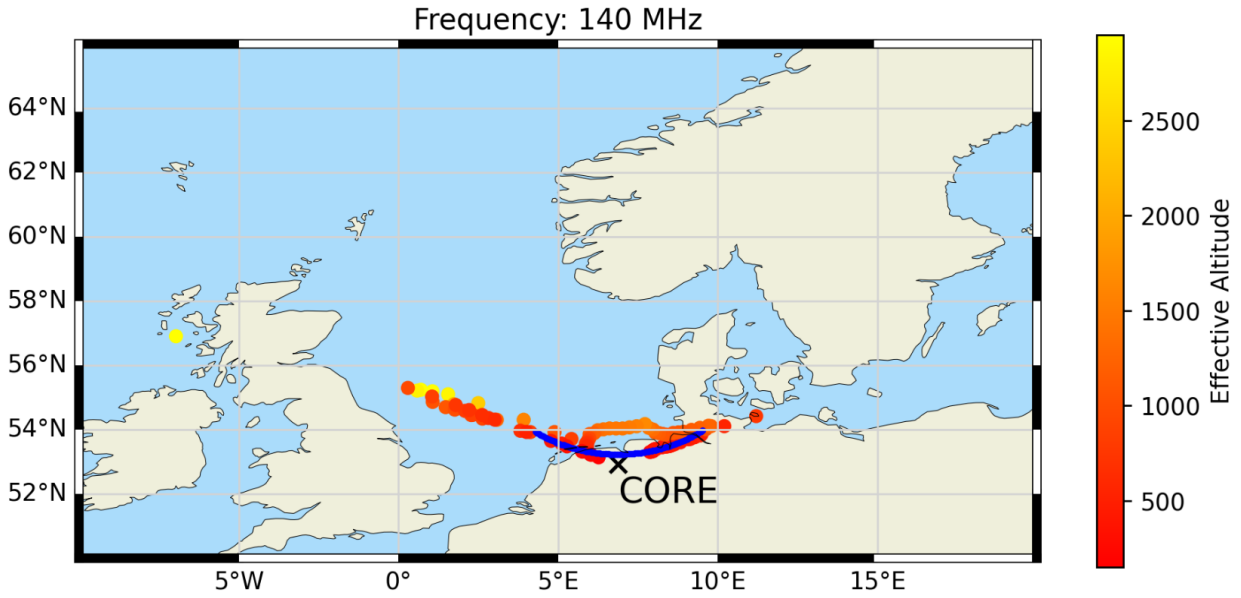



*Figure 4.25. Position of LOFAR CS002HBA0 IPPs (yellow-red dots) projected at the effective altitude and at an altitude of 350 km (blue dots). The black X represents the position of the LOFAR core stations.*

### 4.2.7. Final remarks

In this unprecedented investigation, the unique capabilities of the LOFAR radio telescope were harnessed to directly probe the structure and dynamics of the ionosphere during the most extreme space weather conditions of the last two decades. During the main phase of the superstorm, LOFAR LBA observations of the 3C380 source revealed significant signal fading, coinciding with the equatorward displacement of the auroral oval and related occurrence of E-layer irregularities due to particle precipitation. Furthermore, the favorable post-storm ionospheric conditions on May 12th, 2024 enable high-quality LOFAR observations of the redshifted H-alpha spectral line, suggesting geomagnetic activity may serve as a precursor for planning such observations. In addition to ionospheric disturbances, LOFAR also captured a class X 3.9 solar flare and an associated solar radio burst on the morning of May 10th (Annex E), demonstrating its capability to observe both solar and ionospheric phenomena during extreme space weather events. This analysis also allowed to demonstrate the importance of the study of geomagnetic storms for the astronomy community. As reported in Annex F, the IDOLS data clearly showed a disappear of significant ionospheric structuring between 09:00 UT and 16:00 UT of 12$^{th}$ May 2024

However, it is during the early hours of the recovery phase on May 11th that LOFAR revealed its uniqueness as an ionospheric probing instrument. Indeed, LOFAR HBA observations from Cassiopeia A between 04:00 UT and 11:00 UT allowed to reconstruct fast-moving ionospheric irregularities, for which it was estimated a drift velocities reaching up to ~800 m/s, associated with a strong upward displacement of the ionosphere, whose effective altitude reached up to 1500 km. LOFAR enabled this first and peculiar determination thanks to the application of two independent techniques - one based on cross-correlation and the other on Fresnel frequency analysis. Indeed, an ionospheric uplift the lower boundary of which has been found to be up to 1000 km in various sectors has been reported in the literature, based on ionosonde data (see, e.g., (Fagundes et al., 2025; Paul et al., 2025; Spogli et

al., 2024). However, this study derived the effective, time-resolved estimate of the ionospheric altitude. This approach is particularly valuable in conditions where ionosonde data are unavailable or inconclusive or when fixing the altitude of IPPs may lead to misleading interpretations.

The identified fast plasma flow has been ascribed to Polarisation Jets/Sub-Auroral Ion Drifts drifting mostly westward and coinciding with long-lasting conditions of strong westward auroral electrojet activity (IU index down to -1500 nT). The upward displacement resulted mostly from increased Joule heating, which caused the thermosphere to expand rapidly. The heating in an expanded oval drives powerful storm-time thermospheric winds that blow equatorward. This created disturbed composition changes and the large-scale plasma transport which produced the dramatic uplift observed over Europe. These results demonstrate the unique capability of LOFAR to provide precious ionospheric information under extreme space weather conditions, offering complementary insights where conventional ground-based instruments may provide a limited picture.

## 4.3. Climatological analysis

The preceding sections of this chapter have presented detailed case-study analyses of the January 2022 storm and the May 2024 Mother's Day superstorm. This event-based approach was essential for demonstrating LOFAR's advanced observational capabilities and for capturing high-resolution ionospheric dynamics during specific, highly disturbed periods.

However, the limited temporal scope of case studies cannot, by itself, determine the generalisability of these findings. It is necessary to ascertain whether the observed phenomena, such as the strong field-alignment of irregularities seen in the January 2022 event, are anomalous behaviours or if they represent a fundamental and persistent characteristic of the ionospheric plasma irregularities that LOFAR observes.

To bridge this gap between isolated, dynamic events and a generalised physical understanding, a comprehensive climatological analysis was conducted. This study moves beyond individual snapshots of storm activity to establish a robust statistical baseline of typical irregularity behaviour. By processing and analysing an extensive dataset encompassing over two years of observations, this analysis aims to validate the case study findings against a wide spectrum of geomagnetic conditions, from profoundly quiet to moderately active. This statistical context is indispensable for identifying dominant morphological characteristics, quantifying their underlying diurnal patterns, and ultimately, for correctly interpreting the significance of the extreme storm-time events.

In the following subsections, I will first describe the screening and selection criteria I applied to create a consistent dataset for this analysis. I will then present my statistical finding regarding the directional alignment of the measured irregularity velocities. Finally, I will investigate how this alignment is influenced by the intensity of ionospheric scintillation, thereby generalizing the key findings from my individual storm events.

### 4.3.1. Data screening and selection

The foundation of any robust climatological study is a dataset that is not only large but also statistically homogeneous. The complete LOFAR archive of observations for which velocity data was available

is extensive, comprising approximately 2800 hours of core station data collected over more than two years. To ensure the creation of a statistically robust and homogeneous final subset, a rigorous screening process was applied.

The primary and most critical selection criterion was the restriction of the entire analysis exclusively to observations targeting the celestial radio source Cassiopeia Alpha. This decision was underpinned by two fundamental justifications, one statistical and one technical.

First, from a statistical standpoint, Cas A is by a significant margin the most frequently observed source within the LOFAR archive. As illustrated in figure 4.26, the volume of Cas A observations vastly outnumbers all other targets (Cygnus Alpha (Cyg A) and Taurus Alpha (Tau A)).

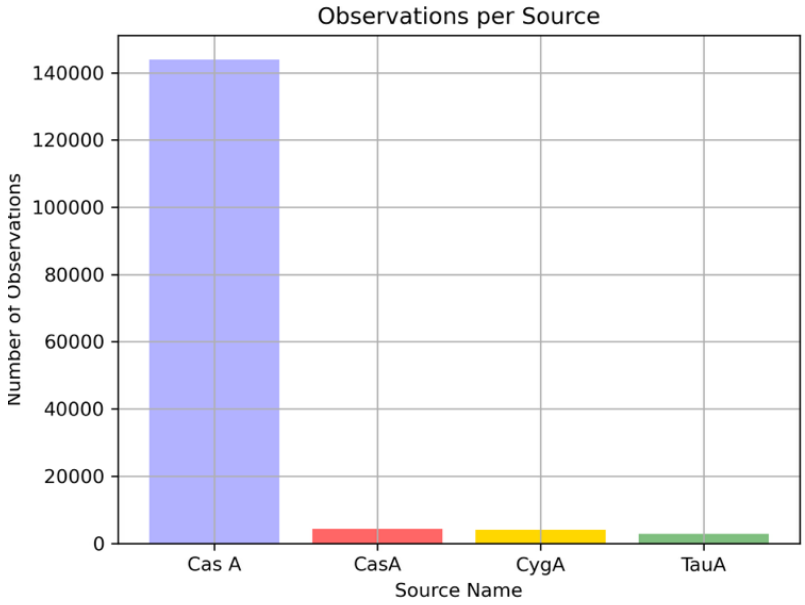



*Figure 4.26. Histogram of distribution of LOFAR observations radio sources*

Selecting only this source provides the largest possible dataset, maximizing the temporal coverage across different diurnal and seasonal cycles. This comprehensive coverage is essential for building a reliable climatology and identifying statistically significant trends.

Second, from a technical standpoint, Cas A is the brightest non-solar radio source at LOFAR's operational frequencies (Gasperin et al., 2020). This intrinsic brightness is a crucial practical advantage, as it guarantees a high signal-to-noise ratio (SNR) for the received signal. A high SNR is a fundamental prerequisite for the successful application of the cross-correlation velocity algorithm detailed in Chapter 3. This method relies on identifying the subtle, time-lagged peaks of the scintillation pattern as it passes across different stations. During periods of weak ionospheric activity, the scintillation signature itself is faint; a low-SNR observation (from a dimmer source) would be dominated by thermal noise, rendering the cross-correlation function unreliable and making the extraction of an accurate velocity vector impossible (Fallows et al., 2020). By focusing exclusively on Cas A, a high-quality signal is ensured, which maximises the reliability of the velocity measurements even during the quietest ionospheric conditions.

In addition to this primary selection, a minor data integrity check was performed. It was noted that a small subset of observations listed the source as "CasA" rather than "Cas A". This discrepancy was traced to a change in the data-saving algorithm used. Although the source is the same, the use of a different saving algorithm introduces a potential source of systematic error; it is possible that other, more subtle processing artifacts or metadata inconsistencies were also introduced. To maintain the strictest possible homogeneity and to eliminate this source of uncertainty, this small, anomalous "CasA" dataset was conservatively excluded from the final analysis.

The resulting, curated dataset thus consisted entirely of observations performed by the LBA core antennas, measuring intensity at a 0.1-second time resolution and ~200 KHz frequency resolution.

### 4.3.2. Results and discussion

Following the screening process, the final, curated dataset of Cassiopeia A observations consists of 2410 hours of intensity measurements recorded between July 2014 and August 2016. Those observations were performed during the early LOFAR cycles 0 and 1 (*https://www.lofar.eu/retirement-of-early-lofar-cycle-data/*).

Figure 4.27 illustrates the monthly (Left panel) and hourly (Right panel) distribution of the data. Both distributions are not uniform as they reflect the scheduling priorities for the LOFAR observations. Indeed, it is important to remember that LOFAR was mainly built to perform astronomy observations and therefore the observations usable for ionospheric analysis are mainly performed when other observations are not possible. The monthly distribution shows a higher density of observations during the winter and spring months, with a relative minimum during late summer. More significant is the diurnal distribution. It exhibits a clear bimodal pattern, with the majority of observations clustered in the post-midnight (approximately 02:00-06:00 UT) and post-sunset (approximately 16:00-22:00 UT) sectors.

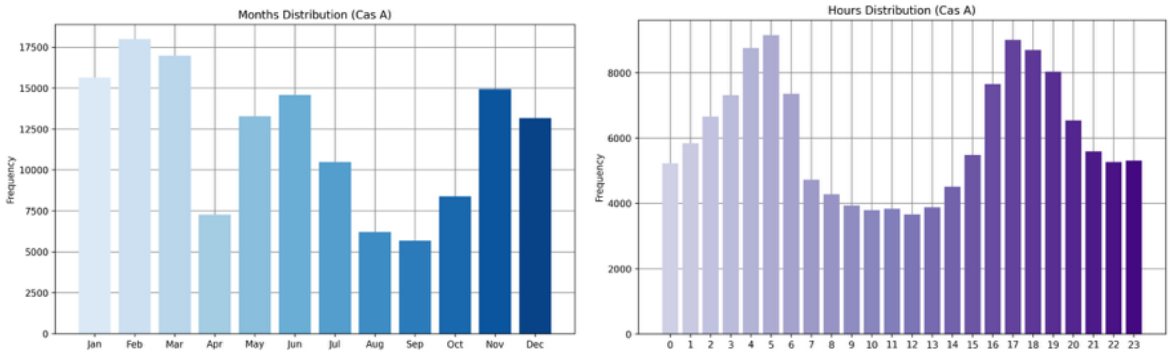



*Figure 4.27. Histograms of LOFAR observations monthly (left panel) and daily (right panel) distribution.*

After the selection process, the cross-correlation velocity algorithm, detailed in chapter 3.4, was applied to the remaining data considering a fixed altitude of the irregularity of 350 km. To minimise the computational demand the velocity was measured only for the data at 45 MHz every minute instead of the 30-seconds sliding windows applied for the storms analysis.

For every observation, additionally to the North-South and East-West component of the reconstructed velocity, other essential ancillary and quality-control data were considered. These ancillary data consist of the cross-correlation value across all baselines, the median S4 scintillation index simultaneously recorded by each core station, and the geographic coordinates of the IPPs corresponding to each station.

For this statistical analysis, most of the observation were performed at quiet ionospheric conditions. Figure 4.28 shows the number of observations in the dataset for different Kp index, together with the proportion of hours in the dataset which contain events in these ranges. Approximately 45% of the data corresponds to Kp<2, and a nearly equal proportion (~45%) is observed for 2≤Kp<4 range. Only the remaining ~10% of the data encompasses periods with Kp values ≥4.

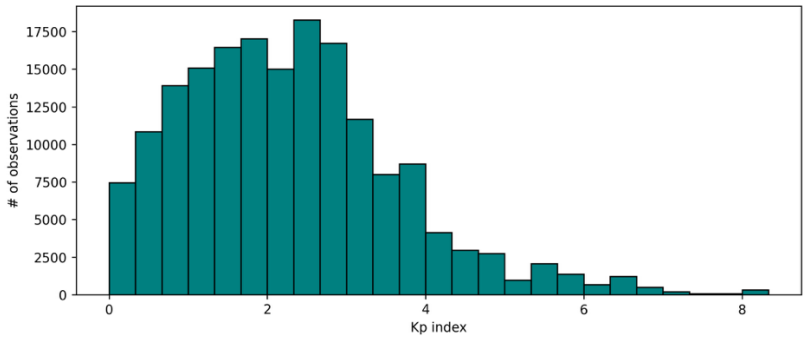



*Figure 4.28. Histograms of Kp-indexes values at each time at which the velocities were reconstructed.*

For this reason, the choice of a fixed altitude for the projected IPPs (at 350 km) for all the velocity measurements can be considered accurate.

From the ancillary variables, it is possible to investigate the relation between the ionospheric irregularities, of which it is possible to reconstruct the velocity, and the Earth's magnetic field, to understand the nature of the irregularities that mostly affects LOFAR observations. Similarly to what reported in chapter 4.1, also for this statistical study the Earth's magnetic field direction has been reconstructed, using the IGRF-13$^{th}$ generation, as described in chapter 2.2.6.

The most significant finding from this 2410-hour climatological analysis is that the measured velocity of the ionospheric irregularities exhibits a dominant and persistent field-alignment. This characteristic, first identified in the January 2022 storm analysis, is now confirmed as the fundamental baseline behaviour for the kilometre-scale irregularities LOFAR observes. This is demonstrated conclusively in figure 4.29, which plots the measured azimuthal velocity angle against sidereal time. The distribution of measurements, shown as blue dots, is clearly not random. Instead, the vast majority of points cluster tightly along the well-defined, red lines, which represent the predicted direction of $B \times LoS_{tg}$, reconstructed as described in chapter 4.1.3. This plot visually confirms that the irregularity motion detected by LOFAR is strongly constrained by the local magnetic field geometry relative to the observation's LoS.

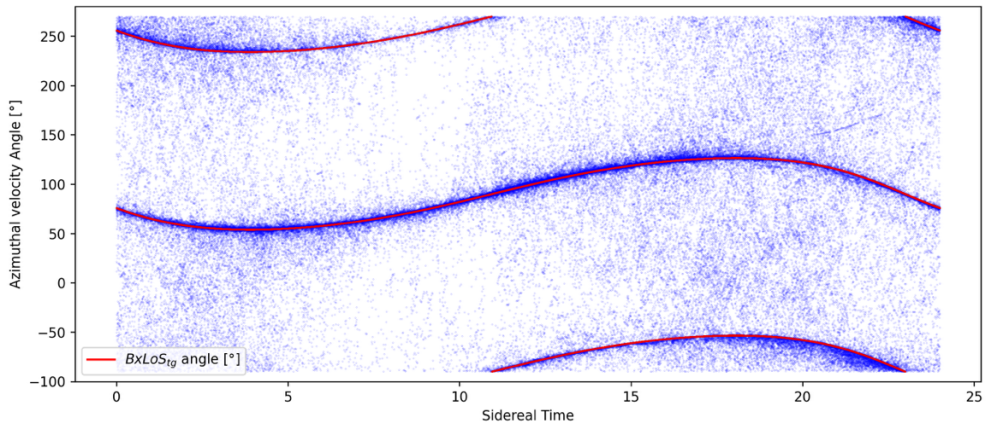



*Figure 4.29. Direction of the velocity (blue dots), reconstructed by the cross-correlation algorithm, as a function of sidereal time. The red lines represent the direction of the $B \times LoS_{tg}$.*

This visual evidence is quantified in figure 4.30, which presents a histogram of the absolute difference between the measured velocity angle and the $B \times LoS_{tg}$ direction. The distribution is sharply peaked near zero, indicating that a very large proportion of all measurements show a misalignment of only a few degrees. This result is critical: it statistically validates the case study finding and proves that the strong field-alignment is not an anomaly specific to geomagnetic storms but is, in fact, the default, underlying characteristic of the plasma structures being measured.

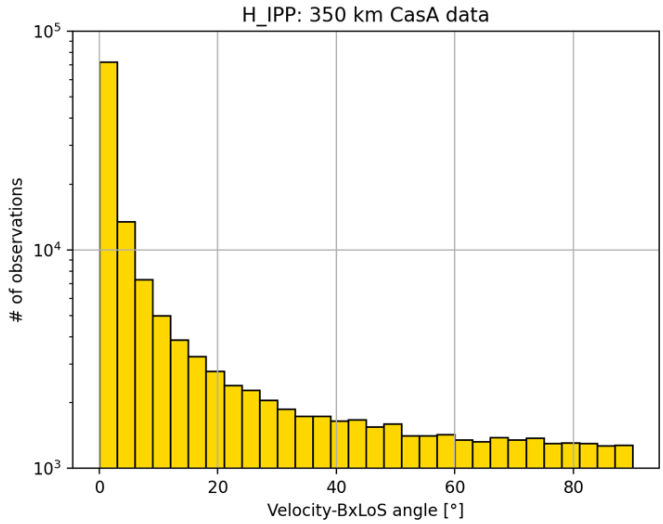



*Figure 4.30. Histogram of the distribution of the absolute difference between the azimuthal velocity angle and the $B \times LoS_{tg}$ projection.*

Further analysis revealed that this alignment is subject to several dependencies. A clear diurnal pattern emerged, as shown in figure 4.31, with the reconstructed velocity showing a much higher percentage of field-aligned structures during the nighttime hours compared to the daytime.

Figure 4.31 presents the diurnal distribution of the reconstructed velocity measurements from the Cas A dataset. The chart uses bars to illustrate the division between aligned and non-aligned structures as a function of the hour of the day. The total height of each yellow bar represents the total number of velocity measurements successfully reconstructed for that hour. This total dataset is then subdivided:

the dark red portion of the bar shows the count of "aligned" structures. For this analysis, "aligned" is defined as any measurement where the velocity's azimuthal angle has a difference of less than 9° from the calculated $B \times LoS_{tg}$ direction. Consequently, the upper portion of the bar (the difference between the total height and the red portion) implicitly represents the "not-aligned" structures, or those with a misalignment of 9° or more. The percentage reported above each bar quantifies the fraction of aligned structures relative to the total number of observations for that specific hour, clearly showing a higher prevalence of field-alignment during nighttime.

This 9° threshold was selected as a metric to distinguish between aligned and non-aligned structures because it represents 10% of the maximum possible absolute difference. As illustrated by the x-axis of the histogram in Figure 4.29, the absolute difference between the measured velocity azimuth and the $B \times LoS_{tg}$ direction is constrained, by definition, to a range between 0° (indicating perfect alignment) and a maximum possible value of 90° (indicating that the velocity is aligned perpendicular to $B \times LoS_{tg}$).

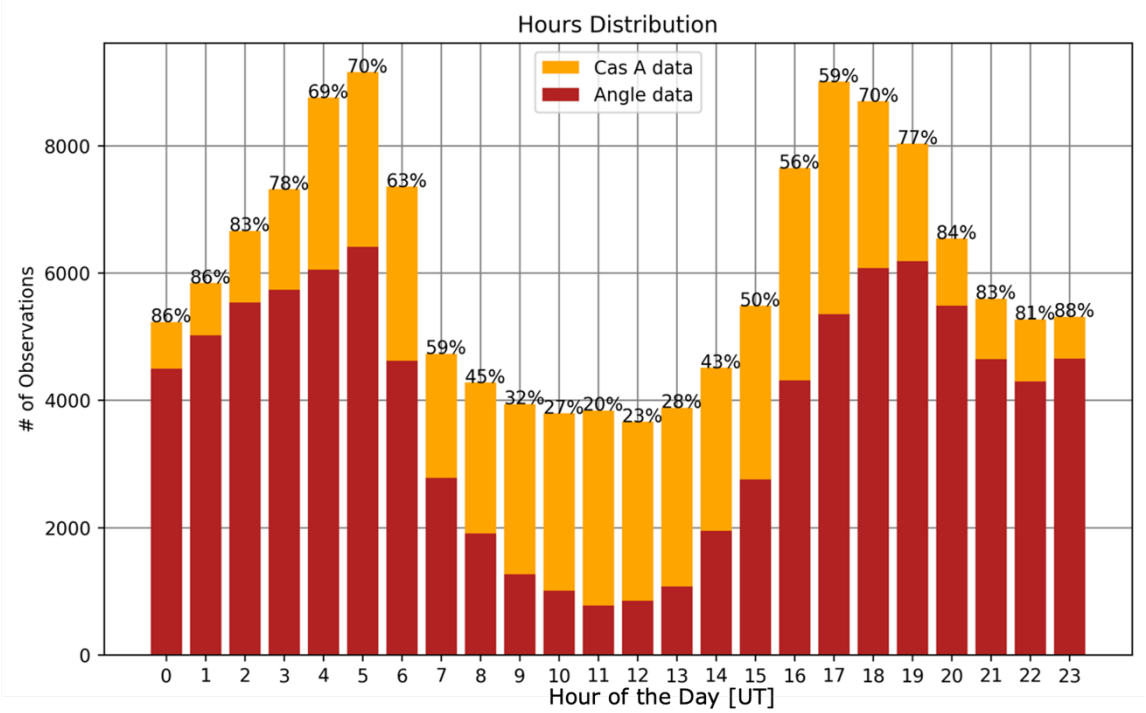



*Figure 4.31. Bar chart reporting the number of observations of Cas A (yellow bars) and the number of aligned structures (red bard) as a function of the hour of the day (UT). Above each bar it is reported the percentage of aligned structure with respect to the total number of structures reconstructed at that specific hour of the day.*

A second, and perhaps more telling, dependency of the velocity direction is on the intensity of the scintillation itself. Figure 4.32 is a two-part figure that graphically investigates the relationship between scintillation intensity S4 and the degree of field-alignment of the observed irregularities. The upper panel consists of a grid of 20 individual histograms, each corresponding to a specific 0.01-wide bin of the S4 index, ranging from "0.00 to 0.01" up to "0.19 to 0.20". Each histogram displays the distribution of the difference angle (between the measured velocity azimuth and the $B \times LoS_{tg}$ direction) on its x-axis, against the number of observations on a logarithmic y-axis. Annotations on each histogram quantify the mean and standard deviation of the distribution, as well as the percentage

of "Good" (aligned) structures, which are those falling within the 9° threshold. The lower panel of figure 4.32 provides a summary of this trend by plotting the fraction of aligned irregularities (the "Good" percentage from the upper histograms) on its y-axis against the S4 index on its x-axis. This line plot clearly demonstrates a positive correlation: as the S4 index increases, the fraction of aligned irregularities also increases, rising steeply from below 0.5 at very low S4 and plateauing at over 0.85 for higher S4 values. After this point, for S4 values greater than 0.125, the line begins to oscillate. This increased variability is likely attributable to the significantly lower number of total observations available in these high S4 bins (as evidenced by the histograms in the upper panel), which reduces the statistical accuracy of the calculated percentage.

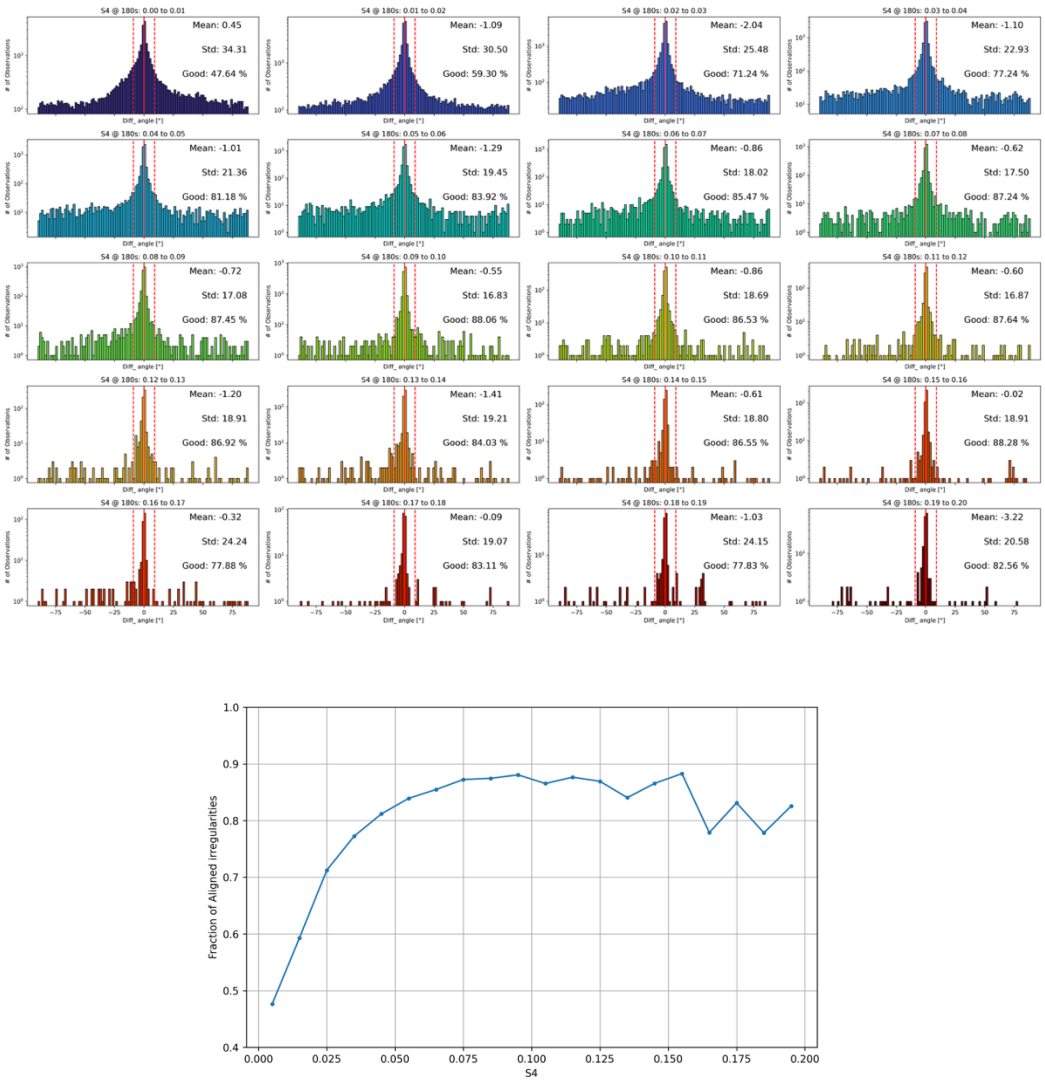



*Figure 4.32. The upper panel shows the histograms of the distribution of aligned and not-aligned structures. Every plot corresponds to a different subset of observations with varying S4 corresponding values, equally divided between 0 and 0.2. The lower panel shows the fraction of field-aligned structures as a function of S4.*

After analysing the dependency from S4, to probe the morphology of the irregularities themselves, the cross-correlation data at zero time-lag are analysed. For each time step, a two-dimensional (2D)

Gaussian was fitted to the spatial distribution of correlation values across all baselines, as exemplified in Figure 4.33.

The equation of the fitting function is given by:

$$CC = |A| \cdot e^{-\left(\frac{(cos(\theta)x+sin(\theta)y)^2}{2\sigma_x^2}+\frac{(-sin(\theta)x+cos(\theta)y)^2}{2\sigma_y^2}\right)} + \text{offset} \qquad (4.1)$$

Equation 4.1 defines the 2D-Gaussian function that is fitted to the cross-correlation data at zero time-lag. This function models the relationship between the spatial separation of the LOFAR station pairs and their measured signal cross-correlation. In this equation, CC is the dependent variable, representing the Cross-Correlation value at a lag of zero that is being modelled. The known independent variables are x and y, which represent the components of the baseline coordinates (i.e., the East-West and North-South spatial separation) between IPPs of each station pair. The remaining five terms are the unknown parameters determined through the best-fitting process. $A$ is the amplitude of the 2D Gaussian function, representing the peak correlation value relative to the offset. The rotation angle $\theta$ is a critical parameter that defines the orientation of the fitted ellipse, describing the morphological orientation of the irregularity pattern. The terms $\sigma_x$ and $\sigma_y$ are the standard deviations that define the width of the Gaussian along its two principal axes, with their ratio determining the anisotropy or elongation of the structure. Finally, the offset term represents a constant, baseline correlation value, accounting for the fact that the correlation may not fall to zero even at large separations.

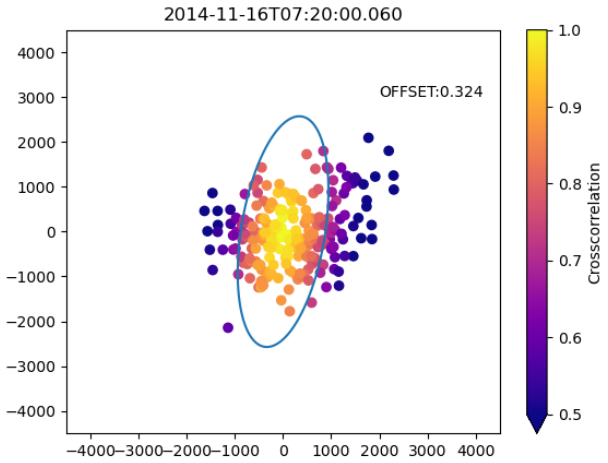



*Figure 4.33. Cross-correlation data at lag zero extracted from the observation performed November 16th, 2014 between 07:17 UT and 07:23 UT. The blue gaussian reports the 1-sigma boundary of the 2D fitted gaussian.*

This analysis revealed that the irregularities are consistently anisotropic, meaning they are elongated rather than circular, and that their major axis is oriented perpendicular to the reconstructed velocity vector. An even more subtle and powerful result emerged from analysing the temporal stability of this elongated shape. Figure 4.34 plots the measured velocity angle with the colour scale representing the stability of the irregularity's orientation over time over a surrounding 7-minute (7-point) window (three minutes before and three minutes after). Darker colours represent a very small difference, indicating high stability, while lighter colours represent a large difference, indicating instability. The resulting image shows that the tight, field-aligned bands are also the most stable. This 7-minute

interval was selected as an optimal coherence timescale to distinguish persistent, physically significant structures from transient fluctuations or noise. This window is long enough to average out rapid, high-frequency noise and the effects of very small-scale, quickly evolving irregularities. At the same time, it is short enough to capture the persistent orientation of the dominant, stable structures being tracked, without overly smoothing or averaging out the genuine, underlying ionospheric characteristics.

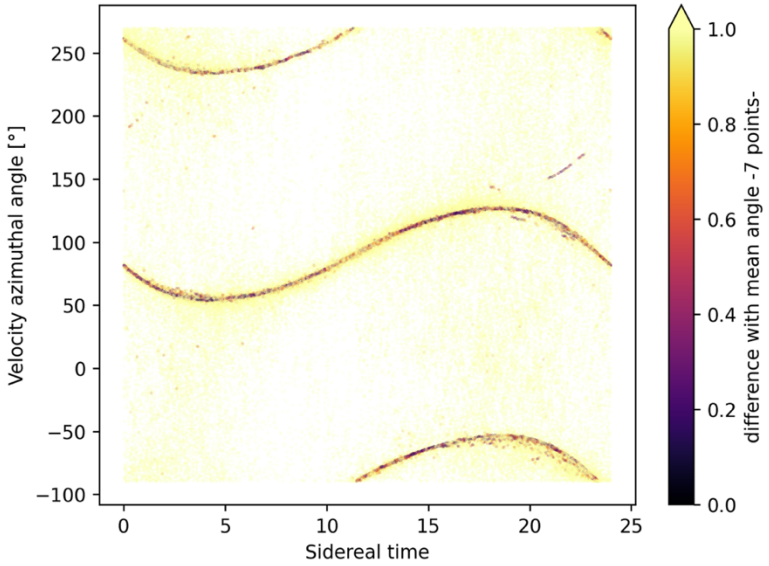



*Figure 4.34. Velocity azimuthal angel as a function of sidereal time. The color represents the difference of the direction of the major axis of the fitted gaussian with the angle obtained by the mean of the directions of the major axis obtained in the three minutes before and after, with darker shades representing smaller differences.*

The plot indicates that only the structures with high temporal coherence—those that are persistent and physically stable over several minutes—are the ones that perfectly align with the magnetic field direction. This strongly suggests that the algorithm is successfully isolating physically real, field-aligned ionospheric plasma structures from more transient or non-ionospheric noise.

The final step of the climatological analysis focused on identifying a physical cause for the non-aligned velocity measurements by comparing them with external parameters from other instruments. For this specific part of the analysis, the azimuthal velocity direction data are presented using a 180° module. This methodological choice is deliberate, designed to focus purely on the axis of alignment rather than the specific vector direction. The cross-correlation algorithm, as implemented, can occasionally produce velocity vectors that flip by 180°, even though both directions are physically constrained by the same magnetic field line. By applying a 180° module, these directional flips are ignored. This allows the analysis to clearly distinguish between structures that are aligned with the magnetic field (regardless of their polarity) and those that are truly non-aligned.

The most significant finding from this comparison was a strong correlation with the presence of Sporadic-E (Es) layers. This was established using data from the Dourbes ionosonde, which is located ~300 km away from the LOFAR core stations. The evidence for this is presented in Figure 4.35. The left panel plots the 180°-modulo velocity azimuth against time and sidereal time, while the right panel overlays the detection of Es layers as black dots.

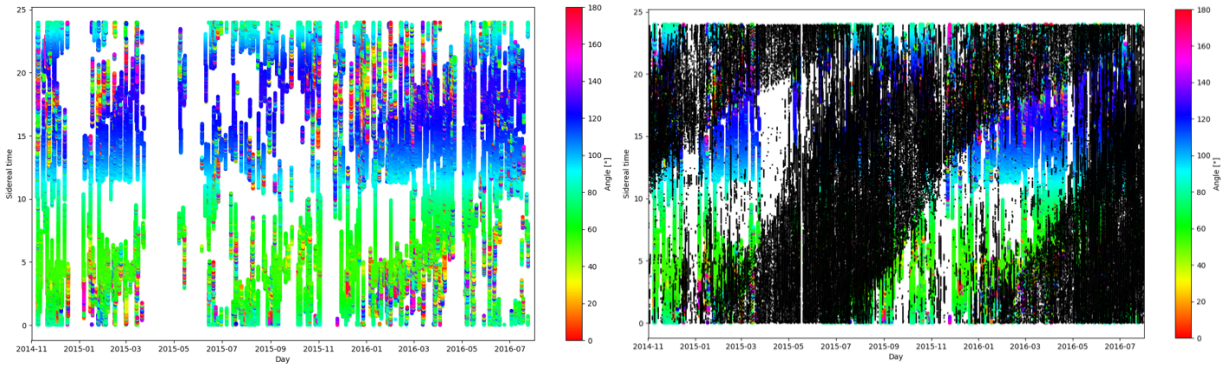



*Figure 4.35. Left panel represents the azimuthal angular direction of the reconstructed velocity as a function of time (x-axis) and sidereal time (y-axis). The right panel report the same plot on the left with the addition, as black dots, of the times for which the Dourbes ionosonde reported the presence of a sporadic-E layer*

In these plots, the expected field-aligned measurements are visible as stable green and blue bands that follow a sidereal time variation (as they are tracking the star, Cas A).

However, these stable bands are clearly "corrupted" by anomalous, colourful stripes that follow a daily time pattern. A heuristic correspondence is evident between these anomalous stripes and the presence of the Es layer (the black dots in the right panel).

This suggests that the sporadic-E layer itself, at ~90-140 km, can become the dominant irregularity layer responsible for the scintillation observed by LOFAR. However, the algorithm fails to correctly characterise these structures for two fundamental reasons. First, the very nature of sporadic-E layers—being "sporadic"—means the irregularities they generate are often not temporally coherent. As established in the analysis of figure 4.34, the cross-correlation algorithm is most reliable when tracking structures that are stable for several minutes. The erratic and quickly evolving nature of sporadic-E irregularities fails this coherence test, making them impossible to track. Second, the presence of these structures at a low altitude violates the algorithm's single thin-screen assumption of a 350 km F-region layer. This combination of a lack of temporal coherence and an incorrect altitude model could cause the velocity reconstruction to fail, producing an erroneous, seemingly random, non-aligned velocity vector. This explains why the daily-varying, Es-generated data in Figure 4.35 is distinct from the stable, sidereally varying, field-aligned F-region structures.

This suggests a practical application: by monitoring co-located ionosonde data, it is possible to assess the a priori reliability of the LOFAR velocity algorithm, thereby saving significant computational resources by avoiding analysis during periods of known strong sporadic-E contamination.

# 5. Conclusions

This thesis was conceived to provide a new perspective on ionospheric monitoring by leveraging the unique capabilities of the LOw Frequency ARray (LOFAR) radio telescope. The primary objectives were threefold: first, to rigorously validate LOFAR as a robust instrument for ionospheric diagnostics against established geospace instrumentation; second, to extend its scientific utility to the challenging domain of extreme space weather; and third, to construct a long-term climatological perspective on the irregularities LOFAR observes.

This research has successfully met these objectives, demonstrating that LOFAR is not merely a viable tool, but an indispensable one for modern space weather research, providing observational capabilities that are unavailable to conventional systems. The main contributions of this work and their implications for future research are synthesized below.

## 5.1. Summary of relevant outcomes

The scientific contributions of this thesis have been presented by progressively moving from instrument validation to extreme event analysis and, finally, to long-term statistical characterization.

A foundational outcome of this work was the successful validation of LOFAR-derived metrics against GNSS data. The analysis of the January 2022 geomagnetic storm revealed a distinct mismatch between LOFAR-derived S4 and GNSS-derived ROTI in the sub-auroral region. This was demonstrated to be a direct consequence of the different scale sizes the instruments are sensitive to LOFAR's high-resolution data captured small-scale irregularities (<10 km) that were averaged out by the 30-second sampling of the GNSS data. This finding not only validates LOFAR's precision but confirms its ability to probe a finer, kilometre-scale regime of plasma turbulence.

Building on this validation, this thesis demonstrated LOFAR's unique operational resilience during the most severe space weather event of the last two decades. During the May 2024 "Mother's Day" superstorm, LOFAR provided continuous, high-quality data even when conventional instruments, such as the European ionosonde network, were rendered inoperable due to widespread absorption and G-conditions. This resilience enabled the application of a novel algorithm developed in this research to retrieve the effective altitude of the irregularity layer. This method, which uniquely combines cross-correlation and Fresnel-based velocity estimates, quantified a dramatic ionospheric uplift event, with the effective altitude reaching up to 1500 km. This was the first known simultaneous observation of this extreme uplift and its associated high-speed (~ 800 m/s) plasma drifts, a measurement made possible only by LOFAR's specific configuration.

Finally, the climatological analysis of over 2400 hours of observations generalized the findings from the case studies. This study confirmed that the plasma irregularities observed by LOFAR are fundamentally characterized by a strong field-alignment. This alignment was shown to be a dominant feature of the nighttime ionosphere and to correlate positively with scintillation intensity. The analysis also characterized the morphology of the irregularities, revealing a persistent anisotropic (elongated) shape oriented perpendicular to the velocity vector. This establishes a robust statistical baseline for the kilometre-scale irregularities at high-to-mid latitudes

## 5.2. Future Developments

The methodologies developed and the findings presented in this thesis open several promising avenues for future research. A primary and immediate path forward involves the refinement and subsequent large-scale application of the novel effective altitude retrieval algorithm. While this algorithm proved its unique value during the May 2024 superstorm, its accuracy is intrinsically linked to the Fresnel velocity estimation, which was noted to have limitations based on the power spectrum's roll-off frequency. Future work should therefore focus on refining this algorithm, potentially by incorporating the phase spectrum method, which may provide a more robust and accurate determination of the Fresnel frequency. Future work should therefore focus on refining this algorithm to provide a more robust and accurate determination of the Fresnel frequency. This can be achieved by a method based on the Cross Normalised Power Spectral Density (Song et al., 2025).

Once this more advanced algorithm is validated, it should be applied to the full climatological dataset established in this work. This would represent a significant methodological advancement for the field, enabling the community to move beyond the ubiquitous but static 350 km thin-screen assumption, despite the limitation of the narrow ionospheric range scanned by LOFAR CSs. The result would be the first statistical model of the irregularity layer's effective altitude, allowing for a comprehensive characterization of its dependencies on geomagnetic activity, season, and local time.

Furthermore, a significant avenue for future work lies in exploiting LOFAR's unique broadband capabilities to investigate the frequency dependence of scintillation. This thesis has used the S4 index at specific frequencies (e.g., 60 MHz and 140 MHz) as a primary metric. However, LOFAR observes across a wide, continuous frequency range within its LBA and HBA bands. A dedicated study on the frequency dependence of the S4 index would be highly valuable. According to scintillation theory, $S_4$ is expected to follow a power-law relationship with frequency ($S_4 \propto \nu^{-k}$). However, a preliminary study on this dependency has revealed a violation of this scaling. It could be interesting to investigate the behaviour.

This improved methodological framework will, in turn, enable a more sophisticated investigation into the fundamental physics of irregularity generation and coupling. The analysis of the January 2022 storm, for instance, highlighted that the direct causal link between the small-scale (<10 km), field-aligned irregularities detected by LOFAR and the large-scale Travelling Ionospheric Disturbances (TIDs) observed by GNSS remains an open question. Future research, armed with a dynamic altitude model, could focus on this multi-scale coupling. A key strategy will be to integrate LOFAR data with co-located, high-rate (e.g., 1 Hz) GNSS receivers to bridge the observational gap that currently exists between the two measurement regimes.

Finally, this research has confirmed LOFAR's powerful dual-use capability, opening a new path for interdisciplinary collaboration. The discovery that the ionosphere can become exceptionally quiet and depleted in the recovery phase of a major storm presents a unique opportunity for the radio astronomy community. Future work could explore the feasibility of using high geomagnetic activity as a predictive precursor, allowing for the strategic scheduling of sensitive, very-low-frequency (e.g., <20 MHz) astronomical observations during these transient "windows" of extreme ionospheric clarity.

# Annex A

In figure A1, white intervals represent periods where no data were collected, or the observation failed to produce valid measurements or if the confidence level of the data collected is unknown. Stations showing predominantly continuous colour bands have more complete records during the specified timeframe, whereas those with frequent white spaces or short colour segments indicate missing data thus resulting in a lack of complete coverage of the ionosphere during that period.

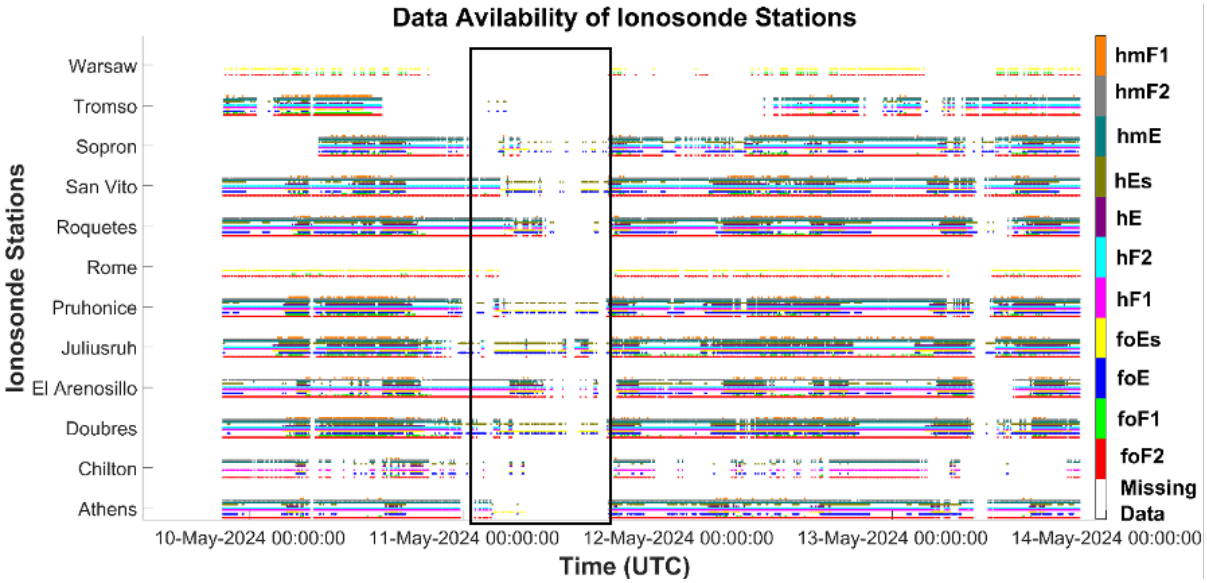



**Figure A1.** Data availability for multiple European ionosonde stations from 9 May to 14 May 2024, with each coloured bar representing a specific ionospheric parameter (e.g., foF2, foF1, etc.) measured at a given station over the set time. The black rectangle highlights the morning of 11 May, when the European ionosonde network experienced an "information blackout".

# Annex B

Figures B1 and B2 present the complete set of normalised dynamic spectra for the LOFAR observation L2040075, which is analysed in Section 4.2.3. These data were collected on May 10th, 2024, between 21:35 and 23:35 UTC, using the Low Band Antennas (LBA) to observe the celestial radio source 3C380. Figure B1 specifically displays the spectra for the Core Station CS002, Remote Station RS106, and all International LBA stations. Figure B2 provides the corresponding spectra for the full set of LOFAR Core LBA stations. As discussed in the main text, 3C380 is a fainter source than Cassiopeia A, which can increase the challenge of signal reception during disturbed conditions. These plots clearly show correlated signal fading, visible as dark horizontal and vertical stripes across nearly all stations, particularly around 22:15 UTC and 23:15 UTC.

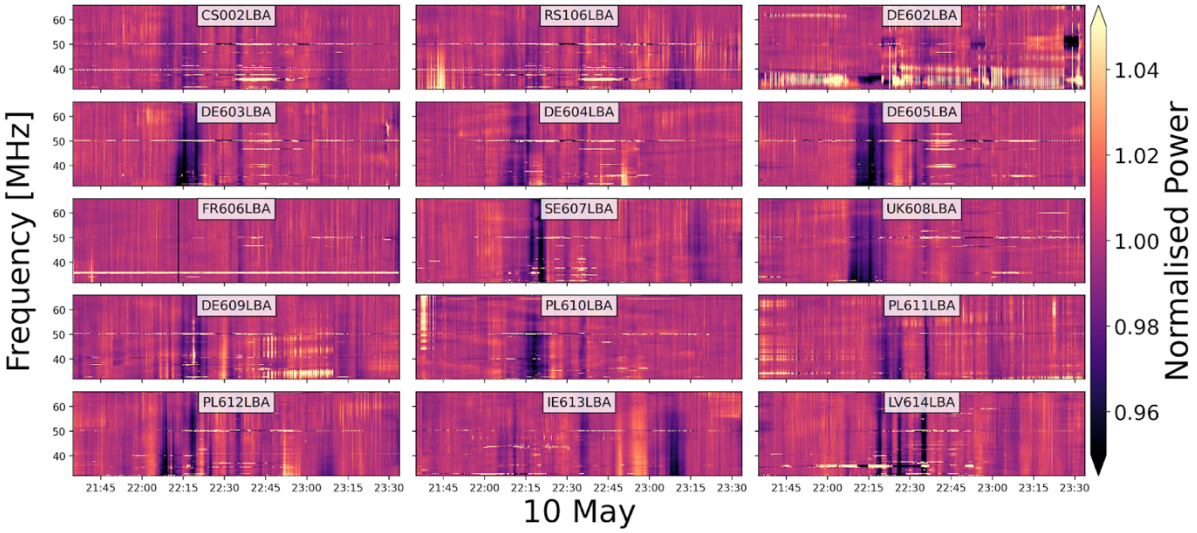



**Figure B1.** LOFAR data for observation L2040075, covering the period of May 10th from 21:35 until 23:35 UTC. The astronomical source of the signal is 3C380. The plot represents the normalised dynamic spectra of the CS002, RS106 and International LBA stations.

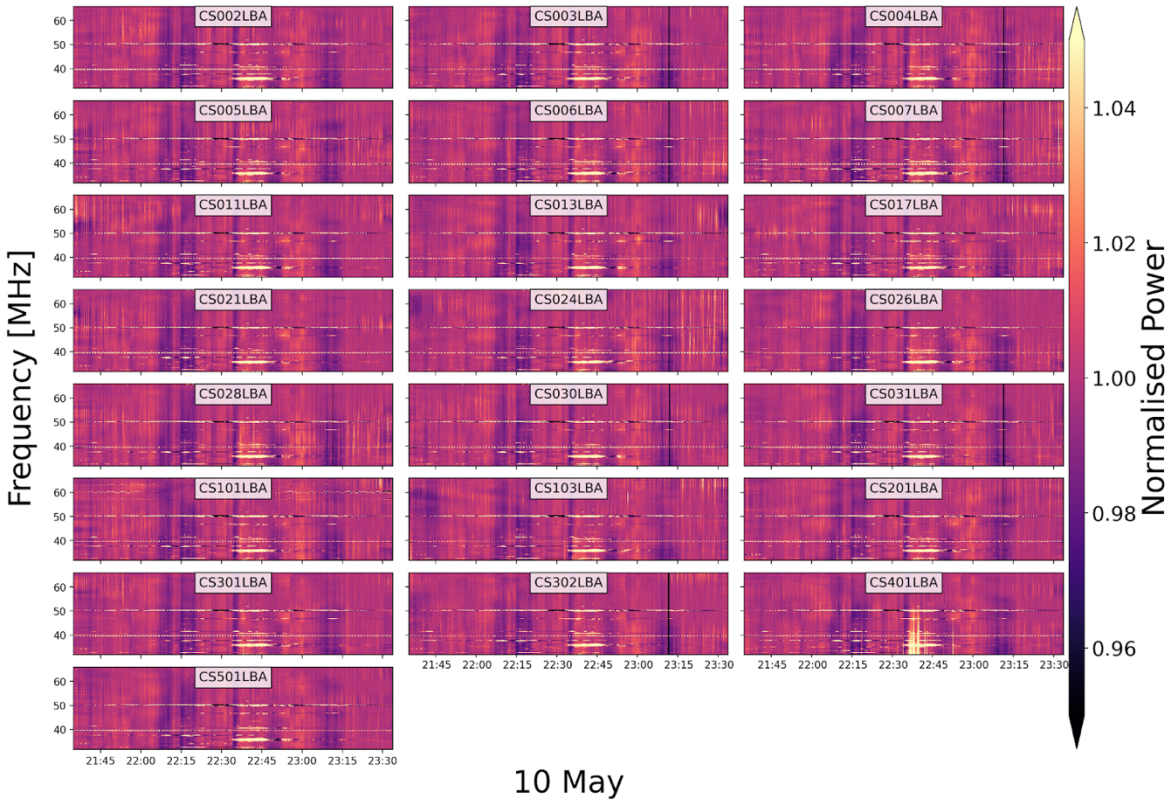



**Figure B2.** LOFAR dynamic spectra for observation L2040075, covering the period of May 10th from 21:35 until 23:35 UTC. The astronomical source of the signal is 3C380. The plot represents the data of the Core LBA stations.

# Annex C

Figures C1 and C2 show the complete set of S4 scintillation index data for the LOFAR observation L2040001, which is analysed in Section 4.2.4. This observation was conducted during the recovery phase of the superstorm on May 11th, 2024, from 03:40 to 11:40 UTC, using the High Band Antennas (HBA) to observe the radio source Cassiopeia A. The S4 index was calculated over a 180-second window. Figure C1 presents the S4 dynamic spectra for all HBA antennas in the LOFAR Core. Figure C2 shows the corresponding S4 spectra for the Core Station CS002, Remote Station RS106, and all International HBA0 stations. As noted in the main analysis, the scintillation patterns are highly consistent across the core stations, with the exception of CS103HBA0, which shows elevated noise. The plots clearly illustrate the trend discussed in Section 4.2.4, with the most intense scintillation (highest S4 values) occurring before 06:00 UTC and a significant reduction in activity after 09:00 UTC.

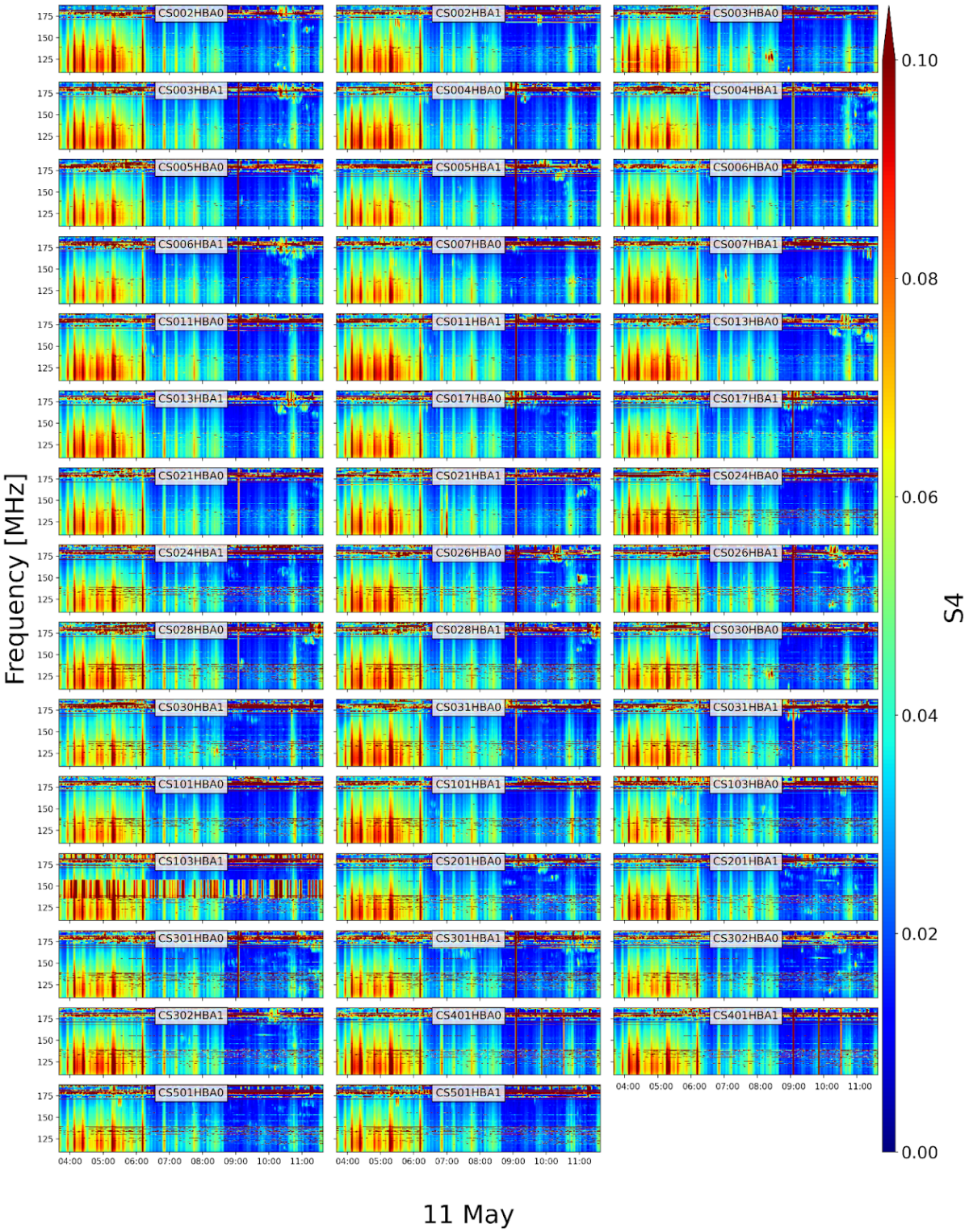



**Figure C1.** LOFAR data for observation L2040001, covering the period of May 11th from 3:40 until 11:40 UTC. The astronomical source of the signal is Cassiopeia A. The plot represents the S4 indexes, measured at 180s, of all the HBA Core antennas.

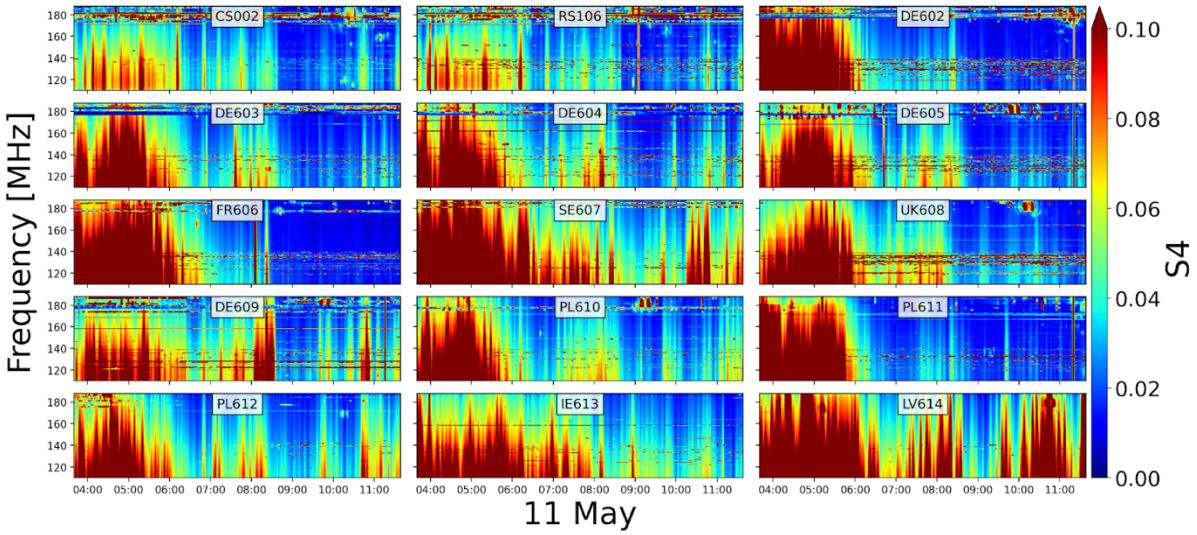



**Figure C2.** LOFAR data for observation L2040001, covering the period of May 11th from 3:40 until 11:40 UTC. The astronomical source of the signal is Cassiopeia A. The plot represents the S4 indexes, measured at 180s, of the CS002, RS106 and International HBA0 antennas.

# Annex D

For this study, IDOLS observations were available from May 10th at 13:35 UTC until May 14th at 08:30 UTC, covering the storm's main phase, recovery phase, and subsequent quiet periods. Using this dataset, it was possible reconstructed the ionospheric velocity by applying the algorithm based on the Fresnel frequency. Subsequently, the results derived from the 60 MHz IDOLS data were compared with those obtained from the 140 MHz HBA data during the morning of May 11th (Annex C). Both datasets contain the normalised signal intensity from Cassiopeia A. The results demonstrate a strong agreement, suggesting the robustness and reliability of Fresnel algorithm, independently from the selected frequency. Only for the sake of such comparison, the IPPs are projected at an altitude of 350 km, an assumption that will be severely criticised afterwards. Indeed, while the absolute velocity estimates are dependent on the chosen projection altitude, this scaling factor affects both datasets equivalently, thus preserving the strong agreement observed between the results, even in the case of a different selected altitude.

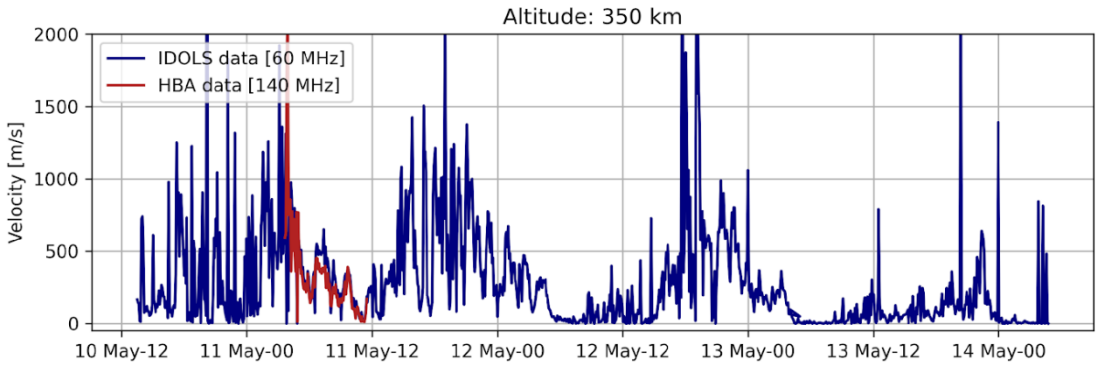



**Figure D1.** Velocity measured using Fresnel algorithm for IDOLS data (blue line) at 60 MHz and for L2040001 observation (red line) at 140 MHz.

# Annex E

Some interesting features appear also in the LOFAR datasets A and B. Specifically, in dataset A, corresponding to the LOFAR observation L2040063, the antennas were observing the radio source 3C48, in the period from 5:58 until 7:58 UTC of May 10th (Figure E1). It is possible to observe a rapid increment in the normalised power spectra of every station at the same time, beginning around 6:43 UTC. This effect is due to a X3.9 solar flare (Peak time at 06:54 UTC), as measured by the Geostationary Operational Environmental Satellites (GOES) 18, originating from the Sun and likely detected through the sidelobes of the LOFAR station beams. It is noteworthy how the increment of the GOES X-Ray flux (blue lines in figure E1) corresponds to the highest variation of the normalised intensity measured by all the LOFAR antennas. This rapid increment is followed by a strong reduction in the measured power. This is due to the absorption of the signal by the ionosphere.

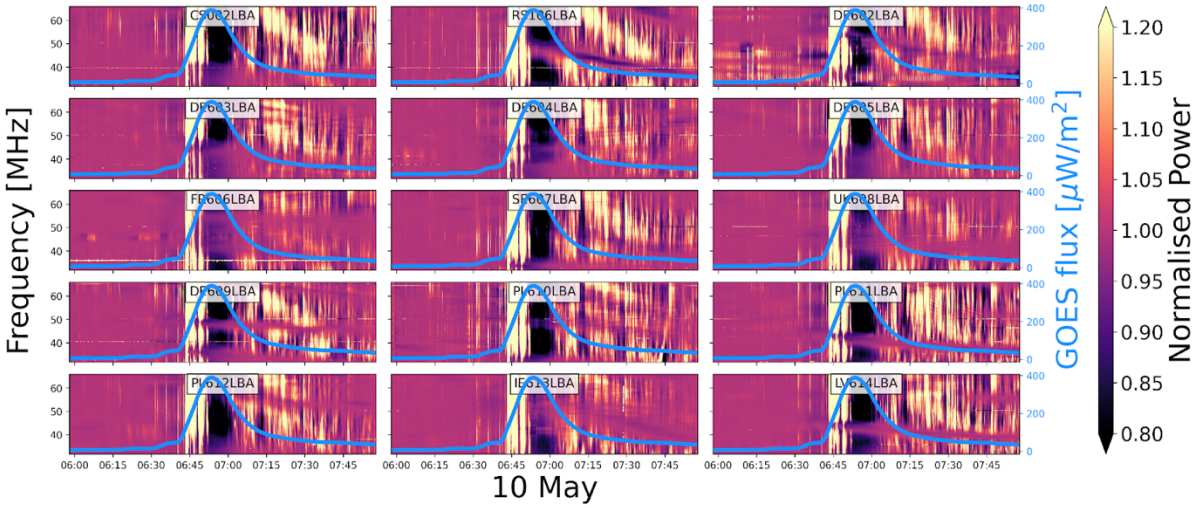



**Figure E1.** LOFAR normalized intensity data for observation L2040063, covering the period of May 10th from 05:58 until 07:58 UTC. The blue line represents the X-ray flux from GOES.

A similar feature is visible in the dataset B, that corresponds to the LOFAR observation L2040071 of the radio source 3C196, in the period from 11:25 until 13:25 UTC of May 10th (Figure E2). An increase in power measurements around 12:30 UT is observable in the normalized dynamic spectra across all stations. Given the large separation between the antennas, ionospheric effects can be ruled out.

Considering also the frequency dependence, it is likely that the effect originates from signals entering through the antenna sidelobes. This is, with high probability, a solar radio burst in the sidelobes of the antenna beams.

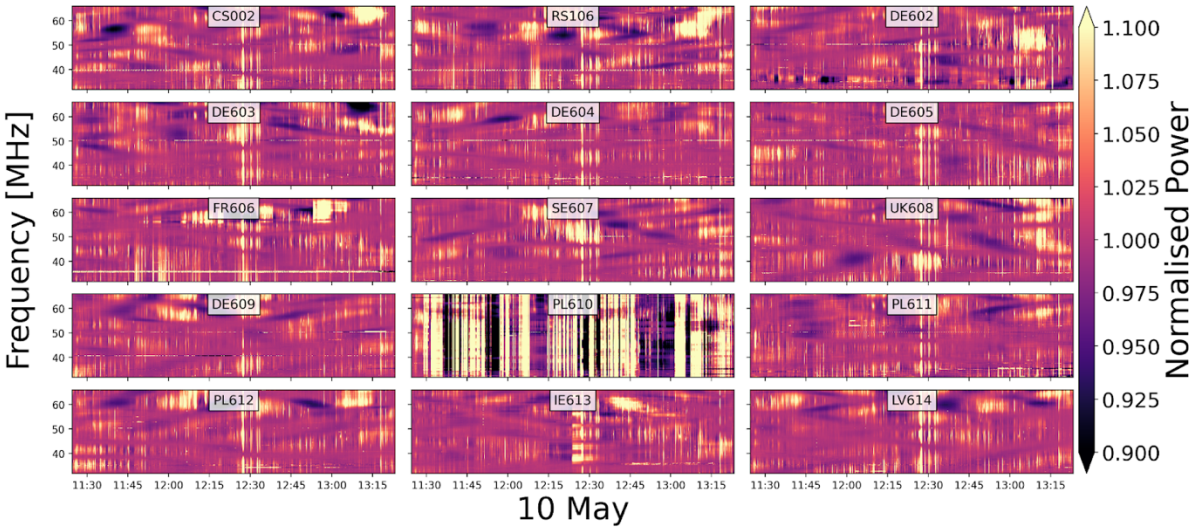



**Figure E2.** LOFAR normalized intensity data for observation L2040071, covering the period of May 10th from 11:25 until 13:25 UTC. Around 12:30 UTC the all the data show a rapid increment at the same instants. This represents the arrival of a solar radio burst.

# Annex F

Astronomical radio observations at the lowest frequencies (below 20 MHz) have gained interest for many reasons. Science at these frequencies include direct radio detection of Jupiter-like exoplanets, stellar flare studies and extragalactic science studying steep spectra radio sources like fossil radio plasma from radio galaxies. In normal conditions, the lowest frequencies are not available for ground-based observatories due to ionospheric cut-off. Also, the lowest frequency observations are often problematic due to ionospheric distortions and radio frequency interference that is reflected from the ionosphere (Chiang et al., 2020).

Between 09:00 UTC and 16:00 UTC on 12th May 2024, the IDOLS observation of Cassiopeia A, made using the CS032, operating between 10 and 80 MHz, did not show significant structuring due to ionospheric effects, based upon the S4 index (Figure F1) . Therefore, at this time, the ionospheric conditions were likely to have been particularly good for very low frequency radio observations. As these conditions occurred sometime after the main phase of the geomagnetic storm, it may be possible to use high levels of geomagnetic activity as a precursor for such conditions and to schedule LOFAR observations accordingly.

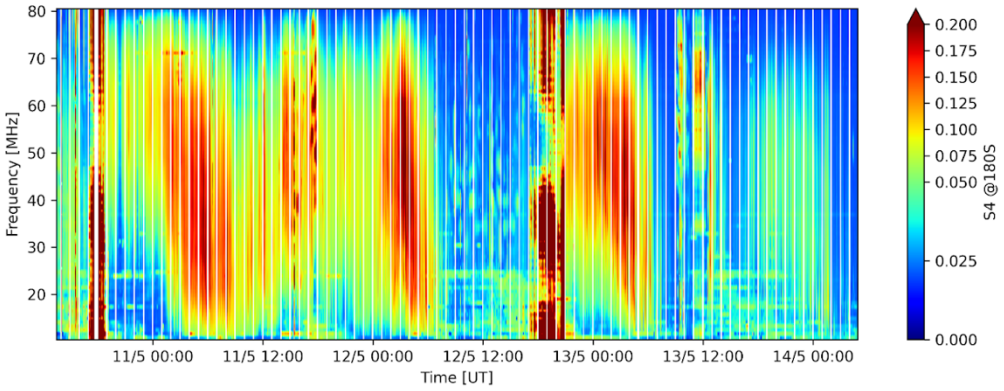



**Figure F1.** LOFAR data for IDOLS observation, covering the period from May 10th at 13:30 UTC until May 14th at 08:30 UTC. The astronomical source of the signal is Cassiopeia A. The plot represents the S4 index, measured at 180s, of the CS0032LBA

# Bibliography


Alfonsi, L., Cesaroni, C., Spogli, L., Regi, M., Paul, A., Ray, S., Lepidi, S., Di Mauro, D., Haralambous, H., Oikonomou, C., Shreedevi, P. R., & Sinha, A. K. (2021). Ionospheric Disturbances Over the Indian Sector During 8 September 2017 Geomagnetic Storm: Plasma Structuring and Propagation. *Space Weather*, *19*(3), e2020SW002607. https://doi.org/10.1029/2020SW002607

Alken, P., Thébault, E., Beggan, C. D., Amit, H., Aubert, J., Baerenzung, J., Bondar, T. N., Brown, W. J., Califf, S., Chambodut, A., Chulliat, A., Cox, G. A., Finlay, C. C., Fournier, A., Gillet, N., Grayver, A., Hammer, M. D., Holschneider, M., Huder, L., … Zhou, B. (2021). International Geomagnetic Reference Field: The thirteenth generation. *Earth, Planets and Space*, *73*(1), 49. https://doi.org/10.1186/s40623-020-01288-x

Apatenkov, S. V., Pilipenko, V. A., Gordeev, E. I., Viljanen, A., Juusola, L., Belakhovsky, V. B., Sakharov, Ya. A., & Selivanov, V. N. (2020). Auroral Omega Bands are a Significant Cause of Large Geomagnetically Induced Currents. *Geophysical Research Letters*, *47*(6), e2019GL086677. https://doi.org/10.1029/2019GL086677

Axford, W. I. (1963). The formation and vertical movement of dense ionized layers in the ionosphere due to neutral wind shears. *Journal of Geophysical Research (1896-1977)*, *68*(3), 769–779. https://doi.org/10.1029/JZ068i003p00769

Balan, N., Liu, L., & Le, H. (2018). A brief review of equatorial ionization anomaly and ionospheric irregularities. *Earth and Planetary Physics*, *2*(4), 257–275. https://doi.org/10.26464/epp2018025

Barta, Veronika, Potuznikova, Katerina, Knížová, Petra Koucká, Chum, Jaroslav, Mielich, Jens, Guerra, Marco, Buresova, Dalia, Sivakandan, Mani, Verhulst, Tobias G. W., Berényi, Kitti A., Altadill, David, Segarra, Antoni, Kouba, Daniel, Mosna, Zbysek, Buzás, Attila, Spogli, Luca, Urbář, Jaroslav, de Paula, Víctor, Ventriglia, Vincenzo, & Belehaki, Anna. (2025). Multi-instrument analysis of medium-scale travelling ionospheric disturbances generated by an intense tropospheric jet-front system with severe convection in Europe in August 2023. *J. Space Weather Space Clim.*, *15*, 31. https://doi.org/10.1051/swsc/2025025

Basu, S., Groves, K. M., Basu, Su., & Sultan, P. J. (2002). Specification and forecasting of scintillations in communication/navigation links: Current status and future plans. *Journal of Atmospheric and Solar-Terrestrial Physics*, *64*(16), 1745–1754. https://doi.org/10.1016/S1364-6826(02)00124-4

Belehaki, A., Häggström, I., Kiss, T., Galkin, I., Tjulin, A., Miháliková, M., Enell, C.-F., Pierantoni, G., Chen, Y., Sipos, G., Bruinsma, S., Pierrard, V., Altadill, D., Segarra, A., Navas-Portella, V., Pica, E., Spogli, L., Alfonsi, L., Cesaroni, C., … Watermann, J. (2025). Integrating plasmasphere, ionosphere and thermosphere observations and models into a standardised open access research environment: The PITHIA-NRF international project. *Advances in Space Research*, *75*(3), 3082–3114. https://doi.org/10.1016/j.asr.2024.11.065

Benson, R. F., & Bilitza, D. (2009). New satellite mission with old data: Rescuing a unique data set. *Radio Science*, *44*(1). https://doi.org/10.1029/2008RS004036

Bhattacharyya, A. (2022). Equatorial Plasma Bubbles: A Review. *Atmosphere*, *13*(10), 1637. https://doi.org/10.3390/atmos13101637

Borries, C., Jakowski, N., & Wilken, V. (2009). Storm induced large scale TIDs observed in GPS derived TEC. *Annales Geophysicae*, *27*(4), 1605–1612. https://doi.org/10.5194/angeo-27-1605-2009

Bougard, B., Sleewaegen, J., Spogli, L., Sreeja Vadakke Veettil, J., & Galera, M. (2011). *CIGALA: Challenging the Solar Maximum in Brazil with PolaRxS*. Proceedings of the 24th International Technical Meeting of the Satellite Division of The Institute of Navigation (ION GNSS 2011). https://www.ion.org/publications/abstract.cfm?articleID=9810

Boyde, B., Wood, A., Dorrian, G., Fallows, R., Themens, D., Mielich, J., Elvidge, S., Mevius, M., Zucca, P., Dabrowski, B., Krankowski, A., Vocks, C., & Bisi, M. (2022). Lensing from small-scale travelling ionospheric disturbances observed using LOFAR. *J. Space Weather Space Clim.*, *12*, 34. https://doi.org/10.1051/swsc/2022030

Brekke, A. (2013). The ionosphere. In A. Brekke (Ed.), *Physics of the Upper Polar Atmosphere* (pp. 189–245). Springer. https://doi.org/10.1007/978-3-642-27401-5_4

Burt, J., & Smith, B. (2012). Deep Space Climate Observatory: The DSCOVR mission. *2012 IEEE Aerospace Conference*, 1–13. https://doi.org/10.1109/AERO.2012.6187025

Cahyadi, M. N., Handoko, E. Y., Rahayu, R. W., & Heki, K. (2021). Comparison of volcanic explosions in Japan using impulsive ionospheric disturbances. *Earth, Planets and Space*, *73*(1), 228. https://doi.org/10.1186/s40623-021-01539-5

Carrano, C., Groves, K., & Rino, C. (2019). On the Relationship Between the Rate of Change of Total Electron Content Index (ROTI), Irregularity Strength (CL), and the Scintillation Index (S). *Journal of Geophysical Research: Space Physics*, *124*(3), 2099–2112. https://doi.org/10.1029/2018JA026353

Cesaroni, C., Alfonsi, L., Pezzopane, M., Martinis, C., Baumgardner, J., Wroten, J., Mendillo, M., Musicò, E., Lazzarin, M., & Umbriaco, G. (2017). The First Use of Coordinated Ionospheric Radio and Optical Observations Over Italy: Convergence of High-and Low-Latitude Storm-Induced Effects. *Journal of Geophysical Research: Space Physics*, *122*(11), 11,794-11,806. https://doi.org/10.1002/2017JA024325

Cesaroni, C., Spogli, L., & De Franceschi, G. (2021). IONORING: Real-Time Monitoring of the Total Electron Content over Italy. *Remote Sensing*, *13*(16), 3290. https://doi.org/10.3390/rs13163290

Cesaroni, C., Spogli, L., Franceschi, G. D., Damaceno, J. G., Grzesiak, M., Vani, B., Monico, J. F. G., Romano, V., Alfonsi, L., & Cafaro, M. (2021). A measure of ionospheric irregularities: Zonal velocity and its implications for L-band scintillation at low-latitudes. *Earth and Planetary Physics*, *5*(5), eepp2021042. https://doi.org/10.26464/epp2021042

Chabanski, S., de Montety, F., Lilensten, J., Poedts, S., & Spogli, L. (2025). The Power of a Name: Toward a Unified Approach to Naming Space Weather Events. *Perspectives of Earth and Space Scientists*, *6*(1), e2025CN000285. https://doi.org/10.1029/2025CN000285

Chabanski, S., Montety, F., Lilensten, J., Poedts, S., & Spogli, L. (2025). The power of a name: Toward a unified approach to naming space weather events. *Perspectives of Earth and Space Scientists*, *6*(1), 2025 000285. https://doi.org/10.1029/2025CN000285

Chapman, S. (1931). The absorption and dissociative or ionizing effect of monochromatic radiation in an atmosphere on a rotating earth. *Proceedings of the Physical Society*, *43*(1), 26. https://doi.org/10.1088/0959-5309/43/1/305

Cherniak, I., Zakharenkova, I., & Redmon, R. (2015). Dynamics of the high-latitude ionospheric irregularities during the 17 March 2015 St. Patrick's Day storm: Ground-based GPS measurements. *Space Weather*, *13*(9), 585–597. https://doi.org/10.1002/2015SW001237

Chernyshov, A. A., Klimenko, M. V., Nosikov, I. A., Borchevkina, O. P., Timchenko, A. V., Efishov, I. I., & Chugunin, D. V. (2025). *Effects in the upper atmosphere and ionosphere in the subauroral region during Victory Day 2024 Geomagnetic Storm (May 10–12, 2024). Advances in Space Research.https://doi.org/10.1016/j.asr.2025.02.015*.

Chiang, H. C., Dyson, T., Egan, E., Eyono, S., Ghazi, N., Hickish, J., Jáuregui-García, J. M., Manukha, V., Menard, T., Moso, T., Peterson, J., Philip, L., Sievers, J. L., & Tartakovsky, S. (2020). *The Array of Long Baseline Antennas for Taking Radio Observations from the Sub-Antarctic*.

Chou, M.-Y., Shen, M.-H., Lin, C. C. H., Yue, J., Chen, C.-H., Liu, J.-Y., & Lin, J.-T. (2018). Gigantic Circular Shock Acoustic Waves in the Ionosphere Triggered by the Launch of FORMOSAT-5 Satellite. *Space Weather*, *16*(2), 172–184. https://doi.org/10.1002/2017SW001738

Ciraolo, L., Azpilicueta, F., Brunini, C., Meza, A., & Radicella, S. (2007). Calibration Errors on Experimental Slant Total Electron Content (TEC) Determined with GPS. *Journal of Geodesy*, *81*, 111–120. https://doi.org/10.1007/s00190-006-0093-1

Curtis, J. A., & Adams, L. J. (1987). Defense Meteorological Satellite Program. *IEEE Aerospace and Electronic Systems Magazine*, *2*(3), 13–17. https://doi.org/10.1109/MAES.1987.5005348

Edler, H. W., Gasperin, F. de, & Rafferty, D. (2021). Investigating ionospheric calibration for LOFAR 2.0 with simulated observations. *Astronomy & Astrophysics*, *652*, A37. https://doi.org/10.1051/0004-6361/202140465

Elvidge, S., & Themens, D. R. (2025). The probability of the May 2024 geomagnetic superstorm. *Space Weather*, *23*(1), 2024 004113,. https://doi.org/10.1029/2024SW004113.

Enengl, F., Spogli, L., Kotova, D., Jin, Y., Oksavik, K., Partamies, N., & Miloch, W. J. (2024). Investigation of Ionospheric Small-Scale Plasma Structures Associated With Particle Precipitation. *Space Weather*, *22*(1), e2023SW003605. https://doi.org/10.1029/2023SW003605

Fagundes, P., Pillat, V., Habarulema, J., Muella, M., Venkatesh, K., Abreu, A., Anoruo, C., Vieira, F., Welyargis, K., & AgyeiYeboah, E. (2025). Equatorial Ionization Anomaly Disturbances (EIA) Triggered by the May 2024 Solar Coronal Mass Ejection (CME): The Strongest Geomagnetic Superstorm in the Last Two Decades. *Adv. Space Res*. https://doi.org/10.1016/j.asr.2025.02.007.

Fallows, RA., Forte, B., Astin, I., Allbrook, T., Arnold, A., Wood, A., Dorrian, G., Mevius, M., Rothkaehl, H., Matyjasiak, B., Krankowski, A., Anderson, J. M., Asgekar, A., Avruch, I. M., Bentum, M., Bisi, M. M., Butcher, H. R., Ciardix, H. R., Dabrowski, B., … Zucca, P. (2020b). A LOFAR observation of ionospheric scintillation from two simultaneous travelling ionospheric disturbances. *J. Space Weather Space Clim.*, *10*, 10. https://doi.org/10.1051/swsc/2020010

Forte, B., Fallows, R., Bisi, M., Zhang, J., Krankowski, A., Dabrowski, B., Rothkaehl, H., & Vocks, C. (2022). Interpretation of Radio Wave Scintillation Observed through LOFAR Radio Telescopes. *The Astrophysical Journal Supplement Series*, *263*(2), 36. https://doi.org/10.3847/1538-4365/ac6deb

Forte, B., & Radicella, S. (2002). Problems in data treatment for ionospheric scintillation measurements. *Radio Science*, *37*(6), 8-1-8–5. https://doi.org/10.1029/2001RS002508

Foster, J. C., Erickson, P. J., Nishimura, Y., Zhang, S. R., Bush, D. C., Coster, A. J., & Franco-Diaz, E. (2024). Imaging the May 2024 extreme aurora with ionospheric total electron content. *Geophysical Research Letters*, *51*(20), 2024 111981. https://doi.org/10.1029/2024GL111981

Friis-Christensen, E., Lühr, H., Knudsen, D., & Haagmans, R. (2008). Swarm – An Earth Observation Mission investigating Geospace. *Advances in Space Research*, *41*(1), 210–216. https://doi.org/10.1016/j.asr.2006.10.008

Gasperin, F. de, Dijkema, T. J., Drabent, A., Mevius, M., Rafferty, D., Weeren, R. van, Brüggen, M., Callingham, J. R., Emig, K. L., Heald, G., Intema, H. T., Morabito, L. K., Offringa, A. R., Oonk, R., Orrù, E., Röttgering, H., Sabater, J., Shimwell, T., Shulevski, A., & Williams, W.

(2019a). Systematic effects in LOFAR data: A unified calibration strategy. *Astronomy & Astrophysics*, *622*, A5. https://doi.org/10.1051/0004-6361/201833867

Gasperin, F. de, Dijkema, T. J., Drabent, A., Mevius, M., Rafferty, D., Weeren, R. van, Brüggen, M., Callingham, J. R., Emig, K. L., Heald, G., Intema, H. T., Morabito, L. K., Offringa, A. R., Oonk, R., Orrù, E., Röttgering, H., Sabater, J., Shimwell, T., Shulevski, A., & Williams, W. (2019b). Systematic effects in LOFAR data: A unified calibration strategy. *Astronomy & Astrophysics*, *622*, A5. https://doi.org/10.1051/0004-6361/201833867

Gasperin, F. de, Vink, J., McKean, J. P., Asgekar, A., Avruch, I., Bentum, M. J., Blaauw, R., Bonafede, A., Broderick, J. W., Brüggen, M., Breitling, F., Brouw, W. N., Butcher, H. R., Ciardi, B., Cuciti, V., Vos, M. de, Duscha, S., Eislöffel, J., Engels, D., … Zucca, P. (2020). Cassiopeia A, Cygnus A, Taurus A, and Virgo A at ultra-low radio frequencies. *Astronomy & Astrophysics*, *635*, A150. https://doi.org/10.1051/0004-6361/201936844

Ghidoni, R., Spogli, L., Mevius, M., Cesaroni, C., Alfonsi, L., Beser, K., Guerra, M., & Maestri, T. (2025). Ionospheric Response to the January 2022 Geomagnetic Storm Using LOFAR and GNSS. *Journal of Space Weather and Space Climate*. https://doi.org/10.1051/swsc/2025052

Ghidoni, R., Spogli Luca, Dorrian Gareth, Mevius Maaijke, Pawel, F., Katarzyna, B., Forte, B., Marcin, G., Kacper, K., Ben, B., Pozoga, M., Dorota, P.-S., Wood, A., Zucca, P., Jānis, Š., Paul, K., Tianchu, L., Claudio, C., Rothkaehl, H., … Tiziano, M. (2025). *LOFAR uniqueness under extreme ionospheric conditions: The May 2024 Mother's Day Superstorm*. Preprints. https://doi.org/10.22541/essoar.176169469.93512147/v1

Gold, V., McNaught, A., & The International Union of Pure and Applied Chemistry (IUPAC) (Eds). (2025). *The IUPAC Compendium of Chemical Terminology: The Gold Book* (5th edn). International Union of Pure and Applied Chemistry (IUPAC). https://doi.org/10.1351/goldbook

Grzesiak, M., Pożoga, M., Matyjasiak, B., Przepiórka, D., Beser, K., Tomasik, L., Rothkaehl, H., & Ciechowska, H. (2022). Determining Ionospheric Drift and Anisotropy of Irregularities from LOFAR Core Measurements: Testing Hypotheses behind Estimation. *Remote Sensing*, *14*(18), 4655. https://doi.org/10.3390/rs14184655

Guerra, M., Cesaroni, C., Ravanelli, M., & Spogli, L. (2024). Travelling ionospheric disturbances detection: A statistical study of detrending techniques, induced period error and near real-time observables. *J. Space Weather Space Clim.*, *14*, 17. https://doi.org/10.1051/swsc/2024017

Hajj, G. A., & Romans, L. J. (1998). Ionospheric electron density profiles obtained with the Global Positioning System: Results from the GPS/MET experiment. *Radio Science*, *33*(1), 175–190. https://doi.org/10.1029/97RS03183

Haldoupis, C. (2011). A Tutorial Review on Sporadic E Layers. In M. A. Abdu & D. Pancheva (Eds), *Aeronomy of the Earth's Atmosphere and Ionosphere* (pp. 381–394). Springer Netherlands. https://doi.org/10.1007/978-94-007-0326-1_29

Hardy, D. A., Gussenhoven, M. S., & Holeman, E. (1985). A statistical model of auroral electron precipitation. *Journal of Geophysical Research: Space Physics*, *90*(A5), 4229–4248. https://doi.org/10.1029/JA090iA05p04229

Hernández-Pajares, M., Juan, J. M., Sanz, J., & Aragón-Àngel, A. (2012). Propagation of medium scale traveling ionospheric disturbances at different latitudes and solar cycle conditions. *Radio Science*, *47*(6). https://doi.org/10.1029/2011RS004951

Hey, J. S., Parsons, S. J., & Phillips, J. W. (1946). Fluctuations in Cosmic Radiation at Radio-Frequencies. *Nature*, *158*(4007), 234–234. https://doi.org/10.1038/158234a0

Hocke, K., & Schlegel, K. (1996). A review of atmospheric gravity waves and travelling ionospheric disturbances: 1982-1995. *Annales Geophysicae*, *14*(9), 917–940. https://doi.org/10.1007/s00585-996-0917-6

Honda, R. H., Kherani, E. A., Figueiredo, C. a. O. B., Astafyeva, E., Wrasse, C. M., & Naccarato, K. P. (2025). Resonant Infrasonic Disturbances in Total-Electron-Content During a Severe Thunderstorm on 23 October 2021. *Journal of Geophysical Research: Space Physics*, *130*(3), e2024JA033679. https://doi.org/10.1029/2024JA033679

Horvath, I., & Lovell, B. (2021). Complex Sub-Auroral Flow Channel Structure Formed by Double-Peak Sub-Auroral Ion Drifts (DSAID) and Abnormal Sub-Auroral Ion Drifts (ASAID). *Journal of Geophysical Research: Space Physics*, *126*(1), e2020JA028475. https://doi.org/10.1029/2020JA028475

Hunsucker, R. D., & Hargreaves, J. K. (2002). The High-Latitude Ionosphere and its Effects on Radio Propagation. In *The High-Latitude Ionosphere and its Effects on Radio Propagation*. https://ui.adsabs.harvard.edu/abs/2002hlie.book.....H

Iijima, T., & Potemra, T. A. (1976). Field-aligned currents in the dayside cusp observed by Triad. *Journal of Geophysical Research (1896-1977)*, *81*(34), 5971–5979. https://doi.org/10.1029/JA081i034p05971

Ippolito, A., Alberti, T., & Giannattasio, F. (2025). Modeling the Magnetic Connection from Earth to Solar Corona during the May 11 Geomagnetic Superstorm. *The Astrophysical Journal*, *979*(2), 146. https://doi.org/10.3847/1538-4357/ada35a

Jin, Y., Kotova, D., Clausen, L. B. N., & Miloch, W. J. (2025). Significant Plasma Density Depletion From High- to Mid-Latitude Ionosphere During the Super Storm in May 2024. *Geophysical Research Letters*, *52*(5), e2024GL113997. https://doi.org/10.1029/2024GL113997

Jonah, O. F., Vergados, P., Krishnamoorthy, S., & Komjathy, A. (2021). Investigating Ionospheric Perturbations Following the 2020 Beirut Explosion Event. *Radio Science*, *56*(10), e2021RS007302. https://doi.org/10.1029/2021RS007302

Katamzi, Z. T., Smith, N. D., Mitchell, C. N., Spalla, P., & Materassi, M. (2012). Statistical analysis of travelling ionospheric disturbances using TEC observations from geostationary satellites. *Journal of Atmospheric and Solar-Terrestrial Physics*, *74*, 64–80. https://doi.org/10.1016/j.jastp.2011.10.006

Kataoka, R., Reddy, S. A., & Nakano, S. (2024). Extended magenta aurora as revealed by citizen science. *Science Reports*, *14*, 25849. https://doi.org/10.1038/s41598-024-75184-9

Kauristie, K., Morschhauser, A., Olsen, N., Finlay, C. C., McPherron, R. L., Gjerloev, J. W., & Opgenoorth, H. J. (2017). On the Usage of Geomagnetic Indices for Data Selection in Internal Field Modelling. *Space Science Reviews*, *206*(1), 61–90. https://doi.org/10.1007/s11214-016-0301-0

Kelley, M. C. (1989). Fundamentals of Ionospheric Plasma Dynamics. In *The Earth's Ionosphere* (pp. 23–63). Elsevier. https://doi.org/10.1016/B978-0-12-404013-7.50007-1

Kelley, M. C. (2009). *The Earth's Ionosphere: Plasma Physics and Electrodynamics*. Academic Press.

Kotulak, K., Zakharenkova, I., Krankowski, A., Cherniak, I., Wang, N., & Fron, A. (2020). Climatology Characteristics of Ionospheric Irregularities Described with GNSS ROTI. *Remote Sensing*, *12*(16), 2634. https://doi.org/10.3390/rs12162634

Li, G., Ning, B., Otsuka, Y., Abdu, M. A., Abadi, P., Liu, Z., Spogli, L., & Wan, W. (2021). Challenges to Equatorial Plasma Bubble and Ionospheric Scintillation Short-Term Forecasting and Future Aspects in East and Southeast Asia. *Surveys in Geophysics*, *42*(1), 201–238. https://doi.org/10.1007/s10712-020-09613-5

Loto'aniu, P., Romich, K., Rowland, W., Codrescu, S., Biesecker, D., Johnson, J., Singer, H. J., Szabo, A., & Stevens, M. (2022). Validation of the DSCOVR Spacecraft Mission Space

Weather Solar Wind Products. *Space Weather*, *20*(10), e2022SW003085. https://doi.org/10.1029/2022SW003085

Luo, X., Lou, Y., Xiao, Q., Gu, S., Chen, B., & Liu, Z. (2018). Investigation of ionospheric scintillation effects on BDS precise point positioning at low-latitude regions. *GPS Solutions*, *22*(3), 63. https://doi.org/10.1007/s10291-018-0728-8

Mannucci, A. J., Wilson, B. D., Yuan, D. N., Ho, C. H., Lindqwister, U. J., & Runge, T. F. (1998). A global mapping technique for GPS-derived ionospheric total electron content measurements. *Radio Science*, *33*(3), 565–582. https://doi.org/10.1029/97RS02707

Marconi, G. (2002). Wireless telegraphic communication. *Resonance*, *7*(1), 95–101. https://doi.org/10.1007/BF02836176

Matzka, J., Stolle, C., Yamazaki, Y., Bronkalla, O., & Morschhauser, A. (2021). The Geomagnetic Kp Index and Derived Indices of Geomagnetic Activity. *Space Weather*, *19*(5), e2020SW002641. https://doi.org/10.1029/2020SW002641

Mevius, M., van der Tol, S., Pandey, V., Vedantham, H., Brentjens, M., de Bruyn, A., Abdalla, F. B., Asad, K. M. B., Bregman, J. D., Brouw, W. N., Bus, S., Chapman, E., Ciardi, B., Fernandez, E. R., Ghosh, A., Harker, G., Iliev, I. T., Jelić, V., Kazemi, S., … Zaroubi, S. (2016). Probing ionospheric structures using the LOFAR radio telescope. *Radio Science*, *51*(7), 927–941. https://doi.org/10.1002/2016RS006028

Nishimura, Y., Kelly, T., Jayachandran, P. T., Mrak, S., Semeter, J. L., Donovan, E. F., Angelopoulos, V., & Nishitani, N. (2023). Nightside High-Latitude Phase and Amplitude Scintillation During a Substorm Using 1-Second Scintillation Indices. *Journal of Geophysical Research: Space Physics*, *128*(8), e2023JA031402. https://doi.org/10.1029/2023JA031402

Paul, K. S., Moses, M., Haralambous, H., & Oikonomou, C. (2025). Effects of the Mother's Day Superstorm (10–11 May 2024) over the Global Ionosphere. *Remote Sensing*, *17*(5), 859. https://doi.org/10.3390/rs17050859

Paxton, L. J., Morrison, D., Zhang, Y., Kil, H., Wolven, B., Ogorzalek, B. S., Humm, D. C., & Meng, C.-I. (2002). *Validation of remote sensing products produced by the Special Sensor Ultraviolet Scanning Imager (SSUSI): A far UV-imaging spectrograph on DMSP F-16* (A. M. Larar & M. G. Mlynczak, Eds; pp. 338–348). https://doi.org/10.1117/12.454268

Pedersen, M. N., Juusola, L., Vanhamäki, H., Aikio, A. T., & Viljanen, A. (2024). Rapid Geomagnetic Variations During High-Speed Stream, Sheath and Magnetic Cloud-Driven Geomagnetic Storms From 1996 to 2023. *Journal of Geophysical Research: Space Physics*, *129*(10), e2024JA032656. https://doi.org/10.1029/2024JA032656

Pierrard, V., Verhulst, T. G., Chevalier, J. M., Bergeot, N., & Winant, A. (2025). Effects of the Geomagnetic Superstorms of 10–11 May 2024 and 7–11 October 2024 on the Ionosphere and Plasmasphere. *Atmosphere*, *16*(3), 299. https://doi.org/10.3390/atmos16030299

Poniatowski, M., & Nykiel, G. (2020). Degradation of Kinematic PPP of GNSS Stations in Central Europe Caused by Medium-Scale Traveling Ionospheric Disturbances During the St. Patrick's Day 2015 Geomagnetic Storm. *Remote Sensing*, *12*(21), 3582. https://doi.org/10.3390/rs12213582

Purfürst, T. (2022). Evaluation of Static Autonomous GNSS Positioning Accuracy Using Single-, Dual-, and Tri-Frequency Smartphones in Forest Canopy Environments. *Sensors (Basel, Switzerland)*, *22*(3), 1289. https://doi.org/10.3390/s22031289

Ranjan, A. K., Nailwal, D., Sunil Krishna, M. V., Kumar, A., & Sarkhel, S. (2024). Evidence of potential thermospheric overcooling during the May 2024 geomagnetic superstorm. *Journal of Geophysical Research: Space Physics*, *129*(12), 2024 033148. https://doi.org/10.1029/2024JA033148

Reinisch, B. W., & Galkin, I. A. (2011). Global Ionospheric Radio Observatory (GIRO). *Earth, Planets and Space*, *63*(4), 377–381. https://doi.org/10.5047/eps.2011.03.001

Reinisch, B. W., Galkin, I. A., Khmyrov, G. M., Kozlov, A. V., Bibl, K., Lisysyan, I. A., Cheney, G. P., Huang, X., Kitrosser, D. F., Paznukhov, V. V., Luo, Y., Jones, W., Stelmash, S., Hamel, R., & Grochmal, J. (2009). New Digisonde for research and monitoring applications. *Radio Science*, *44*(1). https://doi.org/10.1029/2008RS004115

Rietveld, M. T., Wright, J. W., Zabotin, N., & Pitteway, M. L. V. (2008). The Tromsø dynasonde. *Polar Science*, *2*(1), 55–71. https://doi.org/10.1016/j.polar.2008.02.001

Romano, P., Elmhamdi, A., Marassi, A., & Contarino, L. (2024). Analyzing the sequence of phases leading to the formation of the active region 13664, with potential Carrington-like characteristics. *The Astrophysical Journal Letters*, *973*(1), 31. https://doi.org/10.3847/2041-8213/ad77cb

Sanchez, S. A., Kherani, E. A., Astafyeva, E., & de Paula, E. R. (2025). The First Near-Real-Time Compatible Numerical Method for Co-Seismic Ionospheric Disturbances Simulation. *Geophysical Research Letters*, *52*(8), e2025GL115208. https://doi.org/10.1029/2025GL115208

Schafer, R. (2011). What Is a Savitzky-Golay Filter? *IEEE Signal Processing Magazine*, *28*(4). https://doi.org/10.1109/MSP.2011.941097

Siegel, D. M. (1976). Balfour Stewart and Gustav Robert Kirchhoff: Two Independent Approaches to 'Kirchhoff's Radiation Law'. *Isis*, *67*(4), 565–600.

Smith, F. G. (1950). Origin of the Fluctuations in the Intensity of Radio Waves from Galactic Sources: Cambridge Observations. *Nature*, *165*(4194), 422–423. https://doi.org/10.1038/165422a0

Song, K., Meziane, K., Hamza, A. M., & Jayachandran, P. T. (2025). Investigation of the Fresnel Scale From Ionospheric Scintillation Spectra. *Journal of Geophysical Research: Space Physics*, *130*(2), e2024JA033239. https://doi.org/10.1029/2024JA033239

Sotomayor-Beltran, C., Sobey, C., Hessels, J. W. T., Bruyn, G. de, Noutsos, A., Alexov, A., Anderson, J., Asgekar, A., Avruch, I. M., Beck, R., Bell, M. E., Bell, M. R., Bentum, M. J., Bernardi, G., Best, P., Birzan, L., Bonafede, A., Breitling, F., Broderick, J., … Zarka, P. (2013). Calibrating high-precision Faraday rotation measurements for LOFAR and the next generation of low-frequency radio telescopes. *Astronomy & Astrophysics*, *552*, A58. https://doi.org/10.1051/0004-6361/201220728

Spogli, L., Alberti, T., Bagiacchi, P., Cafarella, L., Cesaroni, C., Cianchini, G., Coco, I., Mauro, D. D., Ghidoni, R., Giannattasio, F., Ippolito, A., Marcocci, C., Pezzopane, M., Pica, E., Pignalberi, A., Perrone, L., Romano, V., Sabbagh, D., Scotto, C., … Viola, M. (2024). The effects of the May 2024 Mother's Day superstorm over the Mediterranean sector: From data to public communication. *Annals of Geophysics*, *67*(2), PA218–PA218. https://doi.org/10.4401/ag-9117

Spogli, L., Alfonsi, L., & Cesaroni, C. (2023). Stepping Into an Equatorial Plasma Bubble With a Swarm Overfly. *Space Weather*, *21*(5), e2022SW003331. https://doi.org/10.1029/2022SW003331

Spogli, L., Alfonsi, L., De Franceschi, G., Romano, V., Aquino, M. H. O., & Dodson, A. (2009). Climatology of GPS ionospheric scintillations over high and mid-latitude European regions. *Annales Geophysicae*, *27*(9), 3429–3437. https://doi.org/10.5194/angeo-27-3429-2009

Spogli, L., Ghobadi, H., Cicone, A., Alfonsi, L., Cesaroni, C., Linty, N., Romano, V., & Cafaro, M. (2021). Adaptive Phase Detrending for GNSS Scintillation Detection: A Case Study Over Antarctica. *IEEE Geoscience and Remote Sensing Letters*, *PP*, 1–5. https://doi.org/10.1109/LGRS.2021.3067727

Tanskanen, E. I. (2009). A comprehensive high-throughput analysis of substorms observed by IMAGE magnetometer network: Years 1993–2003 examined. *Journal of Geophysical Research: Space Physics*, *114*(A5), 2008JA013682. https://doi.org/10.1029/2008JA013682

Thaganyana, G. P., Habarulema, J. B., Ngwira, C., & Azeem, I. (2022). Equatorward Medium to Large-Scale Traveling Ionospheric Disturbances of High Latitude Origin During Quiet Conditions. *Journal of Geophysical Research: Space Physics*, *127*(3), e2021JA029558. https://doi.org/10.1029/2021JA029558

Themens, D. R., Elvidge, S., McCaffrey, A., Jayachandran, P. T., Coster, A., & Varney, R. H. (2024). The high latitude ionospheric response to the major May 2024 geomagnetic storm: A synoptic view. *Geophysical Research Letters*, *51, e2*. https://doi.org/10.1029/2024GL111677

Thompson, A. R., Moran, J. M., & Swenson, G. W. (2017). Van Cittert–Zernike Theorem, Spatial Coherence, and Scattering. In A. R. Thompson, J. M. Moran, & G. W. Swenson Jr. (Eds), *Interferometry and Synthesis in Radio Astronomy* (pp. 767–786). Springer International Publishing. https://doi.org/10.1007/978-3-319-44431-4_15

Tsybulya, K., & Jakowski, N. (2005). Medium- and small-scale ionospheric irregularities detected by GPS radio occultation method. *Geophysical Research Letters*, *32*(9). https://doi.org/10.1029/2005GL022420

Tulasi Ram, S., Veenadhari, B., Dimri, A. P., Bulusu, J., Bagiya, M., & Gurubaran, S. (2024). Super-intense geomagnetic storm on 10–11 May 2024: Possible mechanisms and impacts. *Space Weather*, *22*, 2024 004126. https://doi.org/10.1029/2024SW004126

Vadakke Veettil, S., & Aquino, M. (2021). Statistical models to provide meaningful information to GNSS users in the presence of ionospheric scintillation. *GPS Solutions*, *25*(2), 54. https://doi.org/10.1007/s10291-020-01083-x

van Haarlem, M., Wise, M., Gunst, A., Heald, G., McKean, J., Hessels, J., de Bruyn, A. G., Nijboer, R., Swinbank, J., Fallows, R., Brentjens, M., Nelles, A., Beck, R., Falcke, H., Fender, R., Hörandel, J., Koopmans, L. V. E., Mann, G., Miley, G., … van Zwieten, J. (2013). LOFAR: The LOw-Frequency ARray. *Astronomy & Astrophysics*, *556*, A2. https://doi.org/10.1051/0004-6361/201220873

Vanlommel, P. (2022). STCE newsletter: Issue 21 Jan 2022. *Geophysical Research Letters*. https://www.stce.be/newsletter/pdf/2022/STCEnews20220121.pdf

Verhulst, T. G. W., Altadill, D., Barta, V., Belehaki, A., Burešová, D., Cesaroni, C., Galkin, I., Guerra, M., Ippolito, A., Herekakis, T., Kouba, D., Mielich, J., Segarra, A., Spogli, L., & Tsagouri, I. (2022). Multi-instrument detection in Europe of ionospheric disturbances caused by the 15 January 2022 eruption of the Hunga volcano. *Journal of Space Weather and Space Climate*, *12*, 35. https://doi.org/10.1051/swsc/2022032

Viljanen, A., & Häkkinen, L. (1997). Image Magnetometer Network. *Satellite-Ground Based Coordination Sourcebook, ESA Special Publication*, *1198*, 111. https://ui.adsabs.harvard.edu/abs/1997ESASP1198..111V

Wei, Y., Zhao, B., Li, G., & Wan, W. (2015). Electric field penetration into Earth's ionosphere: A brief review for 2000–2013. *Science Bulletin*, *60*(8), 748–761. https://doi.org/10.1007/s11434-015-0749-4

Whitehead, J. D. (1961). The formation of the sporadic-E layer in the temperate zones. *Journal of Atmospheric and Terrestrial Physics*, *20*(1), 49–58. https://doi.org/10.1016/0021-9169(61)90097-6

Wood, A., Alfonsi, L., Clausen, L., Jin, Y., Spogli, L., Urbar, J., Rawlings, J., Whittaker, I., Dorrian, G., Høeg, P., Kotova, D., Cesaroni, C., Cicone, A., Miedzik, J., Gierlach, E., Kochańska, P., Wojtkiewicz, P., Shahtahmassebi, G., & Miloch, W. (2022). Variability of Ionospheric

Plasma: Results from the ESA Swarm Mission. *Space Science Reviews*, *218*. https://doi.org/10.1007/s11214-022-00916-0

Wood, A. G., Donegan-Lawley, E. E., Clausen, L. B. N., Spogli, L., Urbář, J., Jin, Y., Shahtahmassebi, G., Alfonsi, L., Rawlings, J. T., Cicone, A., Kotova, D., Cesaroni, C., Høeg, P., Dorrian, G. D., Nugent, L. D., Elvidge, S., Themens, D. R., Aragón, M. J. B., Wojtkiewicz, P., & Miloch, W. J. (2024). Statistical models of the variability of plasma in the topside ionosphere: 1. Development and optimisation. *Journal of Space Weather and Space Climate*, *14*, 7. https://doi.org/10.1051/swsc/2024002

Wood, A. G., Dorrian, G. D., Boyde, B., Fallows, R. A., Themens, D. R., Mevius, M., Sprenger, T., Main, R., Pryse, S. E., & Elvidge, S. (2024). Quasi-stationary substructure within a sporadic E layer observed by the Low-Frequency Array (LOFAR). *Journal of Space Weather and Space Climate*, *14*, 27. https://doi.org/10.1051/swsc/2024024

Yang, Z., & Liu, Z. (2016). Correlation between ROTI and Ionospheric Scintillation Indices using Hong Kong low-latitude GPS data. *GPS Solutions*, *20*(4), 815–824. https://doi.org/10.1007/s10291-015-0492-y

Yeh, K. C., & Liu, C. (1982). Radio wave scintillations in the ionosphere. *Proceedings of the IEEE*, *70*(4), 324–360. https://doi.org/10.1109/PROC.1982.12313

Yin, F., Lühr, H., Park, J., & Wang, L. (2019). Comprehensive Analysis of the Magnetic Signatures of Small-Scale Traveling Ionospheric Disturbances,as Observed by Swarm. *Journal of Geophysical Research: Space Physics*, *124*(12), 10794–10815. https://doi.org/10.1029/2019JA027523

Zakharenkova, I., Astafyeva, E., & Cherniak, I. V. (2016). GPS and GLONASS observations of large-scale traveling ionospheric disturbances during the 2015 St. Patrick's Day storm: LSTIDs During the March 2015 Storm. *Journal of Geophysical Research: Space Physics*, *121*. https://doi.org/10.1002/2016JA023332

Zuccheretti, E., Tutone, G., Sciacca, U., Bianchi, C., & Baskaradas, J. A. (2003). The new AIS-INGV digital ionosonde. *Annals of Geophysics*, *46*(4), 647–659. https://doi.org/10.4401/ag-4377